

UNIVERSITÀ DEGLI STUDI DI TRENTO

Facoltà di Scienze Matematiche, Fisiche e Naturali



DOTTORATO DI RICERCA IN FISICA
XXIV CICLO

Tesi di Dottorato

EXPERIMENTAL STUDY OF ION-MOLECULE REACTIONS OF
AROMATIC HYDROCARBONS

Relatori: Dr. Daniela Ascenzi

Prof. Paolo Tosi

Dottoranda: Julia Aysina

Dicembre 2011

Abstract

This thesis presents experimental studies, based on guided ion beam mass spectrometric techniques and coupled to theoretical interpretations by quantum chemistry, on ionic mechanisms for the molecular growth of aromatic hydrocarbons with a particular relevance for understanding the formation of large molecules in ionized gases such as planetary ionospheres, plasmas and combustion systems. The starting point of this dissertation is a study of the reactivity of naphthyl cation $C_{10}H_7^+$ with benzene. Ion-molecule reactions leading to hydrocarbon growth via the formation of new C-C bond are studied with special reference to the association product $C_{16}H_{13}^+$. Another experiment in this dissertation concerns the reactivity of the $C_{12}H_9^+$ ion with benzene. The growth of hydrocarbon ions up to $C_{18}H_{15}^+$ species via C-C bond forming reactions is observed. The adduct formation route is found to be exothermic and barrierless, while other products are found to have energy barriers. The last topic addressed in this thesis is the experimental investigation of the possible formation mechanisms of the ion $C_{12}H_{10}O^+$, observed in benzene/air plasma corona discharges at atmospheric pressure.

Keywords

[ion-molecule reactions, aromatic hydrocarbons, planetary ionospheres, atmospheric pressure plasmas, mass spectrometry, ion beam, reactive cross section, rate constant]

Contributions by author

My personal contribution to this investigation was planning and performing the experiments. This includes sample preparations, optimization of ion optics and determination of the best experimental conditions to work at. I carried out the measurements on the energy dependences of reactive cross section as well as pressure dependences of reaction products using the home-built Guided-Ion Beam Mass Spectrometer (GIB-MS). I have also performed the measurements on the reactivity of $C_{10}H_7^+$, $C_{12}H_9^+$, $C_6H_6O^+$, $C_6H_5O^+$ and $OHC_6H_4^+$ ions with benzene (and C_6D_6) using a commercial triple quadrupole mass spectrometer. I performed the data analysis to extract information on absolute values of reactive cross sections, collision energy dependences, branching ratios for the molecular ions mentioned above. I took part in the discussion of the experimental results. Finally, I also took part in discussions regarding quantum chemistry calculations to interpret the obtained results.

List of publications

Included in thesis

- i. D. Ascenzi, **J. Aysina**, P. Tosi, A. Maranzana, G. Tonachini. Growth of polyaromatic molecules via ion-molecule reactions: an experimental and theoretical mechanistic study. *The Journal of Chemical Physics*, 133(18):184308, 2010.
- ii. D. Ascenzi, **J. Aysina**, P. Tosi, A. Maranzana, G. Tonachini. Experimental and theoretical study of the reactivity of $C_{12}H_9^+$ ion with benzene. *In preparation*.

Not included in thesis

- iii. D. Ascenzi, **J. Aysina**, E.-L. Zins, D. Schroder, J. Zabka, C. Alcaraz, S.D. Price, and J. Roithova. Double ionization of cycloheptatriene and the reactions of the resulting $C_7H_n^{2+}$ dications (n=6, 8) with xenon. *Phys. Chem. Chem. Phys.*, 13:18330, 2011.
- iv. E.-L. Zins, P. Milko, D. Schroder, **J. Aysina**, D. Ascenzi, J. Zabka, C. Alcaraz, S.D. Price, J. Roithova. Formation of Organo-Xenon Dications in the Reactions of Xenon with Dications Derived from Toluene. *Chemistry—A European Journal*, 17:4012, 2011.

Acknowledgments

The graduate school is like the next logical step after undergraduate studies. My first mentor, Prof. Alexandr Fishman, gave me fair warning of what to expect but it was still quite the journey. These three years have been filled with challenges, struggles, emotional turmoil, but I was fortunate enough to have an equal amount of rewards and accomplishments. I have learned so much and grown personally and professionally during this time and I owe it all to the people, who have supported me throughout the experience, encouraged and helped me to make my goal achievable. I am deeply grateful to all of them and pleased to acknowledge some people personally.

First of all, I would like to express my deepest gratitude to my supervisor, Dr. Daniela Ascenzi, for giving me the opportunity to work under her guidance. She introduced me to the fascinating area of science and always kept an eye on the progress of my work. She was always available for scientific discussion and has never stopped providing excellent advice and feedback. In addition, I am extremely grateful for her understanding throughout life's many ups and downs. I am also grateful for her invaluable patience with me and my thesis.

I would like to thank our group leader and my second supervisor, Prof. Paolo Tosi, who gave me the chance to carry out my PhD in his group. I have learned many lessons from scientific discussions with him.

Who has ever done experimental physics will know the value of technical support, and I have a lot to thank Damiano Avi. He has always been available, when I needed his help and advice. He was sharing his enthusiasm and knowledge with me.

I wish to thank all my friends for providing me the necessary breaks from work in the laboratory and making my life lively. I also want to express my gratitude to my relatives and friends in Russia. Being abroad I had fully understood that distance is a relative thing indeed. I always miss you.

Finally I am greatly indebted to my mom for encouraging and supporting me to find

my own path of life. Without her I would not be where I am now. You are always in my heart.

I have more people to thank for helping me during my research and my time in Trento. I would like to express my apology and hearty thanks to those of you who I could not mention by name.

Contents

Abbreviations	ix
List of figures	x
List of tables	xvii
1 Introduction	1
1.1 General motivations and outline of thesis	4
2 Experimental Techniques and Procedures	7
2.1 Introduction	7
2.2 GIB-MS setup	8
2.3 API-3000 setup	12
2.4 Data evaluation	14
3 Quantum Chemical Calculations	19
3.1 Introduction	19
3.2 Density functional theory	20
4 Results and discussion	25
4.1 Reactivity of $C_{10}H_7^+$ ion with benzene	25
4.1.1 Introduction	25
4.1.2 Experimental results	26
4.1.3 Theoretical results and reaction mechanisms	34
4.1.4 H/D scrambling	39
4.1.5 Conclusion	42
4.2 Reactivity of $C_{12}H_9^+$ ion with benzene	43
4.2.1 Introduction	43

4.2.2	Experimental results	43
4.2.3	H/D scrambling	48
4.2.4	Theoretical results and reaction mechanisms	49
4.2.5	Conclusion	53
4.3	Formation of $C_{12}H_{11}O^+$ ion	55
4.3.1	Introduction	55
4.3.2	Theoretical results and reaction mechanisms	59
4.3.3	Experimental results	62
4.3.4	H/D scrambling	66
4.3.5	Supplementary data	67
4.3.6	Conclusion	69
	Bibliography	71

Abbreviations

APCI	Atmospheric Pressure Chemical Ionization
CAD	Collisionally Activated Dissociation
CE	collision energy
CID	Collision Induced Dissociation
CM	center-of-mass energy
DBD	dielectric barrier discharge
DFT	Density Functional Theory
EBDS	Electron Beam Dry Scrubbing
EI	Electron Impact
FWHM	full width at half maximum
GC	gas chromatography
GIB-MS	Guided-Ion Beam
HACA	Hydrogen Abstraction ACetylene Addition
ISO	Infrared Space Observatory
LAB	laboratory energy
MS	mass spectrometer
PAHs	Polycyclic Aromatic Hydrocarbons
SE	Semiempirical Methods
VOC	volatile organic compound

List of Figures

2.1	Schematic view of a mass spectrometer.	8
2.2	Schematic view of the GIB mass spectrometer.	9
2.3	The reduced effective potential of an octopole and quadrupole radiofrequency trap as a function of the fractional distance between the center of the device and the rods. (taken from [82], Courtesy of <i>J. Am. Soc. Mass. Spectrom.</i>)	11
2.4	Schematic drawing of an atmospheric pressure chemical ionization source. (Courtesy of <i>Life Technologies Corporation.</i>)	12
2.5	Schematic representation of the gas inlet system created for injection of reagent gases different from N_2 in the collision cell of the API-3000 the original CAD gas flow control and CAD cell are highlighted by a dashed rectangle.	14
2.6	Retarding field analysis of the primary beam at m/z 153.	18
4.1	MS spectrum of ionic products from the reaction of mass-selected $C_{10}H_7^+$ ions with C_6H_6 recorded by GIB-MS at a collision energy $E_{CM} \sim 0.2$ eV in the center of mass frame and with $\sim 1.8 \times 10^{-4}$ mbar (black) and 8×10^{-4} mbar (red) of benzene in the reaction cell. The signal intensity of the parent ion (100%) is off-scale.	26
4.2	MS spectrum of ionic products from the reaction of mass-selected $C_{10}H_7^+$ ions with C_6H_6 recorded by GIB-MS at a collision energy $E_{CM} \sim 0.46$ eV in the center of mass frame and with $\sim 2 \times 10^{-4}$ mbar (black) and 8×10^{-4} mbar (red) of benzene- d_6 in the reaction cell. The signal intensity of the parent ion (100%) is off-scale.	27

- 4.3 MS spectrum of ionic products from the reaction of mass-selected $C_{10}H_7^+$ ions with C_6H_6 recorded by API-3000 at a collision energy $E_{CM} \sim 1$ eV (CE 3.6 in the lab) in the center of mass frame and with $\sim 9.5 \times 10^{-4}$ mbar of benzene in the reaction cell. The signal intensity of the parent ion (100%) is off-scale. 29
- 4.4 Density dependences of: (a) $C_{16}H_{12}^+$ and (b) $C_{15}H_{10}^+$ products after the reaction of $C_{10}H_7^+$ with C_6H_6 at a collision energy of about 0.2–0.3 eV in the center of mass frame. Dashed lines are linear fits of the data. 30
- 4.5 Cross sections as a function of the collision energy for the reaction of $C_{10}H_7^+$ with C_6H_6 leading to the following products: (a) $C_{16}H_n^+$ with $n=13-10$; (b) $C_{15}H_{10}^+$, $C_{15}H_9^+$, $C_{14}H_{10}^+$ and $C_{13}H_9^+$. Red points corresponds to the absolute values of the cross sections for channels (2) and (5), directly obtained from analysis of data shown in Fig. 4.4. Lines in (a) are guide for the eye indicating a dependence E_{CM}^{-1} (green) and $E_{CM}^{-1.3}$ (blue). 31
- 4.6 MS spectra of products from the reactions of $C_6H_5^+$ (in black) and $C_{10}H_7^+$ (in red) with benzene, recorded by API-3000 at an E_{CM} of ~ 1 eV and benzene pressure $\sim 10^{-4}$ mbar. Ions $C_6H_5^+$ and $C_{10}H_7^+$ (relative intensities 100%, out of scale) have been generated in the APCI source from chlorobenzene and 1-chloronaphthalene precursors respectively. 32
- 4.7 MS/MS spectrum of the m/z 205 ion generated by infusion of phenyl-naphthalene in the APCI source, using N_2 as CAD gas at a pressure $\sim 10^{-3}$ mbar and a nominal collision energy of 28 eV in the LAB. 33
- 4.8 Structures and energies of the most relevant stationary points on the reactive potential energy surface leading from $C_{10}H_7^+$ plus benzene to $C_{15}H_{10}^+$ (structure **10**) plus CH_3 . Hydrogen atoms are explicitly indicated when they are involved in shifts or gradual CH_3 formation. Energies are in kcal mol $^{-1}$ 35
- 4.9 The alternative pathway leading to methyl loss from $C_{16}H_{13}^+$ (structure **9**) with formation of $C_{15}H_{10}^+$ in an isomeric structure with respect to **10** (described in Scheme 4.8). Hydrogen atoms are explicitly indicated when they are involved in shifts or gradual CH_3 formation. Carbon atoms involved in bond breaking/bond forming steps are highlighted with red and green dots. Energies are in kcal mol $^{-1}$ 37

4.10	Structures and energies of the hydrogen migrations along the rings of the $C_{16}H_{13}^+$ adduct. Shifting hydrogens are explicitly indicated. Energies are in kcal mol ⁻¹	38
4.11	The alternative pathway leading to methyl loss from the naphthylum moiety. Hydrogen atoms are explicitly indicated when they are involved in shifts or gradual CH_3 formation. Energies are in kcal mol ⁻¹	39
4.12	MS spectrum of ionic products from the reaction of mass-selected $C_{10}H_7^+$ ions with C_6D_6 recorded by API-3000 at a collision energy E_{CM} 1 eV in the center of mass frame (3.6 eV in the lab) and with 9.5×10^{-4} mbar of benzene- d_6 in the reaction cell. Red bars represents the calculated intensities corresponding to a complete randomization of position of H and D atoms in the ions $C_{15}(H, D)_{10}^+$ and $C_{12}(H, D)_{11}^+$ formed according to reactions (5) and (9) respectively.	40
4.13	Experimental intensities of products from the reaction of $C_{10}H_7^+$ with C_6D_6 are compared with calculations assuming a complete randomization of the H and D atoms in the $C_{16}H_7D_6^+$ complex prior to dissociation leading mainly to $C(H, D)_3$ loss.	41
4.14	Structures of various polyphenyl molecules.	43
4.15	Mass spectrum of selected $C_{12}H_9^+$ ions reacting with $\sim 10^{-3}$ mbar of C_6H_6 (a) recorded by API-3000 at a collision energy $E_{CM} \sim 1$ eV in the CM frame. Mass spectra (b) of selected $C_{12}H_9^+$ ions colliding with benzene (red) and with N_2 (blue at a collision energy of 20 eV in the lab frame and black at a collision energy of 4 eV in the lab frame. The signal intensity of the parent ion (100%) is not shown.	44
4.16	Possible mechanism of the $C_{18}H_{15}^+$ ion formation.	44
4.17	Normalized ion yields as a function of the collision energy (in the LAB frame) for the primary and product ions of the reaction of massselected $C_{12}H_9^+$ with C_6H_6 (a) and of the reaction of mass selected $C_{10}H_7^+$ with C_6H_6 (b).	46
4.18	Comparison between reactivities of $C_6H_5^+$, $C_{10}H_7^+$ and $C_{12}H_9^+$ ion colliding with 10^{-4} mbar of benzene. The signal intensity of the parent ion (100%) is not shown.	47

4.19	Mass spectrum of selected $C_{12}H_9^+$ ions reacting with $\sim 10^{-3}$ mbar of C_6D_6 recorded at a collision energy of 3.7 eV in the lab frame (a). The signal intensity of the parent ion (100%) is not shown. Comparison (b) between the experimental and calculated intensities in the mass region of $C_8(H, D)_7^+$ products. The calculated intensities correspond to a complete scrambling of the 9 H and 6 D atoms over the three rings prior to fragmentation.	49
4.20	Preliminary steps: adduct formation, phenyl migration, and formation of a central 5-membered cycle and methynic bridge. Energies are in kcal mol $^{-1}$	51
4.21	Central steps, with temporary linking of the two external phenyl rings. Energies are in kcal mol $^{-1}$	52
4.22	Final steps: phenyl migration, formation of the naphthalene framework (in 11), and final fragmentation. Energies are in kcal mol $^{-1}$	53
4.23	GC-MS analysis of the solid deposit obtained from the DBD treatment of a C_6H_6 mixture with 4 % of O_2 (phenol intensity off scale in the figure).	55
4.24	Positive ion mode mass spectra from the corona discharge source operating with: (a) benzene and (b) deuterated benzene. Air is used as nebulizer gas in both cases, and benzene injection flow is 0.1 mL/min.	56
4.25	Mechanism proposed for the formation of the ion observed at m/z 171.	57
4.26	Reaction of mass selected $[C_6H_6O]^+$ (m/z 94) ions with C_6H_6 at a collision energy of 4 eV in the lab frame. The reacting $[C_6H_6O]^+$ ion was generated in two different ways: (a) by ion-molecule reaction in the APCI source fed with C_6H_6 and air; (b) by ionization of phenol in the APCI source. The pressure of benzene was about 10^{-3} mbar. The signal intensity of the parent ion (100%) is off-scale.	58
4.27	Mechanism proposed for the formation of the ion observed at m/z 171 through the reaction of phenoxy $C_6H_5O^+$ ions with benzene.	59
4.28	Mechanism proposed for the formation of the ion observed at m/z 171 through the reaction of hydroxyphenyl $OHC_6H_4^+$ ions with benzene.	59
4.29	Phenoxy ions ($C_6H_5O^+$) produced from anisole (a) and $OHC_6H_4^+$ ions produced from p-bromophenol (b) in EI or APCI source.	59
4.30	Structures and energies of isomeric $[C_6H_5O]^+$ ions.	60
4.31	Schematic representation of the $C_6H_5O^+ + C_6H_6$ potential energy profile. Energies (ΔG^0) are given in eV at temperature of 298 K relative to the sum of energies of reactants.	61

- 4.32 Schematic representation of the $OHC_6H_4^+ + C_6H_6$ potential energy profile. Energies (ΔG^0) are given in eV at temperature of 298 K relative to the sum of energies of reactants. 63
- 4.33 MS spectra of ionic products from selected $C_6H_5O^+$ ions (blue) and $OHC_6H_4^+$ ions (red), produced from anisole and p-bromophenol in the APCI source (a) and in the EI source (b), colliding with 10^{-4} mbar of C_6H_6 at a collision energy of 1 eV in the centre of mass frame. The signal intensity of the parent ion (100%) is off-scale. 64
- 4.34 Cross sections as a function of the collision energy for the reaction of $C_6H_5O^+ + C_6H_6$ leading to the following products: $C_{12}H_{11}O^+$, $C_{12}H_9^+$ and $C_{11}H_{11}^+$ 65
- 4.35 Density dependences of $C_{12}H_9^+$ product from the reaction of $C_6H_5O^+$ ion with C_6H_6 at a collision energy of ~ 0.64 eV in the center of mass frame. Dashed line is linear fit of the data. 65
- 4.36 Comparison between the experimental (black and red lines) and calculated - red hatched bars intensities in the mass region of $C_{12}(H, D)_9^+$ products from the reaction of $C_6H_5O^+$ or $OHC_6H_4^+$ ions with C_6D_6 67
- 4.37 Schematic representation of commercial samples: (a) 3-phenylphenol, (b) 2-phenylphenol, (c) 4-phenylphenol, (d) diphenyl ether. 67
- 4.38 MS/MS spectra of selected $C_{12}H_{11}O^+$ ion produced from 2-, 3- and 4-phenylphenol colliding with $\sim 1.8 \times 10^{-4}$ mbar of nitrogen at a collision energy of 18 eV in the lab frame. The signal intensity of the parent ion (100%) is off-scale. 68
- 4.39 MS/MS spectra of selected $C_{12}H_{11}O^+$ ion produced from C_6H_6 /air, phenylphenol and diphenyl ether colliding with $\sim 1.8 \times 10^{-4}$ mbar of N_2 at a collision energy of 18 eV in the lab frame. The signal intensity of the parent ion is off-scale. 68
- 4.40 Linear combination of 94% of isomeric phenylphenol (indicated as PP) and about 6% of diphenyl ether (indicated as DE) and MS/MS spectrum of the m/z 171, produced in the APCI source from a C_6H_6 /air mixture. The signal intensity of the parent ion (100% is off-scale). 69

List of Tables

4.1	Branching ratios for formation of the various product channels observed upon reaction of $C_{10}H_7^+$ with benzene- h_6 at the following conditions: (a) GIB-MS, benzene pressure 1.8×10^{-4} mbar, (b) GIB-MS, benzene pressure 8×10^{-4} mbar, (c) API-3000, benzene pressure 9.5×10^{-4} mbar.	28
4.2	Branching ratios for formation of the various product channels observed upon reaction of $C_{12}H_9^+$ with benzene- h_6 at a benzene pressure of 10^{-3} mbar.	46
4.3	Branching ratios for formation of the various product channels observed upon reaction of both $OHC_6H_4^+$ and $C_6H_5O^+$ ions with 10^{-4} mbar pressure of C_6H_6 by API-3000.	64

Chapter 1

Introduction

Laboratory studies on the chemistry of planetary atmospheres and the interstellar medium have been historically focussed mainly on small and simple molecules, such as benzene. The latter has been detected in the atmospheres of Jupiter, Saturn and Titan by using the Infrared Space Observatory (ISO) [1, 2]. In more recent years the attention has shifted towards larger molecules, mostly of organic nature. Among them, a special place is reserved to polycyclic aromatic hydrocarbons (PAHs).

Polycyclic aromatic hydrocarbons may form in various environments, both terrestrial and extraterrestrial. They have been detected in the interstellar space [3, 4], where they are claimed to be responsible for an emission band in the UV region (at 217.5 nm) [5], while it is still an open question the contribution of PAHs to the so-called “diffuse” interstellar bands (DIBs) [5, 6, 7, 8, 9]. A few studies on chemical reactivities of PAHs have shown that these molecules are stable in the interstellar medium [10, 11, 12]. Thereby they might play a role in the extraterrestrial synthesis of complex biomolecules, which in turn might be the building blocks of life. Thus in the past few years understanding how these ubiquitous molecules are formed has become an increasingly important research topic.

The Cassini-Huygens mission [13] has shown that Titan has one of the richest atmospheric chemistry in the solar system. Its extensive atmosphere is composed mostly of N_2 with CH_4 (2%) and H_2 (0.4%) being the most abundant minor constituents [14, 15]. Different types of hydrocarbons [16, 17], nitrogen-bearing species [18], and oxygen-bearing species [19] complete the list of compounds that exist in Titan’s atmosphere. Moreover heavy ions with masses over 100 amu have been detected in significant amounts on Titan’s ionosphere below 1200 km [20]. Due to the possible chemical structures PAHs, nitrile aromatic polymers [21], fullerenes [22] and polyphenyls [23] have been proposed as precursors

for aerosols formations.

PAHs also are ubiquitously present in the terrestrial environment. They are found in air [24], soil [25, 26], groundwater [27] and they can infect food due to the fact that several PAHs are known to be carcinogens and mutagens. PAHs released into the environment may be originated from different sources like gasoline, diesel fuel combustion [28], tobacco smoke [29]. But the major contributors for PAH releases are petroleum refining and transport activities [30]. These loadings can happen through dumping of industrial effluents and through fortuitous release of raw and refined products. In general PAHs are formed during the incomplete combustion of organic materials, where they act as intermediates in the formation of soot particles [31]. Soot formation is a complex process that usually involves decomposition of hydrocarbons in the fuel and formation of small aromatic hydrocarbons from the decomposition products followed by their growth to compounds with a larger number of rings. After the formation of the large aromatic hydrocarbons several processes follow such as inception of the first particles, growth of soot particles due to reactions with gas phase species, particle coalescence, agglomeration and oxidation. Then fine soot particles can carry PAHs deep into the lungs. The ubiquitous distribution of PAHs and their potentially deleterious effects on human health are at the basis of the increased interest in the search for destruction mechanisms of PAHs. For instance, the mechanical way to remove soot from the exhaust gas of a diesel engine is through the use of particulate filters. Another way of reducing the formation of PAHs is through tchemical action (e.g. catalytic combustion [32], biodegradation [33]).

Recently it has been shown that plasmas can be applied for the removal of PAHs as well as several other organic pollutants. There are many techniques based on cold plasmas, which are used in air pollution control for the removal of harmful compounds [34, 35, 36]. In addition, plasmas can be used in hydrocarbon reforming [37], hydrogen production out of liquid fuel [38], for deposition of advanced materials [39], for film growth and particulate formation, and for improvements of ion sources for mass spectrometry techniques. Thus the complex chemistry occurring in gaseous discharges at atmospheric pressure becomes an interesting research area and hence the knowledge of plasma by-products becomes an important issue.

To model the formation and degradation of PAHs in extraterrestrial and terrestrial environments a detailed knowledge of the chemistry of PAH synthesis and oxidation at high and low temperatures and pressures is needed. In particular, the interstellar medium and planetary atmospheres are characterised by low temperatures and small pressures,

while combustion systems and cold plasmas are high pressure systems characterised by high and low temperatures respectively.

Several mechanisms have been proposed for PAHs formation in the high temperature environment of combustion chambers and flames. The most established one is the so-called HACA mechanism [31, 40, 41]. The acronym HACA stands for Hydrogen Abstraction ACetylene Addition and refers to a mechanism in which radicals formed during the combustion process are able to abstract an hydrogen atom from a precursor benzene ring. Subsequently the so-formed phenyl radical can add acetylene molecules to close a second ring onto the benzene one and form naphthalene. Similar mechanisms will cause the production of higher-order PAHs. However, the HACA mechanism presents high energy barriers, which makes it feasible only at high temperatures. In fact the formation of PAHs in flames generally does not occur until the temperature is at least 1200-1600 K. Therefore, the same mechanism cannot be hold responsible for PAHs synthesis at the low temperatures of the interstellar space. Indeed, the extreme conditions in extraterrestrial environment have several limitations for the occurrence of gas phase reactions. The low temperatures rule out endothermic reactions (or exothermic reactions with activation barriers), and low density prevents three-body processes. Thus, the dominant processes in the gas-phase chemistry of interstellar space are exothermic reactions without any activation barriers. The most common type of barrierless reactions are ion-molecules reactions [42]. In the interstellar medium ions can be formed by a variety of the processes. One of the processes is ionization by cosmic ray photons. The reaction rates of ion-molecule reactions at low temperatures exceed by orders of magnitude the reactions rates of gas-phase neutral reactions. Consequently, molecular formation involving ions rather than neutrals may be favoured under extraterrestrial conditions [43] and therefore ion chemistry plays an important role even in the synthesis of organic molecules. Besides growth routes based on singly charged ions [44], with a special relevance to Titan's atmosphere, bond-forming reactions of $C_m H_n^{2+}$ dications with methane have been proposed as a potential formation route of the so-called pre-formed building blocks. Thus the sequential post association of such units into PAHs can be possible [45, 46, 47, 48].

The growing mechanisms of molecular systems initiated by charged particles is also relevant for modelling the ion chemistry occurring in atmospheric pressure plasmas [49]. For instance it was shown that ion-molecule reactions are relevant for understanding the chemical mechanisms of plasma polymerization processes [50]. Plasmas appear to be dominated by reactions of neutral and radical species, whose densities can be larger by

orders of magnitude than that of ions. However, the small density of ions can be balanced by their higher reactivities, which can exceed those of neutral species [51, 52].

With special reference to PAHs, it was recently shown that in some experiments on electron beam industrial gas cleaning of harmful impurities, such as the electron beam dry scrubbing (EBDS) process, an increase in the concentrations and sizes of polycyclic aromatic hydrocarbons is observed, rather than their expected and sought after destruction [53, 54]. The growth is the result of formation of larger PAHs from simpler ones during the processing. The EBDS process, similar to cold plasma treatments, occurs at low gas temperatures and therefore the HACA mechanism does not play a significant role in the dynamics of PAH growth, due to the already mentioned high energy barriers relative to the H abstraction steps. In such conditions an ionic mechanism of condensation of aromatic compounds can be more suited to describe the chemistry of PAH synthesis.

We can therefore conclude that ion chemistry should be taken into account as a competitive mechanism for PAH synthesis in cold plasmas as well as in the interstellar medium and planetary atmospheres.

1.1 General motivations and outline of thesis

Our contribution to the study of possible growing mechanisms of aromatic hydrocarbons in Titan's atmosphere, the interstellar medium or cold atmospheric pressure plasmas is the investigation of association processes involving naphthyl $C_{10}H_7^+$ and biphenylium $C_{12}H_9^+$ cations with benzene. In both studies the growth of hydrocarbon ions were observed via C–C bond forming reactions. The study on the reactivity of naphthyl cation $C_{10}H_7^+$ with benzene is reported in Section 4.1 and in Ref. [55]. Recent measurements about the reactivity of the $C_{12}H_9^+$ ion with benzene show that the structure of the association product corresponds to the structure of polyphenyls and not to PAHs. This study will be discussed in Section 4.2.

With regard to chemical processes in cold plasmas, the study of oxidation processes of aromatic compounds is also of significant interest. It is well-known that benzene can be efficiently converted into phenol in non thermal atmospheric plasma [49, 56, 57]. Apart from phenol various oxygenated products are observed in benzene/air dielectric barrier discharge. The study of the possible mechanisms for formation of the oxygenated product ion $C_{12}H_{10}O^+$ observed in such plasma is given in Section 4.3.

To study ion-molecule reactions guided ion beam tandem mass spectrometers, which

allow selection and manipulation of both reactant and product ions to investigate reaction mechanisms, are used (see Chapter 2). The use of theoretical calculations to calculate energy and structures of the most relevant points on the reactive potential hypersurface is discussed in light of density functional theory.

The outline of the thesis is as follows. The next Chapter 2 presents a brief introduction on mass spectrometric techniques, a detailed description of the experimental set-ups used throughout this thesis and data collection and evaluation procedures. Chapter 3 explains the general idea of density functional calculations. Chapter 4 presents the motivations for the individual systems of investigation, the detailed experimental results and their interpretation also on the basis of theoretical modelling.

Chapter 2

Experimental Techniques and Procedures

This chapter will give a general but brief description of mass spectrometry techniques and of the experimental setups, which were used to perform the measurements, described in Chapter 4. The reactions of cations with neutrals were investigated by using both a home-built Guided-Ion Beam Spectrometer (GIB-MS) and a triple quadrupole mass spectrometer API 3000 LC/MS/MS (in the following indicated as API-3000), AB Sciex, USA equipped with an atmospheric pressure chemical ion source (APCI). The data analysis procedures, used to extract absolute value of cross sections, rate constants, and branching ratios from the measurements will be presented.

2.1 Introduction

Mass spectrometers are powerful analytical instruments that serve as the gold standard for chemical analysis. The first mass spectrometer was reported in 1910 and was followed by 40 years of modest innovations [77]. Before the 1950's, mass spectrometers only had a few applications in physics and chemistry, but this was soon changed with the growth of the petroleum industry. Commercialization of the mass spectrometer for chemical analysis pushed the rapid development of this tool. In turn, emphasis shifted from the physics of the device to finding new applications. Today, mass spectrometers are utilized in industrial processing, environmental monitoring, national security, space exploration, healthcare and characterization of proteins and biomolecules.

A typical mass spectrometer consists of four main components: an ion source, a mass

analyzer, a detector, and a vacuum pump system (see Fig. 2.1). The principle on which the mass spectrometer based is the following. The molecular ion is formed by ionization of a gas sample to be analyzed and the ion source plays a key role in obtaining a mass spectrum. Then ions enter the mass analyzer, where they are sorted depending on their mass to charge ratios (m/z). A system of electrostatic lenses is generally used to focus ions produced in the source and then to guide them through the apparatus into a detector, where they are collected and counted. If we plot the detector count as a function of the specified m/z , we will generate a mass spectrum for the sample. This spectrum will provide information on the relative quantities of each m/z within the sample, and serves as a chemical “*finger print*”. The last major component is the vacuum pump, which keeps the other three components under vacuum (usually using a differential pumping between the ion source and the detector). A schematic view of a typical mass spectrometer is shown in Figure 2.1.

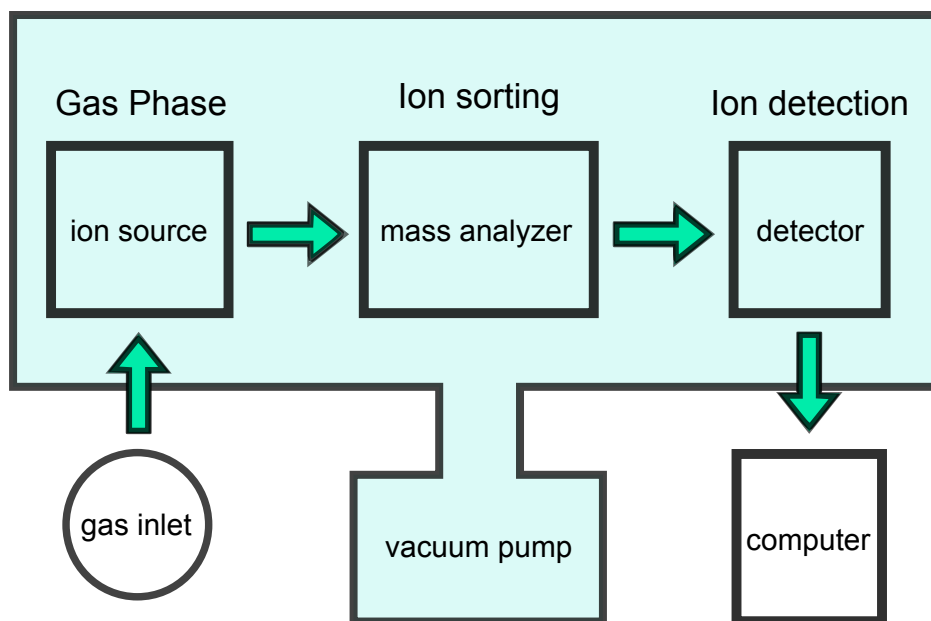


Figure 2.1: Schematic view of a mass spectrometer.

2.2 GIB-MS setup

The guided ion beam setup is a tandem mass spectrometer with an $O_1Q_1O_2Q_2$ configuration (Q stands for quadrupole and O -for octopole), which allows the measurement of integral cross sections for ion-molecule reactions as a function of the collision energy in

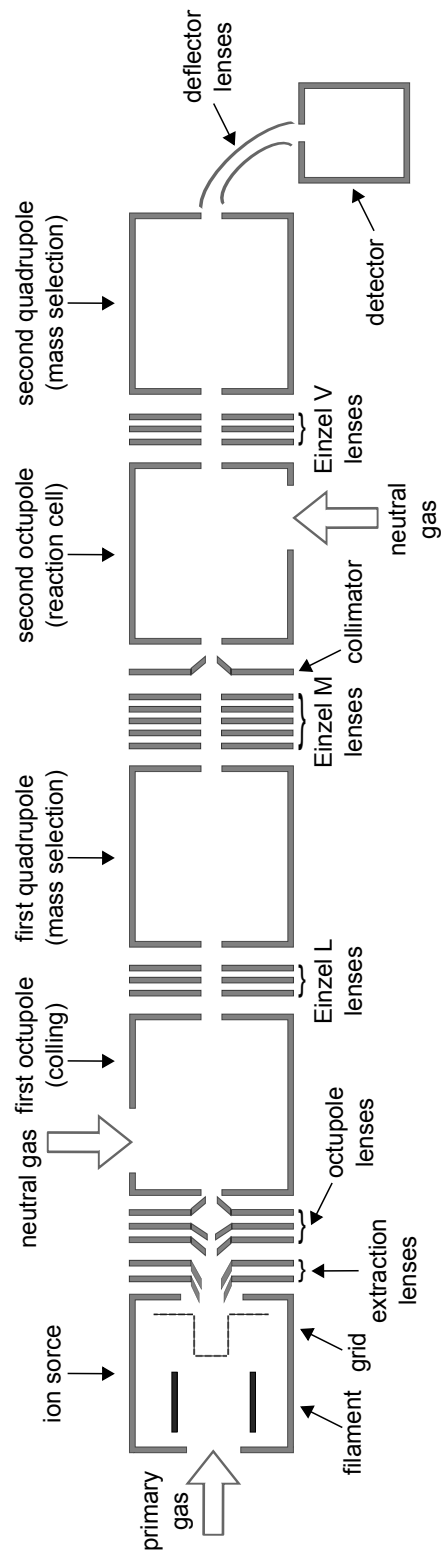


Figure 2.2: Schematic view of the GIB mass spectrometer.

the range from about 0.1 to about tens/hundreds eV in the center of mass. Positive ions are generated in an electron impact source (EI). In this type of source an incandescent filament made of tungsten emits a high-energy beam of electrons (in the range of 70–100 eV), accelerated towards an anode, which is placed on the opposite of the filament side. These electrons collide with the electron cloud of the molecule and thus may transfer enough electron energy to remove another electron from that molecule. EI ionization usually produces singly charged ions containing one unpaired electron. A charged molecule which remains intact is called the molecular ion. Energy imparted by the impact with electron and, more importantly, instability in a molecular ion can cause that ion to break into smaller pieces (fragments). Then ions are extracted by a set of conical extractor lenses, to be injected into a first octopole Q_1 (length 8.2 cm, radius 0.9 cm), which is used as an energy quencher. The octopole is surrounded by a cell, which can be filled with an inert gas (for instance, He or Argon). In this way reagent ions produced in excited states can quench their internal energy by collisions with the inert partner. After the cooling stage, an Einzel lens transport the ions into a first quadrupole Q_1 , which is used to mass-select the primary ion beam. The chosen reactant ions are injected into the second octopole O_2 ion guide (length 10.2 cm, radius 0.6 cm) by a six-element accelerating/decelerating cylindrical lens, whose last element has a conical shape to limit the angular divergence of the ion beam entering the octopole to 41° . The octopole utilizes eight rods arranged in an octagonally symmetrical array around the ions. In the direction perpendicular to the axis of the rods the potential, created by applying radio frequency (rf) electric potentials in opposite phases to alternate rods, produce an inhomogeneous field, which creates an effective radial potential well. In this way scattered reactant and product ions are well trapped and can be collected with enhanced efficiency. In addition, the energy region can be extend from about 1 eV in the laboratory frame down to thermal energies (0.04 eV can be found in Ref. [78]). Such inhomogeneous radiofrequency devices were pioneered by Gerlich [78] and Teloy [79] and more details can be found in the review by Gerlich [80]. We chose an octopole over the conceptually similar rf-only quadrupoles because a more homogeneous trapping field can be obtained with more rods. It was shown that the time-averaged radial trapping field of a rf multipole device varies as r^{p-2} , where r is the distance from the center of the device and p is the number of poles [81]. Thus for the octopole (an instrument having $p=8$ poles) the produced field varies as r^6 and it ensures a large tubular trapping volume (see Fig. 2.3) and steep walls. These characteristics result in effective ion trapping with only small perturbations of the kinetic energies of ions,

traveling down the axis of the octopole. An effective trapping field for a quadrupole is quadratic and varies as r^2 (see Fig. 2.3). The maximum trapping energy (or the depth of the trapping field) for the quadrupole (varies as $(p/2)^2$ [82]) at $r=r_0$ is one-fourth that of the octopole. This makes the quadrupole ion trapping less efficient and yields larger perturbation on the kinetic energy of the ions compared to octupole trapping. Thereby, for the quantitative measurements of the energy dependence of cross section the octopole trapping field is more desirable than a quadrupole field.

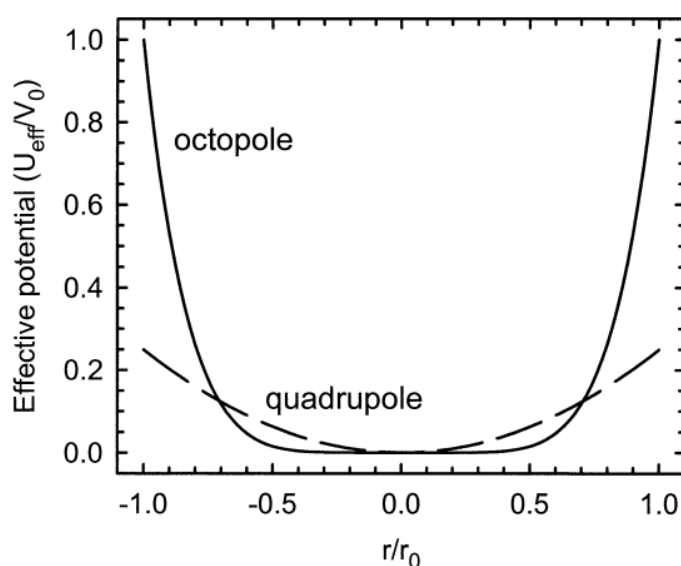


Figure 2.3: The reduced effective potential of an octopole and quadrupole radiofrequency trap as a function of the fractional distance between the center of the device and the rods. (taken from [82], Courtesy of *J. Am. Soc. Mass. Spectrom.*)

The second octopole is surrounded by the scattering cell filled with neutral gas, where mass-selected ions can react with neutrals. Neutrals are introduced in the scattering cell as a vapors through a leak valve with the pressure generally set in the range of 10^{-5} mbar (monitored by a spinning rotor gauge *SRG2 MKS Instruments, USA* [83]) to ensure that products are the result of single collision conditions. Product ions and primary ions are collected by the lens system between the octopole O_2 and the quadrupole Q_2 . These lenses need to efficiently transport ions, which may have large radial velocities because of the rf voltages, emerging from the octopole O_2 into the last quadrupole Q_2 . After a 90° deflection, product ions and primary ions are detected by an electron multiplier.

In general the advantage of the use of the ion beam technology is to be able to control the kinetic energy of the reactant ion. In our GIB-MS the kinetic energy of the projectile

ion beam can be varied easily over a wide range from practically 0 to several tens of eV simply by changing the voltage difference between the region where the ions are formed and where they react (basically, the DC bias potential of O_2). Using the retarding potential analysis (described later and also in Ref. [81]) the energy scale can be calibrated and the energy spread of the ion beam can be measured. In this way the collision energy is determined. Such a large tuneability in the collision energy, achievable with the GIB-MS set up, allows us to perform bond-activation energy measurements and to probe the potential energy surfaces and thus the reaction mechanism.

2.3 API-3000 setup

In the experiments performed with API-3000, reactant ions are generated in an atmospheric pressure chemical ion (APCI) source. A suitable neutral-precursor is injected via a micrometric syringe pump, with injection flows in the range of 1–10 l/min as solution in an appropriate solvent (e.g. methanol). Measurements are performed with the source heated usually at 300–400 °C. Such high temperature used to ensure a rapid evaporation. A high velocity jet of nebulizer gas flows coaxially over the sprayer to disperse the sample as a mist of fine particles. The gaseous sample and solvent molecules are swept from the probe by auxiliary gas flow into the reaction region of the ion source, where the electrons emitted by the corona discharge needle initially ionize the sample and solvent. High purity N_2 is used as nebulizer and curtain gas and obtained by the boil-off from a liquid nitrogen Dewar. Then the vaporized solvent molecules collide with the sample molecules to produce stable sample ions $(X+H)^+$ (see Figure 2.4). Then ions drift under the influ-

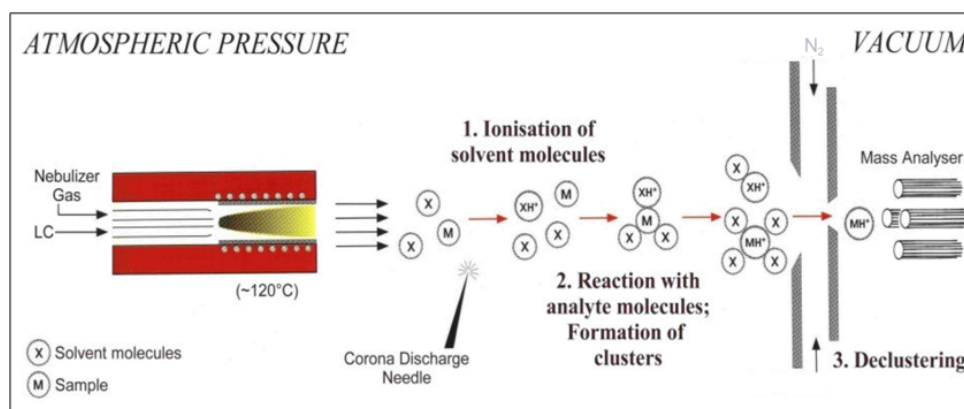


Figure 2.4: Schematic drawing of an atmospheric pressure chemical ionization source. (Cortesy of *Life Technologies Corporation*.)

ence of the electric field in the direction of the curtain plate and through the gas curtain into the mass analyzer. The whole ion formation process is collision dominated because of the pressure of the APCI source. Except in the immediate vicinity of the needle tip, where the electric field strength is greatest, the energy imparted to an ion by the electric field is small in comparison with its thermal energy. In most of our experiments the declustering potential voltage plays an important role. The higher the declustering potential voltage the greater the energy imparted to the ions entering the analyzing region of the mass analyzer. This energy helps to decluster the ions and increasing the voltage beyond optimal conditions can induce fragmentation before the ions enter the mass filters. In this way the dissociation does not occur in the source, since there is not enough energy, but it is due to collision with nitrogen in the declustering region.

The advantage of producing positive ions via the corona discharge of the APCI source rather than by EI in the GIB-MS ion source relies in the lower degree of internal excitation attained by the primary ion, as can be demonstrated by the absence of unimolecular fragmentation of the primary ion to lower mass fragments during the flight from the source to the detector.

After the source the ions of interest are mass-selected with the first quadrupole Q_1 and injected into the second quadrupole Q_2 which acts as an ion guide and which is surrounded by the scattering cell where the neutral partner is admitted at a typical pressure in the range of 10^{-5} – 10^{-3} mbar. In standard operating conditions the API-3000 operates with N_2 as collisionally activated dissociation (CAD) gas in the collision cell and its pressure can be controlled by means of four separate valves with different diameters that operate on a “go/no go” basis. N_2 admitted in the collision cell is redirected from the differentially pumped interface vacuum line and derives from a splitter in the curtain gas supply line. To admit a gas different from N_2 into the CAD cell of the API-3000 instrument the gas injection line was modified by addition of a separate interface vacuum line pumped by a 70 l/s turbo pump backed by a 83 l/min scroll pump and gas inlet system, as shown in Figure 2.5.

Reagent gases or vapors in equilibrium with volatile liquids are stored in small glass cylinders labeled as reagent gas **1** or reagent gas **2** in the figure and the flow in the CAD cell is manually regulated by a variable leak valve (MDC Vacuum products, all metal MLV series, variable leak rate from 10^{-2} to 10^{-7} mbar l s $^{-1}$). When a reagent gas is admitted in the collision cell, the CAD gas flow controller is by-passed (the on/off valve vA is closed), while valves vB and vC are open and any contamination of the CAD gas flow controller

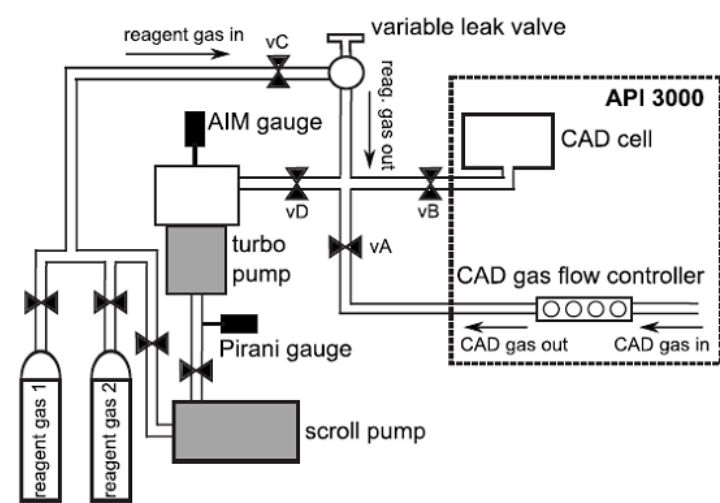


Figure 2.5: Schematic representation of the gas inlet system created for injection of reagent gases different from N_2 in the collision cell of the API-3000 the original CAD gas flow control and CAD cell are highlighted by a dashed rectangle.

with the reagent gas is avoided. This is particularly useful to avoid memory effects when working with reagent gases having high sticking coefficients. By closing the variable leak valve, together with valves vC and vD, and opening valves vA and vB, the systems revert quickly to standard operating conditions and N_2 can be admitted in the collision cell. Ionic products emerging from Q_2 are mass-analyzed by scanning the third quadrupole Q_3 and later detected by a channel electron multiplier.

2.4 Data evaluation

GIB-MS experiments

In our experiments the raw data are reactant/product ion intensities (both with and without gas in the cell) as a function of the ion kinetic energy and as a function of the pressure of the neutral partner. To use these data several transformations are needed. The kinetic energy of the ion is measured in the laboratory frame and appropriate conversion to the center-of-mass energy is performed to get the energy available to the reaction system for chemical transformations. Converting the ratio of product and reactant ion intensities, measured as a function of the neutral target pressure, absolute value of reactive cross section can be obtained [81, 82, 84]. The latter represents the intrinsic probability for reaction.

Conversion from laboratory to center-of-mass energies

It is important to know how much energy is available to the reaction system. The translational energy of the two colliding particles during reaction can be divided into the relative translational motion of the two reactants and the motion of the entire collision system through the laboratory. The latter part is conserved due to the conservation of linear momentum (the total mass of the system does not change during reaction). And so, there is no available energy to induce chemical change during the reaction. Therefore, the energy that is available for chemical reactions is the relative kinetic energy of the two particles (center-of-mass energy, E_{CM}). Due to the fact that the ion has an appreciable velocity, which is defined by its laboratory energy, E_{LAB} , whereas the neutral reactant is essentially stationary, the center-of-mass energy, E_{CM} , can be calculated as

$$E_{CM} = E_{LAB} \cdot \frac{m}{(M + m)}, \quad (2.1)$$

where m and M stand for the mass of the neutral target and the ionic projectile, respectively [84].

Conversion from ion intensities to cross sections

In collision theory the reaction cross section σ is an important quantity. It describes the probability that two particles (e.g., an ion and a neutral) collide and proceed to products. So it has units of area and represents an effective size of the ion-molecule collision pair.

The ratio between the measured signal intensities of product and reactant ions is proportional to the effective integral cross section and its absolute value can be measured, in a beam-cell experiment, according to the Lambert-Beer law. For low pressures of neutral target (thin target limit) the Lambert-Beer law can be approximated as

$$\frac{I_P}{I_0} = \sigma_P \cdot n \cdot l_{eff}, \quad (2.2)$$

where I_P and I_0 are the intensity of products P and reagent ions, respectively (with $I_P \ll I_0$), n is the neutral gas density in the collision cell, and l_{eff} is the effective length of the collision cell (equal to 12.0 ± 0.6 cm in our case). By measuring the slope of the

plot of I_P/I_0 as a function of the neutral gas density (at sufficiently low densities to ensure single collision regime), we can obtain σ_P for each of the reaction channels. In such type of measurements, the accuracy is limited by uncertainties in the measurement of the gas pressure and by error propagation due to the calibration procedure necessary to establish the value of l_{eff} . We estimate that absolute cross section values are accurate within $\pm 30\%$.

Branching ratios

The branching ratio BR for a particular channel is defined in Eq. 2.3 as the ratio of the fraction (or yield) of product ions formed by one channel with respect to the total amount of products formed by all channels.

$$BR_i = k_i/(k_1 + k_2 + k_3 + \dots k_i) = k_i/k \quad (2.3)$$

Hereby, the reaction cross section for individual product ions P can be given as

$$\sigma_P = \sigma_T \cdot BR_P, \quad (2.4)$$

where σ_T is the total reaction cross section, BR_P is the branching ratio for P channel.

Alternatively, given the total amount of products formed by all channels, the partial yield of product ions can be written as

$$k_i = BR_i \cdot k. \quad (2.5)$$

Conversion from absolute cross section values to rate constants

Absolute cross section values can be converted into phenomenological rate constant $k(\langle E \rangle)$ by using this expression

$$k(\langle E \rangle) = v \cdot \sigma_P(E), \quad (2.6)$$

where $k(\langle E \rangle)$ is the rate constant in $\text{cm}^3 \text{s}^{-1}$, σ_P is the reactive cross section for product channel P in cm^2 , $v = (2E/\mu)^{1/2}$ is the nominal center of mass velocity in cm s^{-1} , and μ is the reduced mass of the reactants in kilogram. Because of the kinetic energy distributions of the reagents, the rate constant can be better characterized as a function of the mean relative energy of the reactants, which is given by $\langle E \rangle = E + (3/2)\gamma k_B T$, where $\gamma = M/(M + m)$ and T is the neutral gas temperature. Because GIB-MS allows very low ion energies, the rate constant k at near room temperature for the reaction can be obtained directly from the data at the lowest energy.

Retarding potential analysis

How it was mentioned earlier in this Chapter the DC voltage of octopole establishes the laboratory kinetic energy of the ion. To use the data taken at low energies requires calibration of the energy scale. One of the methods to determine the kinetic energy is retarding potential analysis. To produce a retardation curve the ion beam intensity was taken as a function of the DC voltage of the octopole swept through the zero ion energy. Then the derivative of that curve gives the ion energy distribution.

API-3000 experiments

The kinetic energy of the charged ions entering the middle quadrupole Q_2 can be varied between 0 and 100 eV, which allows the investigation of ion-molecule reactions in different kinetic energy regimes, e.g. from quasi-thermal conditions to elevated kinetic energies, where collision-induced dissociation (CID) experiments are carried out. The collision energy can be adjusted by changing the offset between Q_0 and Q_2 and the zero point of the kinetic energy scale as well as the width of the kinetic energy distribution is determined by means of retarding-potential analysis.

A typical retarding field curve for the primary ion at m/z 153 (data taken for biphenylium ion $C_{12}H_9^+$, produced in the APCI source using p-hydroxybiphenyl $C_{12}H_{10}O$) is shown in Fig. 2.6. The collision energy scans using API-3000 are presented as a function of a nominal collision energy, for which zero value is set to the point of inflection of the curve, obtained by the derivative of the curve. An explanation of the use of nominal values of collision energy is the following. Due to the fact that the primary beam is very wide (the full width at half maximum (FWHM) is about 3 eV in the laboratory frame), collision energy can not be well-defined. In addition, when working with neutral gas in the reaction cell, the smallest pressure of gas inside the middle quadrupole compatible

with the detection of products is around 10^{-4} mbar. For this value of pressure the mean free path (the average distance that the molecule travels between collisions) of a benzene molecule is about (or smaller by about 20%) the length of the reaction cell, which speaks in favor of secondary collisions. Therefore the collision energy can not be defined under such conditions.

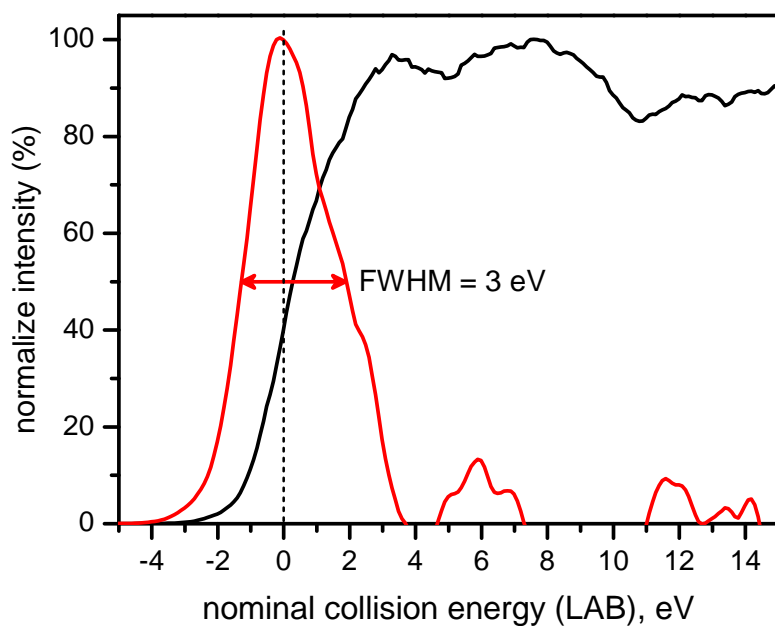


Figure 2.6: Retarding field analysis of the primary beam at m/z 153.

Chapter 3

Quantum Chemical Calculations

Quantum chemistry has been used in this work in parallel to mass spectrometry experiments in order to shed more light on the gas-phase behaviour of the species under study. In particular, the aim of our quantum chemical calculations was the characterization of a molecular system in terms of geometries, relative energies and electronic states of reactants, intermediates, transition structures and products formed during a reaction. The findings relative to the geometries of ground and transition states already tells us an important information about the reaction mechanisms, but the determination of the relative energies allows a more quantitative description of the thermochemistry of a reaction and the location of reaction barriers.

3.1 Introduction

The presence of several nuclei in polyatomic molecules makes quantum chemical calculations harder than for simple diatomic molecules. Besides, the electronic wave function of a diatomic molecule is a function of only one parameter, the internuclear distance. For a polyatomic molecule, the electronic wave function depends on several parameters, such as bond distances, bond angles and dihedral angles of rotation about single bonds. Therefore, the calculation of the electronic wave function for a range of each of these parameters is needed. To minimize the electronic energy the values of equilibrium bond distances and angles should be found. There are four main approaches to the theoretical determination of molecular properties: *ab initio* methods, semiempirical methods (SE), the density functional methods and molecular-mechanic methods. The method which will be used in this thesis is density functional theory (DFT). DFT has been shown to provide

good results at reasonable computational budgets when applied to molecular systems such as the ones discussed in this thesis. In the following a brief introduction to DFT will be given.

3.2 Density functional theory

Density functional calculations are, like *ab initio* and SE calculations, based on the Schrodinger equation. However, unlike the other two methods, DFT does not calculate a wavefunction, but calculates the molecular electron probability density ρ and calculates the molecular electronic energy from ρ . The idea of calculating atomic and molecular properties from the electron density arose from independent calculations on an ideal electron gas made by Enrico Fermi and P.A.M. Dirac in the 1920s (well-known Fermi-Dirac statistics [58]. In Ref. [59] atoms were modelled as systems located in a homogeneous electron gas having positive nucleus potential. This modelling (later called Thomas-Fermi model [60] had very good results only for atoms and not for molecules.

The Born-Oppenheimer approximation [61] is the first assumption made in DFT, as well as in any other quantum chemistry problem with more than two bodies. This approximation assumes that the nuclei are infinitely heavier than the electrons. In this way the motions of the nuclei can be easily separated from that of the electrons, and the electronic problem for a given set of stationary nuclei can be solved. In DFT calculations the properties of a molecule in a ground electronic state are determined by the ground state electron density function $\rho_0(x, y, z)$ (the first Hohenberg-Kohn theorem came out in 1964 [62], proved in Levine [63]). So, if we know $\rho_0(x, y, z)$, in principle we can calculate any ground state property, notably the energy, E_0 and

$$\rho_0(x, y, z) \rightarrow E_0 \quad (3.1)$$

this relationship means that E_0 is a *functional* of $\rho_0(x, y, z)$. Then this theorem says that any ground state property of a molecule is a functional of the ground state electron density function, e.g. for the energy

$$E_0 = F[\rho_0] = E[\rho_0] \quad (3.2)$$

The ground state electronic energy of a molecule can be presented as

$$E_0 = T[\rho_0] + V_{Ne}[\rho_0] + V_{ee}[\rho_0], \quad (3.3)$$

where T is the kinetic energy of the electrons, V_{Ne} is the attractive potential energy between the nuclei and the electrons, V_{ee} is the electron-electron repulsion potential energy. The last term can be represented in two parts: one classical Coulomb potential term and one nonclassical term. Thus determining the ground state of a system becomes a problem of finding the ρ that produces the minimum E . It was shown by Hohenberg and Kohn [62] that E will always be equal to or higher than the true ground state energy.

In the original DFT formalism E is only dependent on ρ , which is a function of only the three spatial coordinates x, y, z , while the wavefunction is a function of $4N$ coordinates (three spatial and one spin coordinate), where N is the number of electrons. Thus ρ significantly reduces the number of variables. However, there are difficulties in finding an accurate functional T , which would facilitate the direct minimization of the ground-state energy with respect to the electron density (see Ref. [64] for review) and this leads to unacceptably low accuracies. A significant improvement was obtained with the introduction by Kohn and Sham of the idea of a reference system of noninteracting electrons [65] (also known as KS orbitals). They represented E as two parts: one part that is based on noninteracting electrons and another part which is a correction for the electron interaction. Now equation 4.2 can be rewritten as

$$E_0 = T_r[\rho_0] + V_{Ne}[\rho_0] + J[\rho_0] + E_{xc}[\rho_0], \quad (3.4)$$

where T_r is the kinetic energy of noninteracting electrons, J is the classical Coulomb potential energy, E_{xc} is the exchange correlation energy, i.e. due to interacting electrons. The E_{xc} can be represented as the sum of the kinetic energy deviation from the reference system and the electron-electron repulsion energy deviation from the classical system:

$$E_{xc}[\rho_0] \equiv \Delta T[\rho_0] + \Delta V_{ee}[\rho_0], \quad (3.5)$$

where $\Delta V_{ee}[\rho_0]$ is the potential correlation energy and the exchange energy and $\Delta T[\rho_0]$ represents the kinetic correlation energy of the electrons, e.g. the deviation of the real kinetic energy from that of the reference system:

$$\Delta T[\rho_0] \equiv T[\rho_0] - T_r[\rho_0]. \quad (3.6)$$

The electronic kinetic energy of the noninteracting electrons $T_r[\rho_0]$ (reference system) is determined from the KS orbitals ψ_i^{KS} as

$$T_r[\rho_0] = \sum_{i=1}^N \left\langle \psi_i^{KS}(1) \left| -\frac{1}{2} \nabla_1^2 \right| \psi_i^{KS}(1) \right\rangle. \quad (3.7)$$

It is worth noting that because KS theory uses orbitals, the number of variables will increase from 3 to $3N$, but for the whole method the complexity is still far less than for many particle wavefunction models.

So now the exchange correlation energy in equation 3.4 can be rewritten as

$$E_{xc}[\rho_0] \equiv \Delta T[\rho_0] + \Delta V_{ee}[\rho_0] = T[\rho_0] - T_r[\rho_0] + V_{ee}[\rho_0] - J[\rho_0], \quad (3.8)$$

By defining it in this way, E_{xc} becomes the only term which can not be computed exactly in the expression for E , and the task of KS theory is to find an expression for it. There are different approaches, and B3LYP is the one which will be used in the thesis. B3LYP is the most popular hybrid functional at present and also the most popular DFT functional. It is based on an exchange-energy functional developed by Becke in 1993 (called Becke 3 parameter hybrid functional for the exchange energy [66]) and modified by Stephens et al. in 1994 [67] by introduction of the LYP 1988 correlation-energy functional (Lee, Yang and Parr functional [68]). The expression for this exchange-correlation functional will be

$$E_{xc}^{B3LYP} = (1 - a_0 - a_x) E_x^{LSDA} + a_0 E_x^{HF} + a_x E_x^{B88} + (1 - a_c) E_c^{VWN} + a_c E_c^{LYP}, \quad (3.9)$$

where the E_x^{LSDA} is the exchange energy, expressed through the Local Spin Density Approximation (LSDA), which treats the electron density locally as a uniform electron gas with different densities for spin up and spin down electrons; the E_x^{HF} is the KS-orbital-based exchange energy functional, given by the wavefunction based Hartree-Fock theory; E_x^{B88} is the Becke 88 gradient correction to the LSDA exchange energy and it is included because the electron gas is not uniform in reality; E_c^{LYP} is a similar gradient corrected functional for the correlation energy; E_c^{VWN} is the Vosko-Wilk-Nusair functional for the correlation energy [69], which forms part of the accurate functional for the homogeneous electron gas of the LSDA. The parameters a_0, a_x and a_c are those that give the best fit of the calculated energy to molecular atomization energies. The terms E_x (an exchange-energy functional) and E_c (a correlation-energy functional) are coming from the expression for the E_{xc} exchange-correlation energy functional $E_{xc} = E_x + E_c$ [70].

As mentioned earlier KS theory calls for the use of (molecular) orbitals. By turn a molecular orbital can be represented by a set of known functions, which are called basis set. When the basis set is complete, the molecular orbital can be accurately described. But this would require an infinite number of functions, which is of course impossible in real numerical calculations. Therefore a finite basis set has to be chosen large enough to give a reliable result and sufficiently small to require reasonable computational resources. It was mentioned by [71]: "There are probably as many basis sets defined for polyatomic calculations as there are quantum chemists". For this reason let us focus only on the basis set used in the calculations carried out in this thesis, namely the 6-31G* [74]. 6-31G* basis set describes the molecular orbitals using Gaussian functions. Gaussians contain an exponential function $e^{-\zeta r^2}$. By themselves Gaussians are not able to describe the qualitative features of molecular orbitals, because they tend to resemble the so called Slater functions, where the exponential is of the form $e^{-\zeta r}$. For instance, the first orbital of hydrogen atom is described by a Slater function. However, using linear combinations of multiple Gaussians gives a reasonable resemblance of Slater features. Unfortunately, it has the drawback of requiring more functions for describing the molecular orbital and its use does not increase the computational time because Gaussian functions provide more easily evaluated integrals. A further reduction in computational efforts can be obtained if the linear combination of Gaussian functions is fixed, which creates a so called contracted set of Gaussian functions. This contraction is advantageous to apply when treating the core electrons, as they do not contribute to the chemistry of the system. The first number of the 6-31G* basis set tells that the core orbitals are represented in terms of

six Gaussians. The next two numbers 3 and 1 refer to the valence electrons, these are the ones which participate in chemical bonds, and the shape of their molecular orbital may therefore deviate from the atomic orbital due to e.g. bonding. For this reason they are not described only by one function, but in this case by two functions. The first is a contraction of three Gaussians, the second consists of only one Gaussian. This arrangement, where the functions for the valence electrons are tripled, is referred to as a triple split valence basis set. It is worth noting that additional valence-shell splitting should lead to even greater flexibility.

6-31G* is also one of the simplest polarization basis sets, constructed from 6-31G by adding a set of *d*-type polarization functions written in terms of a single Gaussian for each heavy (non-hydrogen) atom. To give the lowest energies for representative molecules Gaussian exponents for polarization functions have been chosen. For instance, polarization of the *s* orbitals on hydrogen atoms is necessary for an accurate description of the bonding in many systems (particularly those in which hydrogen is a bridging atom).

Correlation-consistent basis sets cc-pVTZ and cc-pVQZ, developed by Dunning for the first and second row elements [72], were also used in our calculations. cc-p stands for “*correlation consistent-polarized*”, V speaks for valence-only basis sets, T stands for Triple (Q=Quadruple) Zeta. Such basis sets are formulated to yield the lowest possible CISD (A limited Configuration Interaction scheme in which only single and double excitations from occupied to unoccupied molecular orbitals are considered) ground-state atom energies [73]. They should be better suited than basis sets as 6-31G* to capture most of the correlation energy.

In this thesis DFT calculations have been done by the group of Prof. Glauco Tonachini (University of Turin) using the Gaussian09 program package [75] and by Prof. Paolo Tosi using Spartan software [76].

Chapter 4

Results and discussion

In this chapter results from GIB-MS and API-3000 experiments on $C_{10}H_7^+$, $C_{12}H_9^+$ and $C_{12}H_{10}O^+$ are presented and discussed in light of density functional theory theoretical calculations.

4.1 Reactivity of $C_{10}H_7^+$ ion with benzene

4.1.1 Introduction

Polycyclic aromatic hydrocarbons (PAHs) have been observed in quite different gaseous environments, such as combustion systems or the interstellar medium [86]. Thus understanding how these ubiquitous molecules are formed has become an increasingly important research topic in the last few years. While great progress has been made in the knowledge of synthetic mechanisms based on radical and neutral reactions [31], much less is known about ionic routes to the synthesis of PAHs. It is worth noting that ionic reactions are not restricted to “*obvious*” environments (gaseous discharges, plasmas, planetary ionospheres), but they also occur in unexpected situations, such as hydrocarbon flames [87, 88], or the exhaust of aircraft engines [89]. The formation of ionized naphthalene from the reaction of benzene radical cations with diacetylene was described and proposed almost 20 twenty years ago as a general model for the growth of PAHs by ion-molecule reactions [90]. More recently, the formation of benzene ions within ionized acetylene clusters has been reported [91]. In turn benzene ions can catalyze the polymerization of acetylene molecules and possibly their conversion into naphthalene-type ions [92]. An unexpected result from the Cassini flybys of Titan was the discovery of benzene at high altitude [93] and the presence of large mass (over 100 amu) positive and negative ions in significant

amounts in Titan’s ionosphere below 1200 km [20]. Among the possible structures of such large mass molecules fused-ring polycyclic aromatic hydrocarbon compounds (e.g. naphthalene and anthracene, but also nitrile aromatic polymers [21]) have been proposed, as well as fullerenes [22] and polyphenyls [23]. All such structures are compatible with Cassini detections and such heavy particles have been proposed to be the precursors to the haze particles which form the optically thick haze layer lower in Titan’s atmosphere [94]. In spite of several laboratory investigations, new experimental and theoretical data are still required to provide a quantitative comparison between the in situ observations of the Cassini orbiter and the proposed models. In the present section we report on new measurements about the reactivity of the naphthyl cation $C_{10}H_7^+$ with benzene.

4.1.2 Experimental results

The reaction of naphthyl cation $C_{10}H_7^+$ with benzene (both C_6H_6 and C_6D_6) was investigated by using both GIB-MS and API-3000 equipped with the APCI source. Naphthyl ions were formed by dissociative ionization of 1-chloronaphthalene in either EI or APCI sources. The reaction of naphthyl ions with benzene leads to the growth of larger hydro-

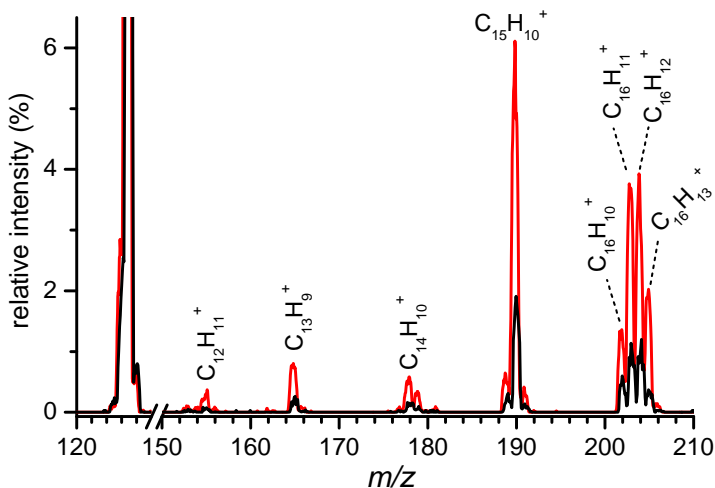


Figure 4.1: MS spectrum of ionic products from the reaction of mass-selected $C_{10}H_7^+$ ions with C_6H_6 recorded by GIB-MS at a collision energy $E_{CM} \sim 0.2$ eV in the center of mass frame and with $\sim 1.8 \times 10^{-4}$ mbar (black) and 8×10^{-4} mbar (red) of benzene in the reaction cell. The signal intensity of the parent ion (100%) is off-scale.

rohydrocarbon species via C–C bond forming reactions. In the case of benzene- h_6 , the occurrence of such reactions is evidenced by the detection of ions $C_{16}H_n^+$ with $n=13-10$

(m/z 202–205), $C_{15}H_n^+$ with $n=9-10$ (m/z 189 and 190), $C_{14}H_n^+$ with $n=9-11$ (m/z 177–179), $C_{13}H_9^+$ (m/z 165), and $C_{12}H_{11}^+$ (m/z 155) in the mass spectrum recorded at low collision energy using the GIB-MS equipped with the EI source (see typical mass spectra reported in Figure 4.1 at two different pressures of benzene- h_6 in the scattering cell).

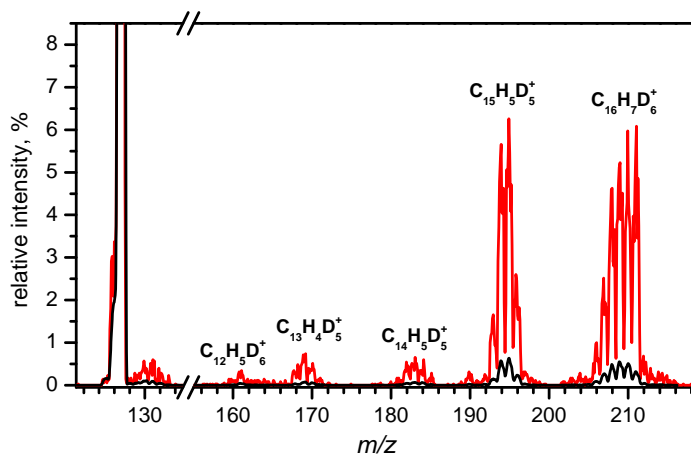
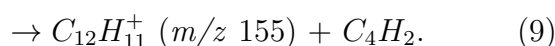
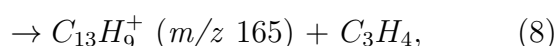
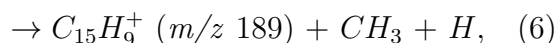
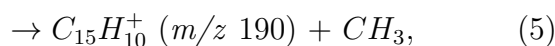
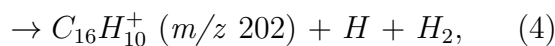
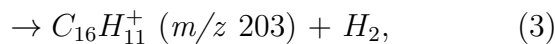
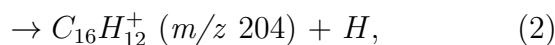
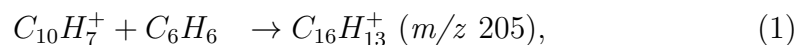


Figure 4.2: MS spectrum of ionic products from the reaction of mass-selected $C_{10}H_7^+$ ions with C_6H_6 recorded by GIB-MS at a collision energy $E_{CM} \sim 0.46$ eV in the center of mass frame and with $\sim 2 \times 10^{-4}$ mbar (black) and 8×10^{-4} mbar (red) of benzene- d_6 in the reaction cell. The signal intensity of the parent ion (100%) is off-scale.

In conjunction with the mass shifts observed upon using benzene- d_6 as reactant (see Fig. 4.2), the generation of such ions is attributed to the occurrence of the following reactions:



The product branching ratios at two different pressures are shown in columns (a) and (b) of Table 4.1. At low benzene pressures the formation of the $C_{16}H_{13}^+$ ion is indeed ob-

Table 4.1: Branching ratios for formation of the various product channels observed upon reaction of $C_{10}H_7^+$ with benzene- h_6 at the following conditions: (a) GIB-MS, benzene pressure 1.8×10^{-4} mbar, (b) GIB-MS, benzene pressure 8×10^{-4} mbar, (c) API-3000, benzene pressure 9.5×10^{-4} mbar.

m/z	Ion	Branching ratios, %		
		(a)	(b)	(c)
Others		0	0	0.6
153 e 155	$C_{12}H_n^+$ n=9, 11	2	3	0.1
165 e 166	$C_{13}H_n^+$ n=9, 10	4	5	0.2
177-181	$C_{14}H_n^+$ n=9-13	4	5	0.4
189-191	$C_{15}H_n^+$ n=9-10	38	34	5.5
202	$C_{16}H_{10}^+$	9	6	1
203	$C_{16}H_{11}^+$	19	20	7.2
204	$C_{16}H_{12}^+$	19	18	6.1
205	$C_{16}H_{13}^+$	5	9	78.3
Total		100	100	100

served experimentally though in a rather low relative yield. The latter is however increasing with the pressure (from 5% to 9%, corresponding to an increase of the pressure from 1.8×10^{-4} mbar to 8×10^{-4} mbar, see Table 4.1). This indicates that multiple collisions allow an efficient dissipation of the energy liberated upon association, thus providing stabilization of the initially excited addition complex, and formation of a long-lived species. The latter most likely has the structure of covalently bound protonated phenyl-naphthalene, formed via electrophilic addition of naphthyl cation to the benzene ring. As well as on specific pressures and collision energy conditions, the relative ionic yields of the various channels are found to be dependent on the ionization method used to generate the $C_{10}H_7^+$ primary ions. Values referring to the use of the API-3000 (with the APCI source) are reported in column (c) of Table 4.1, while a typical mass spectrum is shown in Figure 4.3.

The most striking difference between the ion yields measured by using two different methods for the generation of naphthyl cations (namely EI ionization in GIB-MS and APCI ionization in API-3000) is observed for the association product $C_{16}H_{13}^+$: in the case of EI

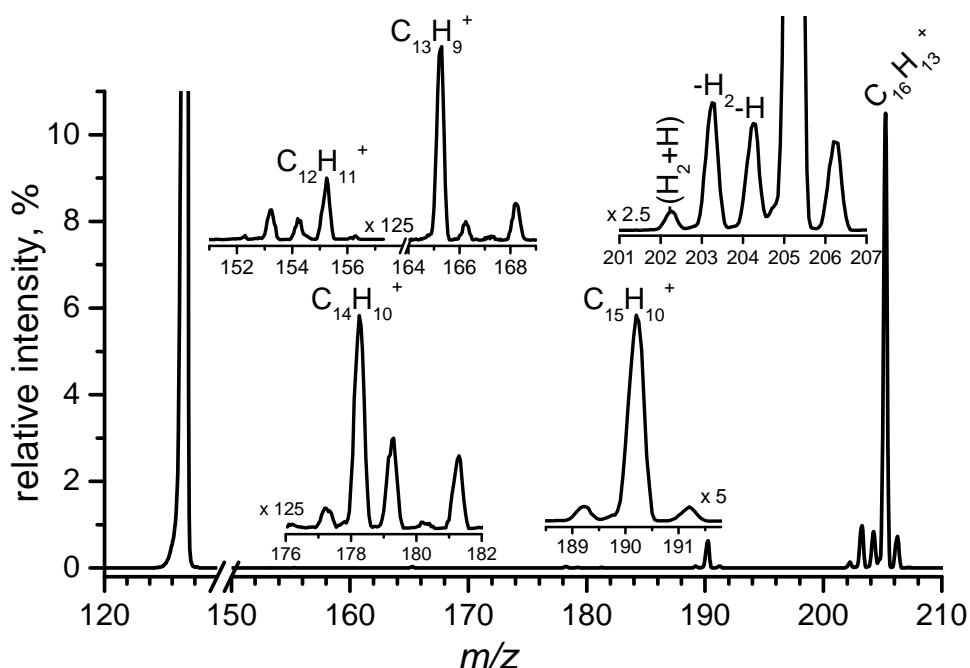


Figure 4.3: MS spectrum of ionic products from the reaction of mass-selected $C_{10}H_7^+$ ions with C_6H_6 recorded by API-3000 at a collision energy $E_{CM} \sim 1$ eV (CE 3.6 in the lab) in the center of mass frame and with $\sim 9.5 \times 10^{-4}$ mbar of benzene in the reaction cell. The signal intensity of the parent ion (100%) is off-scale.

generation (see Figure 4.1 and Table 4.1) the yield of $C_{16}H_{13}^+$ amounts to about 91% (at a pressure of benzene $\sim 8 \times 10^{-4}$ mbar), the main product being $C_{15}H_{10}^+$ produced according to reaction (5) above. Conversely, for APCI generation (see Figure (4.3) and Table 4.1 the association product predominates with a yield of about 62% (at a similar value of the benzene pressure $\sim 10^{-3}$ mbar). The difference is attributed to the internal excitation of the $C_{10}H_7^+$ reacting ion, which is expected to reduce the lifetime of the intermediate complex and the probability for its stabilization into a long-lived species. The EI source of the GIB-MS operates at low pressure and therefore collisional cooling of the nascent ions is ineffective. On the contrary, $C_{10}H_7^+$ ions produced in the APCI source can dissipate the excess of internal energy by collisions with N_2 at atmospheric pressure prior to react with benzene.

The ratio I_P/I_0 as a function of the benzene density for reactions (2) and (5) is shown in Figures 4.4. Data have been collected at the lower collision energy achievable for the present system in GIB-MS about 0.2 ± 0.05 eV in the center of mass frame. We observe a linear dependence up to a density value of about 5×10^{12} molecules cm^{-3} (corresponding

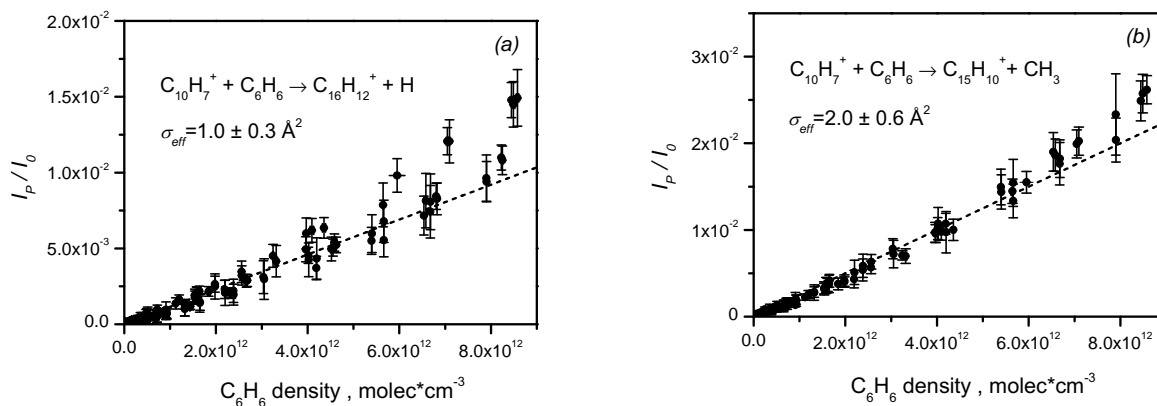


Figure 4.4: Density dependences of: (a) $C_{16}H_{12}^+$ and (b) $C_{15}H_{10}^+$ products after the reaction of $C_{10}H_7^+$ with C_6H_6 at a collision energy of about 0.2–0.3 eV in the center of mass frame. Dashed lines are linear fits of the data.

to a benzene pressure of about 2×10^{-4} mbar). By fitting the data we estimate the absolute values of the reactive cross section for channels (2) and (5) to be $1.0 \pm 0.3 \text{ \AA}^2$ and $2.0 \pm 0.6 \text{ \AA}^2$ respectively. The positive deviation from linearity observed at higher benzene densities can be due to several factors. In particular, multiple collisions can cool internal degrees of freedom of the ionic reactants and/or of the intermediate complexes, and at the same time they can collisionally stabilize products. Considering that reactions (2) and (5) proceed via an intermediate complex, which forms more efficiently at higher pressures due to collisional stabilization. In addition, a multicollisional regime tends to thermalize the reactant kinetic energy.

Reactive cross sections for channels (1)–(8) have been measured as a function of the collision energy in the range 0.1–3 eV, by using GIB-MS, at a benzene pressure of $\sim 8 \times 10^{-5}$ mbar to ensure single collision conditions. For the $C_{16}H_{12}^+$ and $C_{15}H_{10}^+$ products, absolute values of the cross section have been also measured at one specific energy. Cross sections at the other collision energies and for the other channels have been rescaled accordingly, by using the relative intensities of products. In this way absolute cross sections as a function of collision energy were derived and shown in Figure 4.5.

A common trend is the negative energy dependence of the cross sections, indicating barrierless exothermic processes, hence possible energy barriers should be lower than the total energy presumably available to the reactants. The cross section for reaction (1) (open squares in Figure 4.5(a)) shows the steepest decrease as the collision energy increases, which fits with a $E_{CM}^{-1.3}$ dependence (shown by the blue line in Figure 4.5).

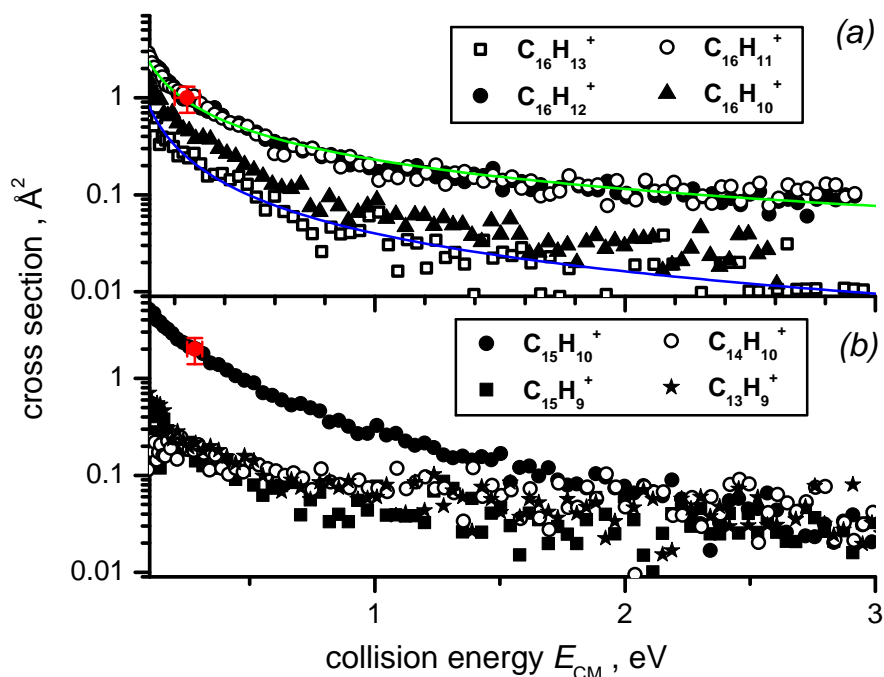


Figure 4.5: Cross sections as a function of the collision energy for the reaction of $C_{10}H_7^+$ with C_6H_6 leading to the following products: (a) $C_{16}H_n^+$ with $n=13-10$; (b) $C_{15}H_{10}^+$, $C_{15}H_9^+$, $C_{14}H_{10}^+$ and $C_{13}H_9^+$. Red points corresponds to the absolute values of the cross sections for channels (2) and (5), directly obtained from analysis of data shown in Fig. 4.4. Lines in (a) are guide for the eye indicating a dependence E_{CM}^{-1} (green) and $E_{CM}^{-1.3}$ (blue).

Several other channels leading to the loss of neutral fragments (i.e., H , H_2 , CH_3 , etc...) can compete with this reaction, thereby explaining the low yield of reaction (1) when carried out at low benzene pressure. The similar energy dependences of all the other channels (2)–(8) suggest that these reactions proceed via a complex-mediated mechanism, i.e., by formation and subsequent fragmentation of the association product $C_{10}H_7 \cdot C_6H_6^+$, with complex formation probability and lifetime strongly suppressed by an increase in the collision energy. We note in passing that the absolute value of the cross section for formation of the benzene addition product from naphthylum ion is smaller than the similar channel leading to $C_{12}H_{11}^+$ from phenylum ion, the latter having a cross section of $1.9 \pm 0.5 \text{ \AA}^2$ at 0.23 eV [85]. This difference is further demonstrated in Figure 4.6 where the MS spectra of products for the reactions of $C_{10}H_7^+$ and $C_6H_5^+$ ions with benzene are shown. Spectra have been taken using the API-3000 and care has been taken in ensuring the same experimental conditions in terms of collision energy, benzene pressure and source parameters relevant for the generation of $C_6H_5^+$ and $C_{10}H_7^+$ ions. The relative yield of

$C_{12}H_{11}^+$ from phenyl cations is about a factor two bigger than $C_{16}H_{13}^+$ from naphthyl cations.

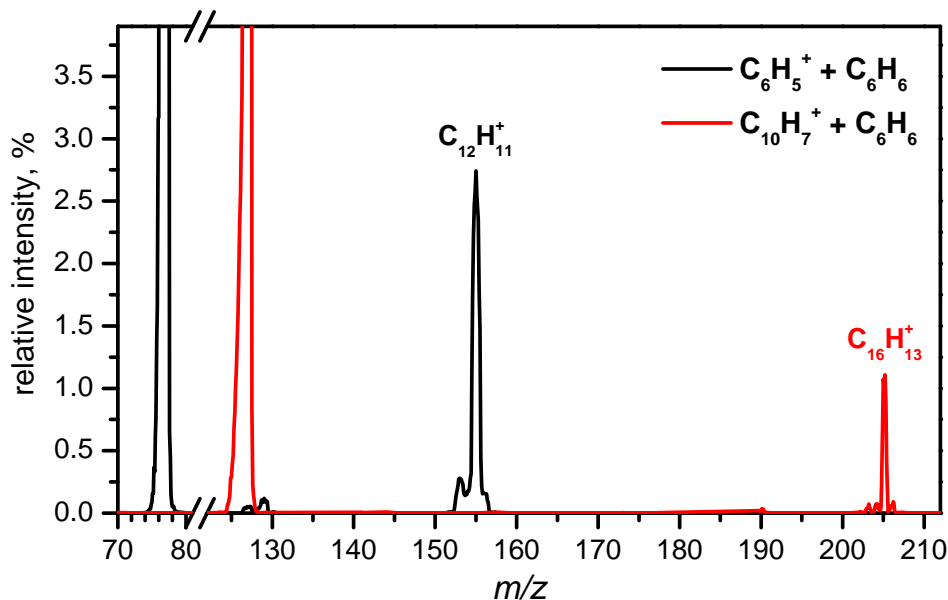


Figure 4.6: MS spectra of products from the reactions of $C_6H_5^+$ (in black) and $C_{10}H_7^+$ (in red) with benzene, recorded by API-3000 at an E_{CM} of ~ 1 eV and benzene pressure $\sim 10^{-4}$ mbar. Ions $C_6H_5^+$ and $C_{10}H_7^+$ (relative intensities 100%, out of scale) have been generated in the APCI source from chlorobenzene and 1-chloronaphthalene precursors respectively.

To shed more light on the reaction mechanism and on the structure of the adduct complex in the reaction of naphthyl cations with benzene we performed collision induced dissociation experiments on the cation $C_{16}H_{13}^+$ (m/z 205) by using N_2 as fragmentation gas. Primary ions at m/z 205 are produced in the APCI source by infusion of a solution of commercial phenylnaphthalene in methanol (0.1 mol/liter). The resulting MS/MS spectrum (reported in Figure 4.7) shows a fragmentation pattern in which the most intense ionic fragments occur at m/z 204 (loss of H), 203 (loss of H_2), 202 (loss of $H + H_2$) and 190 (loss of CH_3). Thus collision induced dissociation of $C_{16}H_{13}^+$ (having the structure of protonated phenylnaphthalene) affords fragments having the same masses of the ions produced in the reaction of $C_{10}H_7^+$ with benzene (compare MS spectra and peak positions in Figures 4.3 and 4.7). Other fragments are detected, although with smaller intensities at m/z 178 (formal loss of C_2H_3), 165 (formal loss of C_3H_4), 149 and 145 plus m/z 77 (in very low yield, formal loss of $C_{10}H_8$). It is worth noting that such fragments are detectable only at high collision energies (i.e. above 20 eV, nominal in the lab).

The MS/MS experiment supports the idea that reaction of naphthyl cation with ben-

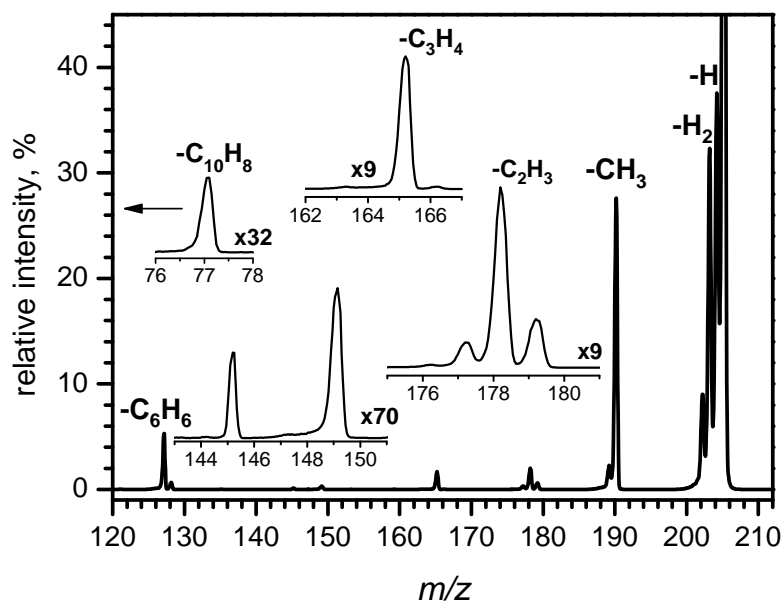


Figure 4.7: MS/MS spectrum of the m/z 205 ion generated by infusion of phenylnaphthalene in the APCI source, using N_2 as CAD gas at a pressure $\sim 10^{-3}$ mbar and a nominal collision energy of 28 eV in the LAB.

zene proceeds via a long lived intermediate complex, for which we can conjecture the structure of protonated phenylnaphthalene. When the internal energy content is high enough, the complex can dissociate along several channels, the principal ones being the loss of light fragments (H , H_2 , methyl).

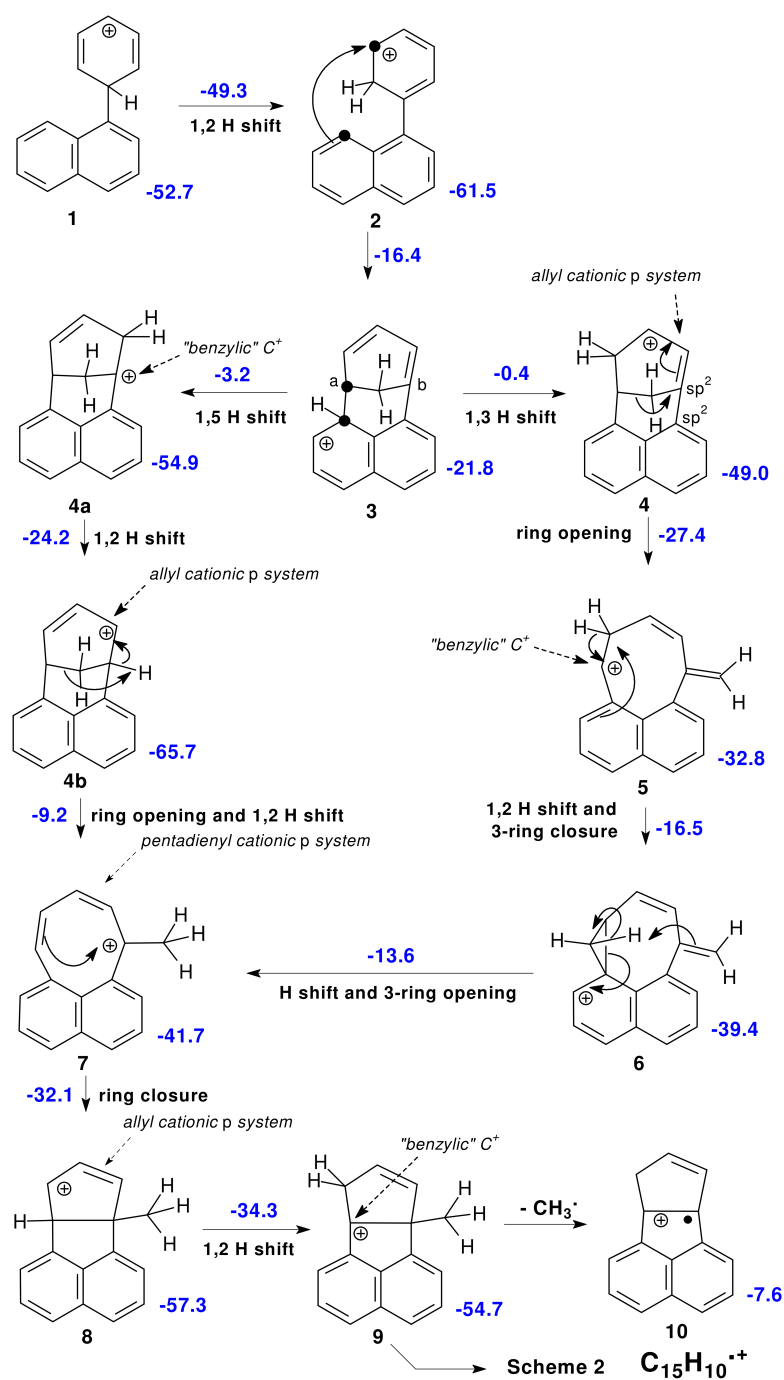
The reactivity of naphthylum ions with benzene molecules is investigated in previous radiolytic studies carried out using both gaseous benzene (at pressures in the range 7–80 mbar, i.e., much higher than those used in present experiments) and liquid benzene [95, 96]. The main observed products, after neutralization via proton transfer with the substrate or the reactor walls, are 1- and 2- phenylnaphthalenes as well as fluoranthene $C_{16}H_{10}$, observed only in one case and in rather low yield [95]. We underline the fact that a quantitative comparison between our and previous experiments is not possible due to the different pressure regimes used (single or close to single collision in our case and strongly multi-collisional regime in Ref. [95, 96]). However we note that C–C coupling reactions, having small reactive cross sections in our low-pressure experiments, occur with rather high overall absolute yields (up to 46%) at elevated benzene pressures [96]. With respect to the atmosphere of Titan, having low temperatures and a surface pressure of about 1 bar, if viable mechanisms exist for the generation of benzene and naphthylum

ions, the C–C coupling reactions of smaller building blocks of the type studied in this section might represent viable paths for further growth of larger hydrocarbons.

4.1.3 Theoretical results and reaction mechanisms

One of the more prominent peaks in Figure 4.1 is relevant to the $C_{15}H_{10}^+$ radical cation, which can form upon methyl radical loss from $C_{16}H_{13}^+$ (reaction 5). Since its origin does not appear obvious, the purpose of this theoretical part of the study is to focus on the possible transformations leading to it. First, naphthylum can be generated with two accessible spin multiplicities, singlet and triplet [97]. Since they are separated by only 3 kcal mol⁻¹, in favour of the singlet [98] or in favour of the triplet (it was shown recently in [99]), they can be deemed accessible both, under present experimental conditions. However, upon exploration of the first reaction steps for the triplet, sizeable barriers have been assessed, that discouraged a full study. Therefore, the energies so defined are just reported in note for completeness [100], making reference, as regards structure identification, to the same numbers used for the singlet (see Scheme 4.8). The results obtained on the singlet hypersurface are presented in the following, discussing CBS ΔE_{ZPE} values, while geometries and energies can be found in the supplement material file [101]. The singlet pathways can be considered reasonably to be at the origin of the largest part of the observed products.

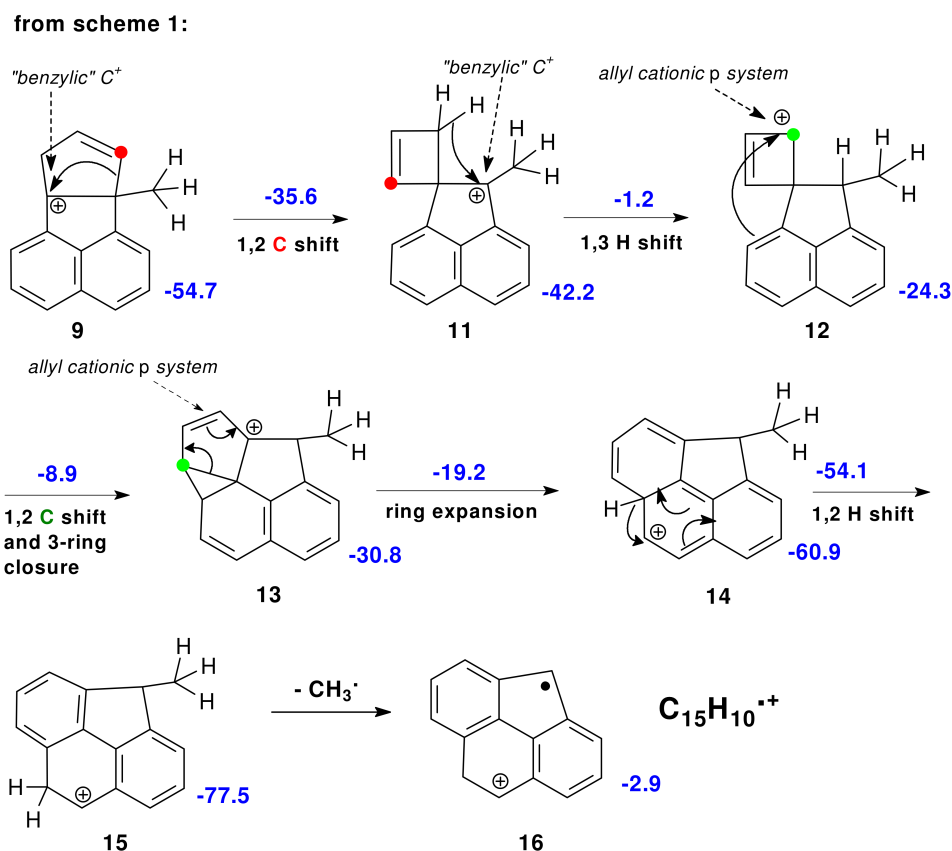
Naphthylum acts as an electrophile and adds to the π system of benzene, leading initially to the formation of an ionic adduct with an exothermicity of about 53 kcal mol⁻¹ (i.e., lying at -53 kcal mol⁻¹ with respect to the reagents, taken as our reference energy throughout). Starting from structure **1** several rearrangements have been explored, apt in principle to lead to a methyl radical loss. We have found that the only sequences of events suitable to get in the end a methyl loss include: **1** a ring closure leaving a methylenic group connecting two other carbons, C_a and C_b in Scheme c and 4.11 (which can be bridgeheads or not); **2** cleavage of one of the two bonds $C_a - C$ or $C - C_b$ in the bridge $C_a - CH_2 - C_b$, to get an exocyclic methylenic group; **3** a final H shift to generate the methyl group, which then dissociates. One or more H shifts can occur in between the above stages. Steps **2** and **3** may be concerted. Consequently, only the most promising pathways are displayed in Schemes 4.8–4.11 and their key passages are illustrated in the following. On the onset, after an easy 1,2 H transfer, the key step for the subsequent formation of a methyl group is the electrophilic addition **2–3**, whose barrier is at -16 kcal mol⁻¹ with respect to the reagents (see Scheme 4.8). It brings about the formation in **3** of



Scheme 4.8: Structures and energies of the most relevant stationary points on the reactive potential energy surface leading from $C_{10}H_7^+$ plus benzene to $C_{15}H_{10}^+$ (structure **10**) plus CH_3 . Hydrogen atoms are explicitly indicated when they are involved in shifts or gradual CH_3 formation. Energies are in kcal mol $^{-1}$.

a bicyclic subunit condensed with the rings formerly belonging to naphthylum (n-rings), located in turn at $-22 \text{ kcal mol}^{-1}$ with respect to the reagents. This subunit carries a methylenic group as a one-carbon bridge, indicated as $C_a - CH_2 - C_b$ in Schemes 4.8 and 4.11, which is the future nucleus for methyl group formation. This rearrangement has an energetic cost which can easily be sustained by the evolving system. Then, two alternative H transfers (**3-4** and **3-4a**) can restore the aromaticity of the leftmost n-ring. However the H shifts require overcoming sizable energy barriers, which bring the system energy close to the zero defined by the separate reactants. **3-4a** is slightly favoured, having a barrier at -3 kcal mol^{-1} with respect to the reagents. Then, the energy gain so attained is not negligible, since the energy of the system is now comparable in both cases to that of the initial adduct (**4a**: $-55 \text{ kcal mol}^{-1}$; **4**: $-49 \text{ kcal mol}^{-1}$). From **4**, ring opening and further H shifts produce first an 8-membered ring that carries a methyl substituent, **5**, $-33 \text{ kcal mol}^{-1}$, followed by two H shifts to get **7**, at $-42 \text{ kcal mol}^{-1}$. Both barriers relevant to these steps are well below our reference energy. The isomer **7** can be obtained also from **4a** and then **4b**, through an H shift and subsequent ring opening (with barriers at -24 and -9 kcal mol^{-1}). So, both pathways stemming from **3** finally converge on **7**. Then a final ring closure with formation of two condensed 5-membered rings leads from **7** to **8** (at $-57 \text{ kcal mol}^{-1}$). Another H shift and a final methyl radical loss from **9** (which is at $-55 \text{ kcal mol}^{-1}$) lead to the $C_{15}H_{10}^+$ product (**10**). The dissociation limit is at -8 kcal mol^{-1} with respect to the reagents. From **9**, an alternative pathway (described in Scheme 4.9) leads to an isomer of **10**. The first step is a 5-ring opening/4-ring closure (barrier at $-36 \text{ kcal mol}^{-1}$ with respect to the reagents) which forms the spiro intermediate **11**, at $-42 \text{ kcal mol}^{-1}$. Its evolution is energy demanding, yet with a barrier still below the reference. A difficult H shift (barrier at -1 kcal mol^{-1}) and a subsequent easier C shift (barrier at -9 kcal mol^{-1}) generate an intermediate in which the migrating C (highlighted with a green dot in Scheme 4.9) bridges onto two carbons of one n-ring (**13**, at $-31 \text{ kcal mol}^{-1}$). Then the 3-membered ring breaks and a ring expansion follows (barrier at $-19 \text{ kcal mol}^{-1}$), generating a structure resembling phenanthrene, **14**. It is quite stable, at $-61 \text{ kcal mol}^{-1}$. A further H shift allows to create a biphenyl-type structure, and the intermediate **15** is even more stable ($-77 \text{ kcal mol}^{-1}$). The dissociation of a methyl radical leaves the intermediate product **16**, of formula $C_{15}H_{10}^+$. This last step is very endoergic, yet the energy of the dissociation limit is still below the reference by 3 kcal mol^{-1} .

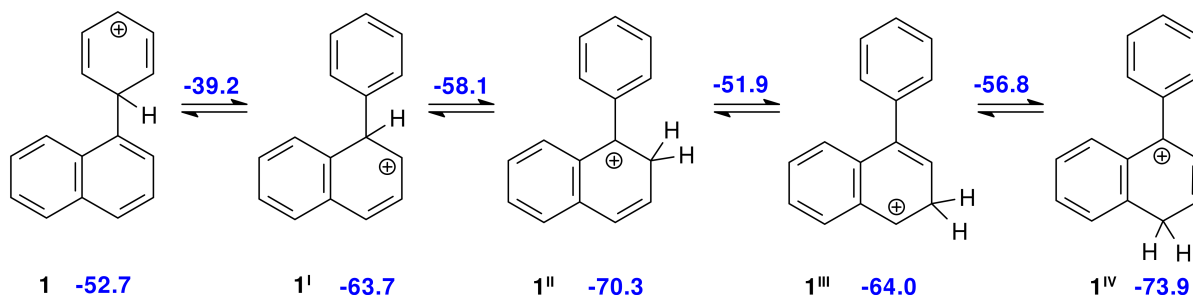
In conclusion, the channel through **3** and **4a** implies overcoming a slightly lower barrier than that through **3** and **4**. Then the step from **9** to **10** with methyl loss goes up to -8



Scheme 4.9: The alternative pathway leading to methyl loss from $C_{16}H_{13}^+$ (structure **9**) with formation of $C_{15}H_{10}^+$ in an isomeric structure with respect to **10** (described in Scheme 4.8). Hydrogen atoms are explicitly indicated when they are involved in shifts or gradual CH_3 formation. Carbon atoms involved in bond breaking/bond forming steps are highlighted with red and green dots. Energies are in kcal mol⁻¹.

kcal mol⁻¹, while that from **9** to **11** and **12** has to go up to -1 kcal mol⁻¹. All considered, the description of the $C_{16}H_{13}^+ \rightarrow C_{15}H_{10}^+$ evolutions offered above appears consistent with the height of the $C_{15}H_{10}^+$ peak. We have also explored the possibility of methyl loss involving a carbon that belongs to one n-ring. Also in this case we describe as an example only a channel presenting lower barriers for methyl loss. For this alternative process to proceed, the **1–3** sequence outlined above (see Scheme 4.8) should actually be preceded by preliminary hydrogen migrations to position 4 of the formerly naphthylum part (1^{IV} in Scheme 4.10), in order to form a methylenic group (in the initial adduct **1** the n-ring is bound to the phenyl part by its position 1). We note in passing that isomers $1^I - -1^{IV}$ having the “extra” hydrogen bound to a sp^3 carbon belonging to the “naphthalene” part of the adduct, actually have lower energies than **1** itself, the most stable one being structure

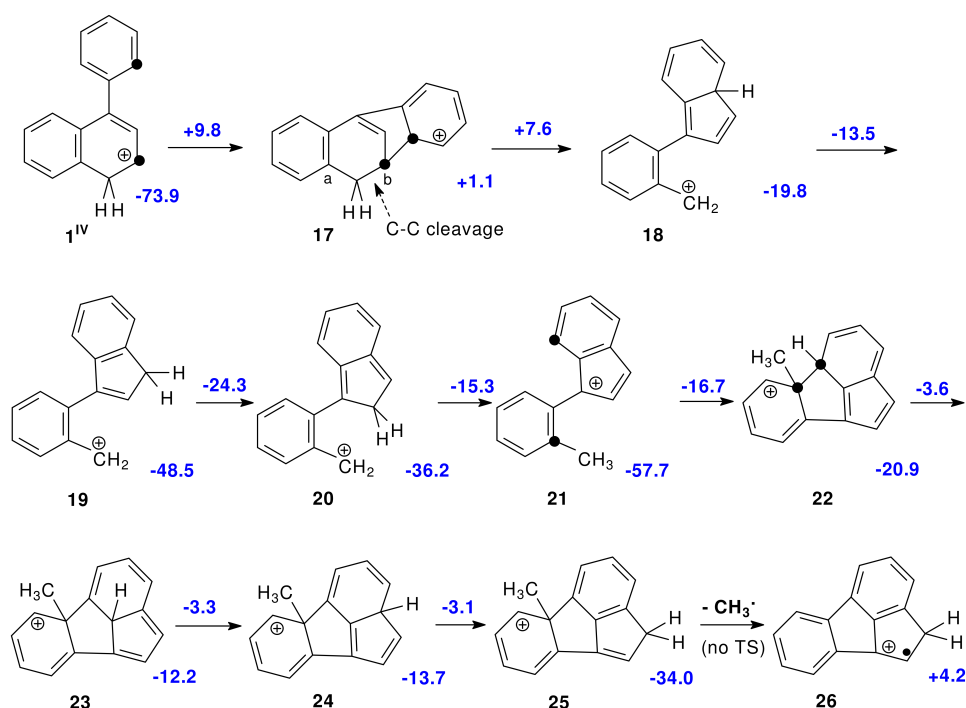
1^{IV} that lies ~ 21 kcal mol $^{-1}$ lower than structure **1**.



Scheme 4.10: Structures and energies of the hydrogen migrations along the rings of the $C_{16}H_{13}^+$ adduct. Shifting hydrogens are explicitly indicated. Energies are in kcal mol $^{-1}$.

The complete mechanism for methyl loss from the n-rings is represented in Scheme 4.11. After H migrations leading to 1^{IV} , the next step entails binding one ortho carbon of the phenyl part to the 3 position (which becomes C_b) in the rightmost n-ring (the C atoms involved in this step are highlighted by black dots in structures 1^{IV} and **17** of Scheme 4.11). The ring closure step brings the reacting system to an higher energy with respect to the reference level defined by the two reactants (structure **17**, at +1.1 kcal mol $^{-1}$). Then, a bond cleavage involving the CH_2 group would follow: two are possible, but only breaking of $CH_2 - C_b$ is relatively easy. After some H shifts the methyl group is formed. One ring closure and a few other H shifts and it can leave without attaining too high an energy (+4.2 kcal mol $^{-1}$ with respect to reagents). Methyl loss from **21–24** does not allow to form a biphenyl structure which can be attained only from **25**. In concluding the survey of the most viable channels it is worth pointing out that the CH_3 loss from phenyl (Schemes 4.8 and 4.9) is at any step below the reference level defined by reagents, and thus is a viable pathway for methyl loss in cold environments such as the interstellar medium or Titans ionosphere.

Regarding the formation of $C_{16}H_{12}^+$ and $C_{16}H_{11}^+$, we expect that the high exothermicity of reaction (1) leading to structure **1** favours further chemical rearrangements giving rise to H and H_2 losses, reactions (2)–(4), maybe as a consequence of self-condensation reactions resulting in fluoranthene-like structures, as put forward in Ref. [95]. However the theoretical investigation of these reactive channels is beyond the scope of the present section.



Scheme 4.11: The alternative pathway leading to methyl loss from the naphthylmethyl cation. Hydrogen atoms are explicitly indicated when they are involved in shifts or gradual CH_3 formation. Energies are in kcal mol^{-1} .

4.1.4 H/D scrambling

Further measurements are carried out in the API-3000 by using isotopically labelled C_6D_6 as neutral reagent, with the purpose of investigating any possible H/D atom scrambling during reactions (2)–(9) and of observing channels leading to back-fragmentation of the association product adduct into reactants. A typical mass spectrum of products from the reaction of $C_{10}H_7^+$ (produced in the APCI source) with C_6D_6 taken at a collision energy $E_{CM} \sim 0.5 - 1$ eV and benzene- d_6 pressure $\sim 10^{-3}$ mbar is shown in Figure 4.12. The mass spectrum is complicated by extensive H/D atom scrambling in some of the reaction products, similar to what previously observed in the phenyl cation/benzene system [85].

In ion-molecule reactions leading to arenium-like ions (e.g. protonated benzene, protonated naphthalene and protonated biphenyl [85, 102, 103]) H/D atom scrambling implies a reactive mechanism that proceeds via the formation of an intermediate complex, whose lifetime is long enough to allow a redistribution of the H and D atoms over the rings via 1,2-hydrogen shift, both intra and inter rings (i.e. the benzyl and naphthyl rings in the present case of $C_{16}H_{13}^+$ having the structure of protonated phenylnaphthalene). The

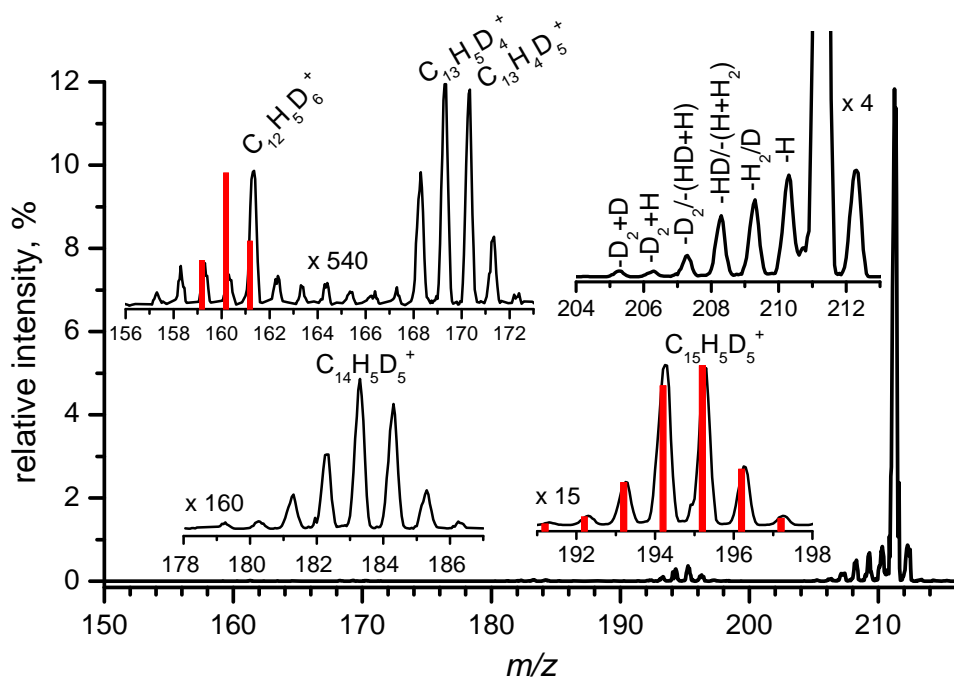


Figure 4.12: MS spectrum of ionic products from the reaction of mass-selected $C_{10}H_7^+$ ions with C_6D_6 recorded by API-3000 at a collision energy E_{CM} 1 eV in the center of mass frame (3.6 eV in the lab) and with 9.5×10^{-4} mbar of benzene- d_6 in the reaction cell. Red bars represent the calculated intensities corresponding to a complete randomization of position of H and D atoms in the ions $C_{15}(H, D)_{10}^+$ and $C_{12}(H, D)_{11}^+$ formed according to reactions (5) and (9) respectively.

reactive channel that is most easily analyzed in terms of H/D scrambling is reaction (5), leading to $C_{15}H_{10}^+$ at m/z 190 in the case of benzene- h_6 (in Figure 4.3 two peaks at m/z 189 and 191 are visible but with much smaller intensity compared to m/z 190: peak at m/z 189 corresponds to production of $C_{15}H_9^+$, with an intensity about 14 times lower than $C_{15}H_{10}^+$, while the contribution of $C_{15}H_{11}^+$ to the peak at m/z 191, when ^{13}C contribution is taken into account, is over a factor 90 smaller than $C_{15}H_{10}^+$). When naphthyl cations are reacted with benzene- d_6 a cluster of ions is observed in the m/z region 192–198, with the highest intensity at the mass of $C_{15}H_5D_5^+$ (m/z 195). The relative intensities of the peaks 193–196 within the cluster can be calculated assuming a *complete randomization* of the 7 H and 6 D atoms over both benzyl and naphthyl aromatic ring systems at the level of the intermediates $C_{16}H_7D_6^+$ indicated as **1** and **2** in Scheme 4.8 prior to production of $C_{15}(H, D)_{10}^+$ and, though in smaller amounts, of $C_{15}(H, D)_9^+$ and $C_{15}(H, D)_{11}^+$. From an energetic point of view H atoms can freely “walk” along both rings since barriers for 1,2 H shifts always lie well below the reactant energy. The peak intensities expected for

complete statistical scrambling can be calculated making allowance for the presence of ^{13}C at natural abundance in the C_6D_6 reacting partner [104], and taking into account the presence of channels leading $C_{15}(H, D)_9^+$ and $C_{15}(H, D)_{11}^+$, as well as $C_{15}(H, D)_{10}^+$. According to the results obtained in the fully hydrogenated case, the relative intensities of the three channels are in the ratio $C_{15}H_9^+ : C_{15}H_{10}^+ : C_{15}(H, D)_{11}^+ = 6.6:92.4:1.0$ and this same ratio is assumed also in the mixed isotope experiment.

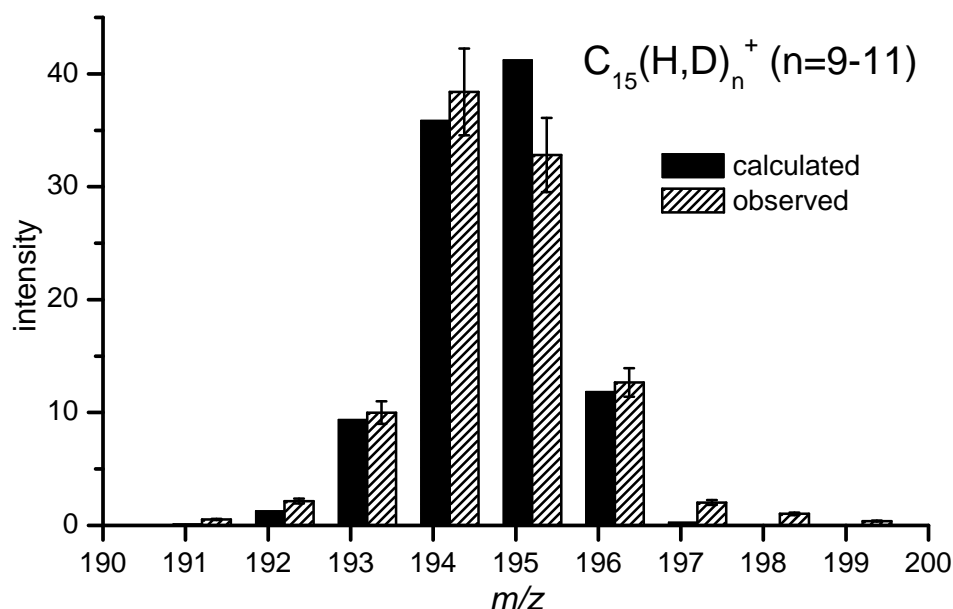


Figure 4.13: Experimental intensities of products from the reaction of $C_{10}H_7^+$ with C_6D_6 are compared with calculations assuming a complete randomization of the H and D atoms in the $C_{16}H_7D_6^+$ complex prior to dissociation leading mainly to $C(H, D)_3$ loss.

The calculated intensities are shown as hatched bars in Figure 4.13 and are compared with the experimental results (black bars) given in terms of areas of the experimental peaks in the mass range 191–199. Both data have been renormalized to give a total intensity of 100.0. Experimental intensities are in good, though non perfect agreement, with calculations from a model, suggesting that the mechanism for formation of $C_{15}(H, D)n^+$ (with $n=9-11$) ions involves a high degree of H/D randomization over both the naphthyl and phenyl rings.

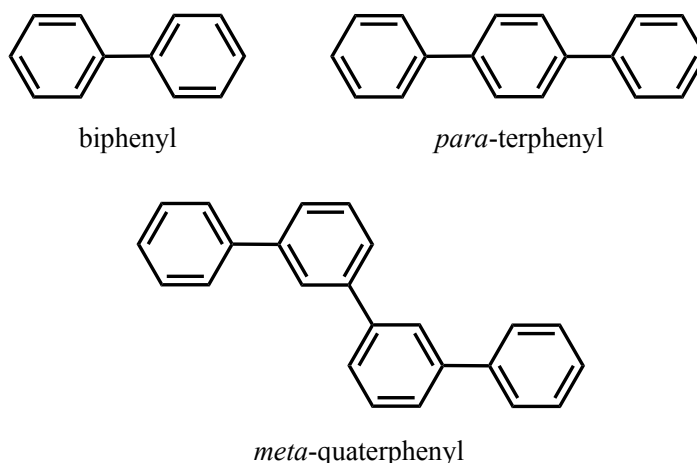
4.1.5 Conclusion

In this section we explored mechanisms for the molecular growth based on ion-molecule reactions, which can be relevant in ionized gases such as planetary ionospheres, plasmas, and combustion systems. The reaction of naphthyl cation $C_{10}H_7^+$ with benzene was investigated by using tandem mass spectrometers and reactive cross sections were measured as a function of the collision energy. We detected the association product $C_{16}H_{13}^+$ and various lighter cations corresponding to the loss of H , H_2 , and CH_3 . Experiments performed by using isotopic reagents indicate an almost statistical scrambling of H, D atoms among the different rings, thus suggesting that the reaction proceeds via a long-lived association product, presumably the covalently bound protonated phenylnaphthalene, from which lighter species are generated by elimination of neutral fragments. In particular the reaction channel $C_{10}H_7^+ + C_6H_6 \rightarrow C_{15}H_{10}^+ + CH_3$ was theoretically investigated by DFT calculations, and at least two exoergic mechanisms were found sketched in Schemes 4.8 and 4.9. This result is a clear example for the possibility of molecular growth via ion-molecule reactions, and may be relevant for explaining the detection of large PAHs in diverse environments, in those cases when a certain degree of molecular ionization is present.

4.2 Reactivity of $C_{12}H_9^+$ ion with benzene

4.2.1 Introduction

Not only polycyclic aromatic hydrocarbons can be present in Titan's atmosphere, but also polyphenyls [23] might be used to explain the formation of heavy hydrocarbons under the conditions of atmosphere of Titan. Polyphenyls are aromatic hydrocarbons with chemical and physical properties similar to PAHs (e.g. ionization potential and electron affinity). In general, polyphenyls refer to benzene rings bonded together with single C–C bonds between each ring (see Scheme 4.14).



Scheme 4.14: Structures of various polyphenyl molecules.

The simplest polyphenyl is biphenyl that consist of only two benzene rings. The reaction of biphenylium ion $C_{12}H_9^+$ with benzene was chosen to study in our laboratory as a consequence of the interest that such species have recently received as potential components of Titan's upper atmosphere. The cold temperatures and low pressures at the altitude of around 1000 km speak in favor of the formation of polyphenyls rather than PAHs. Thus polyphenyls can grow to the larger polymeric structures to form aerosols under such conditions [23].

4.2.2 Experimental results

The reactivity of biphenylium ion $C_{12}H_9^+$ with benzene was investigated by API-3000. Biphenylium ions $C_{12}H_9^+$ were produced in the APCI source using p-hydroxybiphenyl ($C_{12}H_{10}O$) as precursor via dissociation of the precursor ions ($C_{12}H_{10}OH^+$ generated

in the plasma corona discharge) induced by collisions with the nitrogen declustering gas.

A typical mass spectrum of the ionic products for the reaction of $C_{12}H_9^+$ with benzene is shown in Fig. 4.15(a). The spectrum was measured at a collision energy (in the center

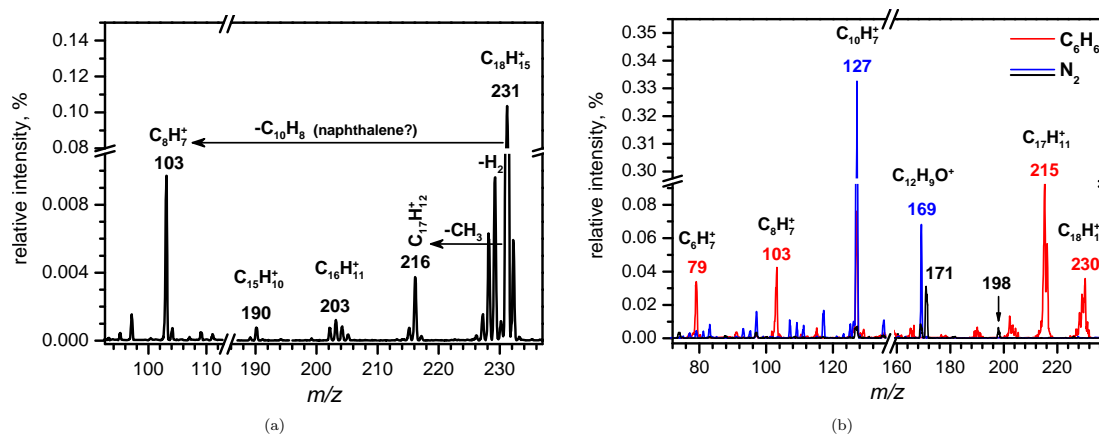
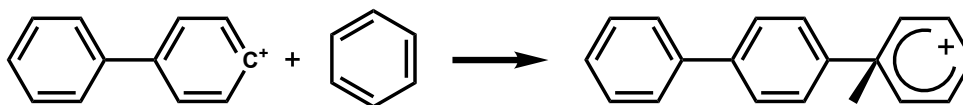


Figure 4.15: Mass spectrum of selected $C_{12}H_9^+$ ions reacting with $\sim 10^{-3}$ mbar of C_6H_6 (a) recorded by API-3000 at a collision energy $E_{CM} \sim 1$ eV in the CM frame. Mass spectra (b) of selected $C_{12}H_9^+$ ions colliding with benzene (red) and with N_2 (blue at a collision energy of 20 eV in the lab frame and black at a collision energy of 4 eV in the lab frame). The signal intensity of the parent ion (100%) is not shown.

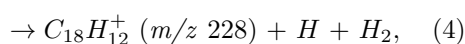
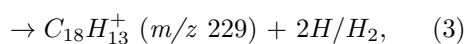
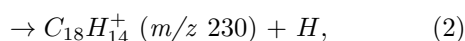
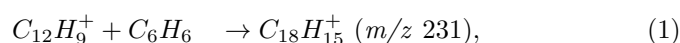
of mass frame) $E_{CM} \sim 1$ eV (corresponding to a nominal collision energy of 3.7 eV in the laboratory) and with a pressure of benzene inside the reaction quadrupole of about 10^{-3} mbar.

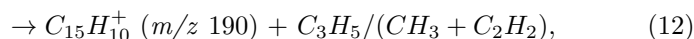
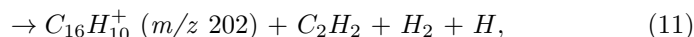
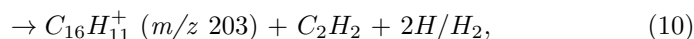
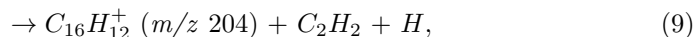
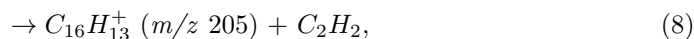
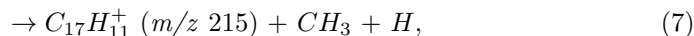
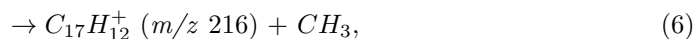
The main ionic product is observed at m/z 230 and a possible pathway might be the electrophilic addition of the aromatic neutral to the cation, followed by H migration to give the two different isomers of the terphenyl radical cation:



Scheme 4.16: Possible mechanism of the $C_{18}H_{15}^+$ ion formation.

The generation of various ions attributed to the occurrence of the following reactions:





To better understand fragmentation processes a collision induced dissociation experiment was performed using nitrogen in the reaction cell (the pressure of the nitrogen was about 2×10^{-3} mbar). The resulting mass spectrum is compared with the one observed with benzene (at a pressure of about 10^{-3} mbar) as reaction partner in Figure 4.15(b). A collision energy of 20 eV in the LAB was used in both benzene and nitrogen cases. The most intense peak at m/z 127 comes from the loss of C_2H_2 from the primary beam $C_{12}H_9^+$ (see spectrum with N_2 (blue line) in Fig. 4.15(b)). The presence of a peak at m/z 169 is due to the fragmentation of adducts that $C_{12}H_9^+$ forms with water (due to the presence of a certain degree of humidity in the nitrogen), which are indeed observed at m/z 171 (and 198 at low collision energies (see Fig. 4.15(b) the spectrum in black)). When working with benzene as a collision gas, in addition to products at high mass (e.g. m/z 215, 230) ions at m/z 79, 103 and 127 are observed. In particular, the ion at m/z 103 appears only when benzene is used as reagent and therefore it does not derive from collision induced dissociation of the primary ions, but can be regarded as a characteristic fragmentation of the product resulting from the addition of benzene to $C_{12}H_9^+$. This channel is found to be exothermic and will be discussed more in theoretical part.

The relative ionic yields of the different channels are reported in Table 4.2. The association product predominates with a yield of about 79%.

The dependence of product ion abundances on the nominal collision energy can provide some mechanistic insight in the reaction process. Products of exothermic or thermoneutral reactions generally have an onset at a similar energy to that of the parent ion and present a maximum at low collision energies, while endothermic channels require some excess energy to occur and thus peak at higher collision energies. The ion abundance curves as a function of the nominal collision energy in the LAB frame are shown in Figure 4.17(a)

Table 4.2: Branching ratios for formation of the various product channels observed upon reaction of $C_{12}H_9^+$ with benzene- h_6 at a benzene pressure of 10^{-3} mbar.

m/z	Ion	Branching ratios
103	$C_8H_7^+$	5.38 ± 1.5
104	$C_8H_8^+$	0.13 ± 1.5
189 – 191	$C_{12}H_n^+, n = 9 - 11$	0.67 ± 1.5
202 – 205	$C_{16}H_n^+, n = 10 - 13$	2.07 ± 1.5
215 – 217	$C_{17}H_n^+, n = 11 - 13$	2.4 ± 1.5
227	$C_{18}H_{11}^+$	1.05 ± 1.5
228	$C_{18}H_{12}^+$	3.52 ± 1.5
229	$C_{18}H_{13}^+$	6.94 ± 1.5
230	$C_{18}H_{14}^+$	0.46 ± 1.5
231	$C_{18}H_{15}^+$	78.85 ± 1.5
Total		100

for the ionic products $C_{18}H_{15}^+$ (adduct), $C_{18}H_{14}^+$ and $C_8H_7^+$.

The $C_{18}H_{15}^+$ product has the characteristic shape of an exothermic and barrierless formation of a covalently bound adduct via an intimate collision complex, while the other two products show markedly higher thresholds and should therefore be assigned to endothermic process. Due to the large spread in the kinetic energy distribution of the pri-

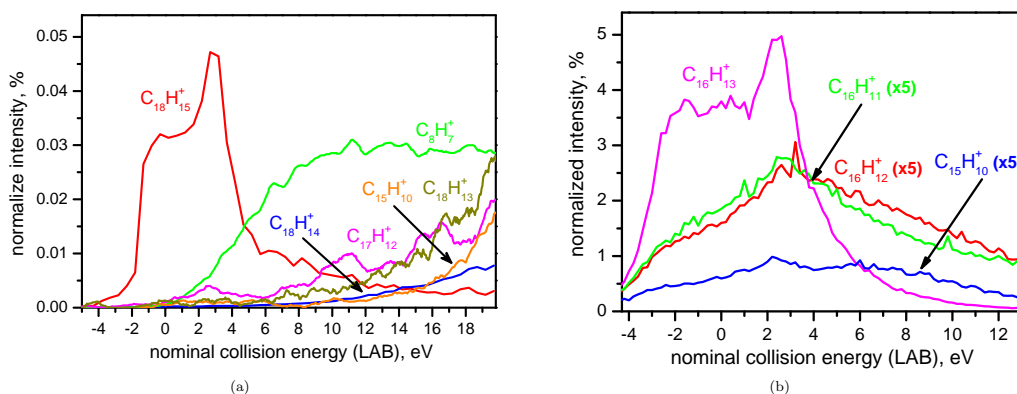


Figure 4.17: Normalized ion yields as a function of the collision energy (in the LAB frame) for the primary and product ions of the reaction of massselected $C_{12}H_9^+$ with C_6H_6 (a) and of the reaction of mass selected $C_{10}H_7^+$ with C_6H_6 (b).

mary ion, a quantitative measure of the appearance energy threshold for the endothermic products is beyond the capability of our experimental set-up, however we can qualitatively

observe that the $C_8H_7^+$ has the smallest threshold, while the loss of an H atom, H_2 , and CH_3 molecule from the adduct requires a substantially larger amount of translational energy.

To obtain further confirmation of the absence of any experimental artifacts, the data for the system $C_{10}H_7^+ + C_6H_6^+$, that was studied using GIB-MS as described in Section 4.1 and Ref. [55], were repeated using API-3000 and collision energy data are shown in Figure 4.17(b). In the case of naphthylum ion, reactivity studied with GIB-MS, the dependences of the collision channels for the loss of H , H_2 and CH_3 are exothermic. The data obtained with API-3000 and relative to adduct formation from $C_{10}H_7^+$ and from $C_{12}H_9^+$ have the same dependence on the nominal collision energy (see red line in Fig. 4.17(a) and magenta line in Fig. 4.17(b)). Channels of exothermic losses of H , H_2 and CH_3 have maximum at low collision energies for the case of naphthylum ion (see Fig. 4.17(a)). While in the case of biphenylum ion the only exothermic channel without a barrier is $C_{12}H_9^+ + C_6H_6 \rightarrow C_{18}H_{15}^+$. The other channels, like the one that leads to $C_8H_7^+ + C_{10}H_8$, seem to have an energy barrier and therefore might be interesting for the modelling of the growth of PAH in high energy environments such as flames, combustion, etc.. In particular, the channel leading to the formation of $C_8H_7^+$ is the most abundant after the adduct and it is the reactive channel showing the lowest energy threshold.

In Figure 4.18 comparison between reactivities of $C_6H_5^+$, $C_{10}H_7^+$ and $C_{12}H_9^+$ ions col

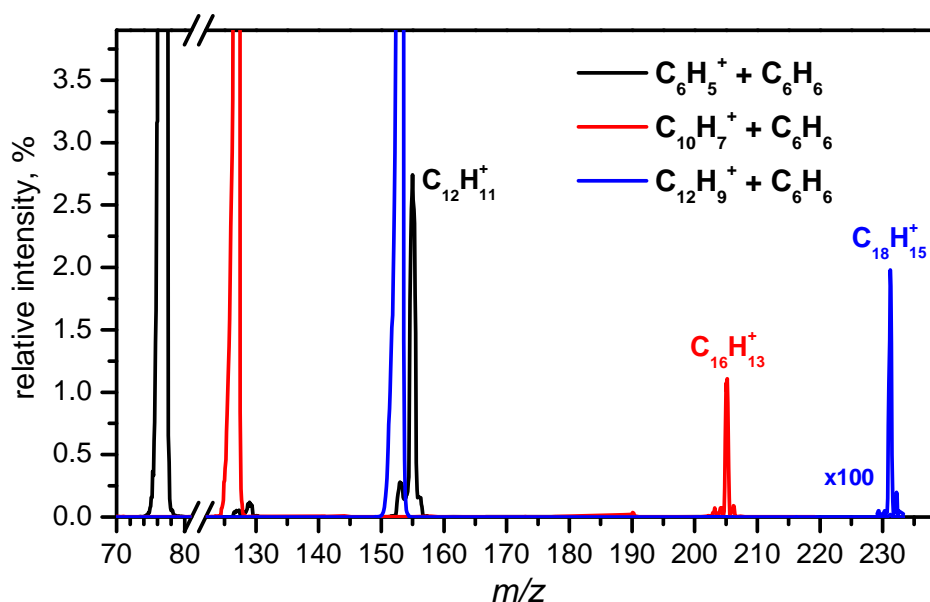
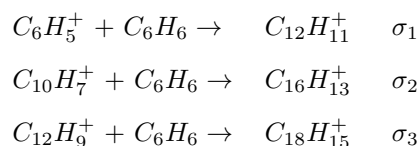


Figure 4.18: Comparison between reactivities of $C_6H_5^+$, $C_{10}H_7^+$ and $C_{12}H_9^+$ ion colliding with 10^{-4} mbar of benzene. The signal intensity of the parent ion (100%) is not shown.

liding with benzene is shown. The three MS spectra are renormalized so that the intensity fo the parent ion is 100% in each case. For the $C_{12}H_9^+$ plus benzene system the MS spectrum of product ions are also multiplied by a factor 100 for an easier comparison with the spectra of the other systems. A rough estimate of the reaction probability for the association of the $C_{12}H_9^+$ ions with benzene can be obtained as described in the following. Because the pressure of benzene in the scattering cell is the same in all cases, the ratios of the relative intensities of products (e.g. given by the integration over the mass peaks) can be assumed equal to the ratios of the corresponding reaction probabilities σ_i . In particular for the association reactions:



we can infer that:

$$\frac{\sigma_1}{\sigma_2} = \frac{I(C_{12}H_{11}^+)}{I(C_{16}H_{13}^+)} \approx 3 \quad (4.1)$$

and

$$\frac{\sigma_1}{\sigma_3} = \frac{I(C_{12}H_{11}^+)}{I(C_{18}H_{15}^+)} \approx 140 \quad (4.2)$$

Thus the highest reaction probabilities are observed for phenylium and naphthylum ions, while biphenylum ions are about a factor 100 less reactive against benzene.

4.2.3 H/D scrambling

Further measurements have been carried out by using isotopically labelled C_6D_6 as neutral reagent with the purpose of investigating any possible H/D atom scrambling and of observing channels leading to back-fragmentation of the association product into reactants. A typical mass spectrum of products from the reaction of $C_{12}H_9^+$ with C_6D_6 taken at a collision energy of 3.7 eV (in the lab) and with a benzene- d_6 pressure $\sim 10^{-3}$ mbar is shown in Figure 4.19(a). The mass spectrum is complicated by extensive H/D atom

scrambling in some of the reaction products, similar to what we have previously observed in the naphthylum/benzene system (see Section 4.1 and Ref. [55]).

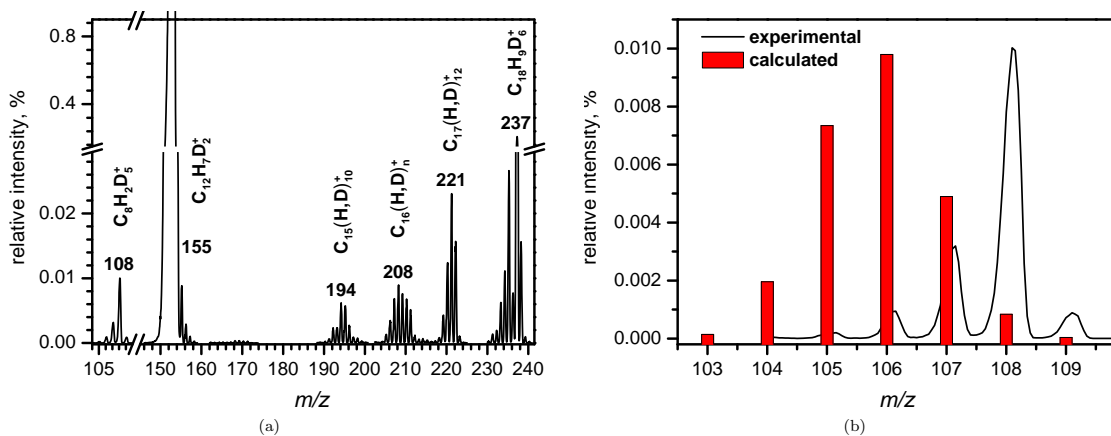


Figure 4.19: Mass spectrum of selected $C_{12}H_9^+$ ions reacting with $\sim 10^{-3}$ mbar of C_6D_6 recorded at a collision energy of 3.7 eV in the lab frame (a). The signal intensity of the parent ion (100%) is not shown. Comparison (b) between the experimental and calculated intensities in the mass region of $C_8(H,D)_7^+$ products. The calculated intensities correspond to a complete scrambling of the 9 H and 6 D atoms over the three rings prior to fragmentation.

So far we have focussed the attention only on the $C_8(H,D)_7^+$ product for which the scrambling is far from being statistical, as shown in Fig. 4.19(b), where the comparison between the experimental intensities and those calculated assuming a statistical redistribution of the H and D atoms over the three benzene rings prior to fragmentation is reported.

4.2.4 Theoretical results and reaction mechanisms

Here we will discuss the possible mechanisms for the formation of the ion $C_8H_7^+$. One of the more prominent peaks in Fig. 4.15(a) is relevant to the $C_8H_7^+$ cation observed at m/z 103, which can be formed upon fragmentation from $C_{18}H_{15}^+$, and implies the formation of a neutral counterpart of molecular formula $C_{10}H_8$. This peak is present only when $C_{12}H_9^+$ reacts with benzene. Moreover, the peak is more pronounced at high collision energy (>6 – 10 eV) and it almost disappears at collision energies smaller than 4 eV. Due to the fact that this peak may correspond to the formation of the smallest PAH, naphthalene, or other two-ring isomers the formation mechanism of the ion $C_8H_7^+$ bears a particular interest, and possible reaction channels are investigated.

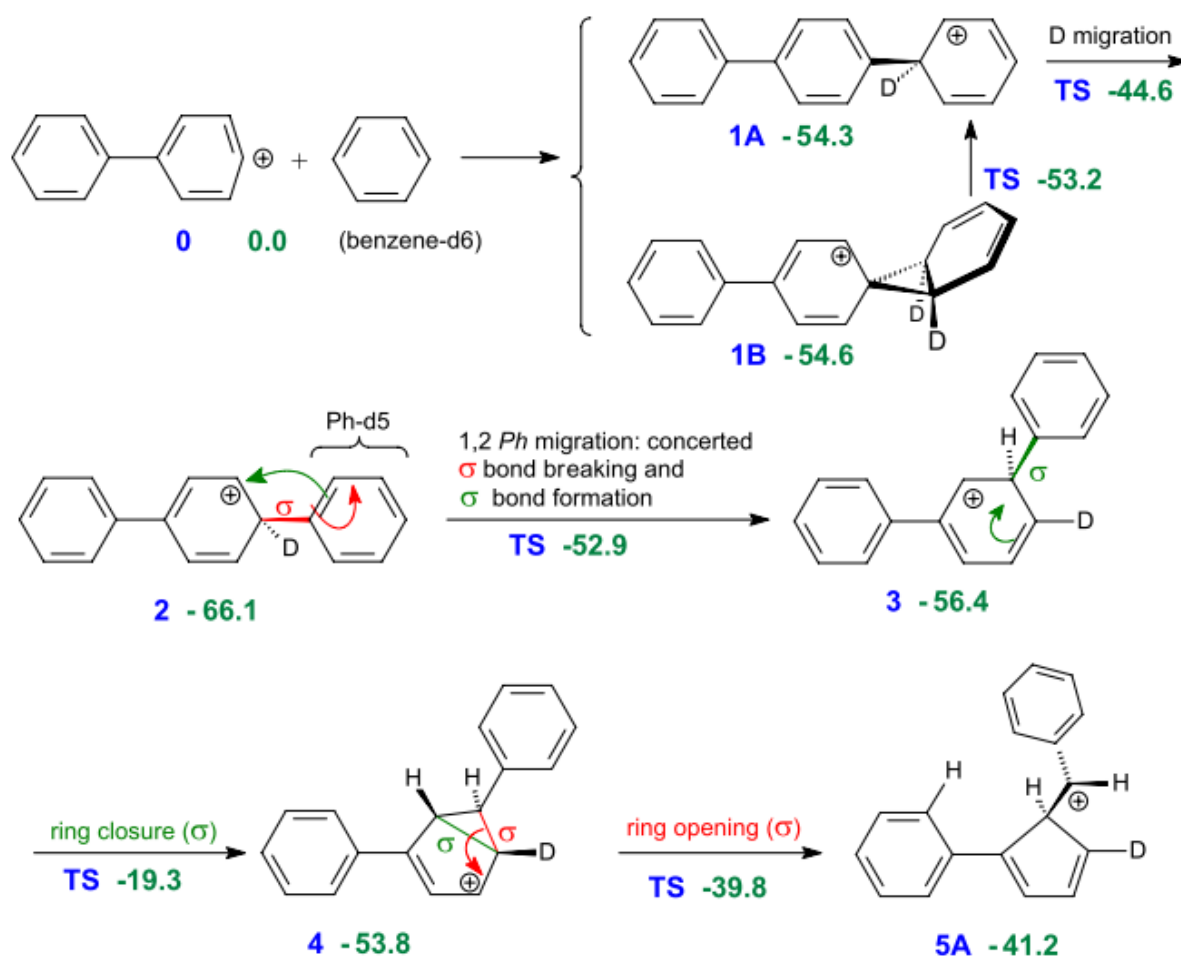
Biphenylum can be generated with two accessible spin multiplicities, singlet and

triplet. Since they are separated by only $1.9 \text{ kcal mol}^{-1}$, in favour of the singlet, they can be deemed accessible both under our experimental conditions. However, only results obtained on the singlet hypersurface are discussed here.

Several unimolecular transformations are explored, apt in principle to lead to a couple $C_8H_7^+/C_{10}H_8$. Among them, only the most promising pathway is displayed in Schemes 4.20–4.22, and the relevant steps are briefly commented in the following. Along this channel the system can evolve through some hydrogen shifts with ring closures and openings, and this allows in the end the formation of a naphthalene unit. An overall barrier above the reagents is present, and it has a moderate height, which is consistent with the experimental data on collisional energy dependences.

In Schemes 4.20–4.22 σ bond cleavages are indicated in red, σ bond formations in green. Biphenylium acts as an electrophile and adds to the π system of benzene, leading initially to the formation of either ionic adducts **1A** or **1B** (Scheme 4.20), depending on the formation of one or two σ bonds between the two moieties. The exoergicity (ΔE_{ZPE}) is in both cases $-54 \text{ kcal mol}^{-1}$ with respect to the reagents (labelled as **0** in Scheme 4.20), which is taken as a reference energy. An 1,2 H shift (or D shift, when working with deuterated benzene) from position **1'** to position **1** leads from **1A** to **2** down to $-66 \text{ kcal mol}^{-1}$. The relevant barrier is 10 kcal mol^{-1} high, i.e. below the reagents. The next rearrangement is a simple concerted 1,2 phenyl shift from position **4'** to **3'** of the original biphenylium. It entails a barrier of 13 kcal mol^{-1} and the isomer **3** is obtained. Both initial steps are well below the energy of the reagents. The energy of **3** is slightly below that of **1A**. Then, from **3**, the bridged intermediate **4** is obtained, in which the original 6-ring, though still present, splits into the two fused 5- and 3-rings. This is not an easy process, because it requires 37 kcal mol^{-1} , but since the system goes up to $-19 \text{ kcal mol}^{-1}$, it seems quite feasible. Then one bond belonging to the 3-ring cleaves and generates a central 5-ring and a C^+ -H bridge into the intermediate **5A**.

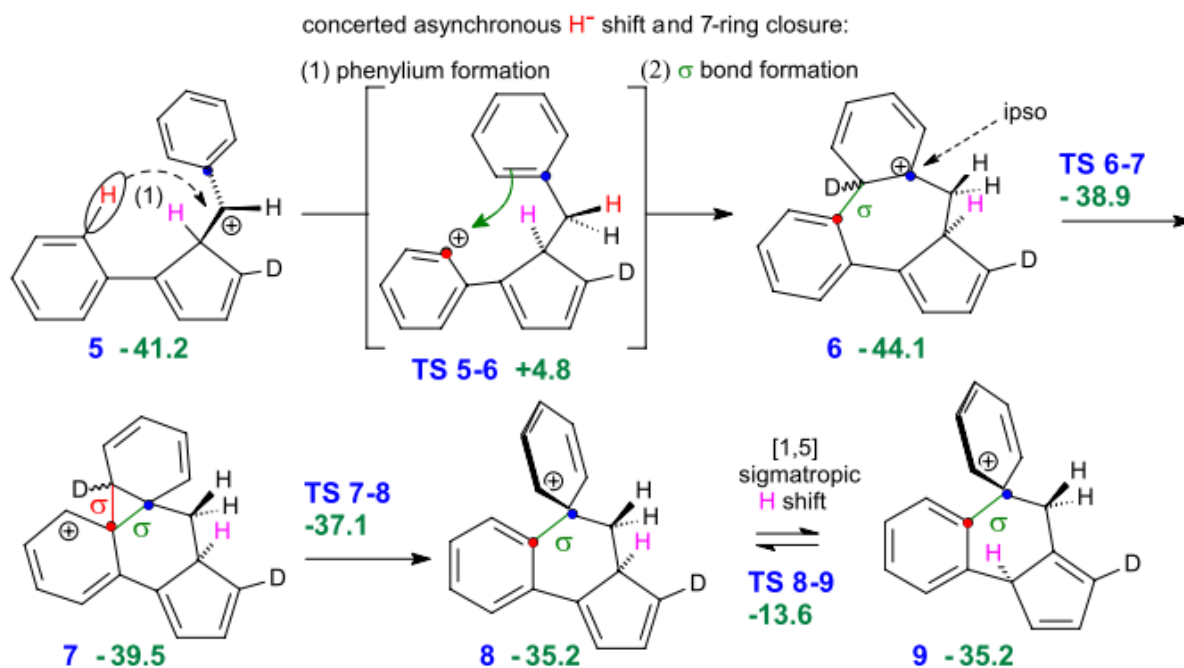
In Scheme 4.21 the phenyl group of structure **5** can transfer a hydride to the carbocationic center C^+ -H group. This occurs because a favorable geometric arrangement can be attained with consequent good overlap between one phenyl's ortho C–H bond and the empty π orbital on the C^+ . The H shift would create a “phenylium” substituent (phase (1) in Scheme 4.21, where a positive charge is localized on the carbon marked by a red dot). However, though this entity is recognizable on inspection of the transition structure (TS **5–6**), this positively charged carbon (marked by a red dot) concertedly attacks the upper phenyl group in the ortho position, indicated as a σ bond formation (2), which entails a



Scheme 4.20: Preliminary steps: adduct formation, phenyl migration, and formation of a central 5-membered cycle and methynic bridge. Energies are in kcal mol^{-1} .

7-ring closure. Consequently, a “phenylium”-carrying intermediate is not present along this pathway (as indicated by the brackets). The events (1) and (2) take place concertedly but asynchronously, in the sense that ring closure clearly follows the “H⁻” transfer, which is very nearly accomplished in a complete way in the TS. Along the reaction pathways discussed here, this step is the most demanding one. It corresponds to a barrier of 46 kcal mol^{-1} and the system goes up in energy, almost to 5 kcal mol^{-1} above the reactants. Subsequently, an easy two-step migration of the former phenylium carbon (red dot) to the ipso position of the upper phenyl group (blue dot), takes place. First, the formation of a 3-ring in the intermediate **7** occurs. Then, the former inter-ring connection is abandoned in favour of the new one, and the **8** spiro intermediate is obtained, in which the red-dot

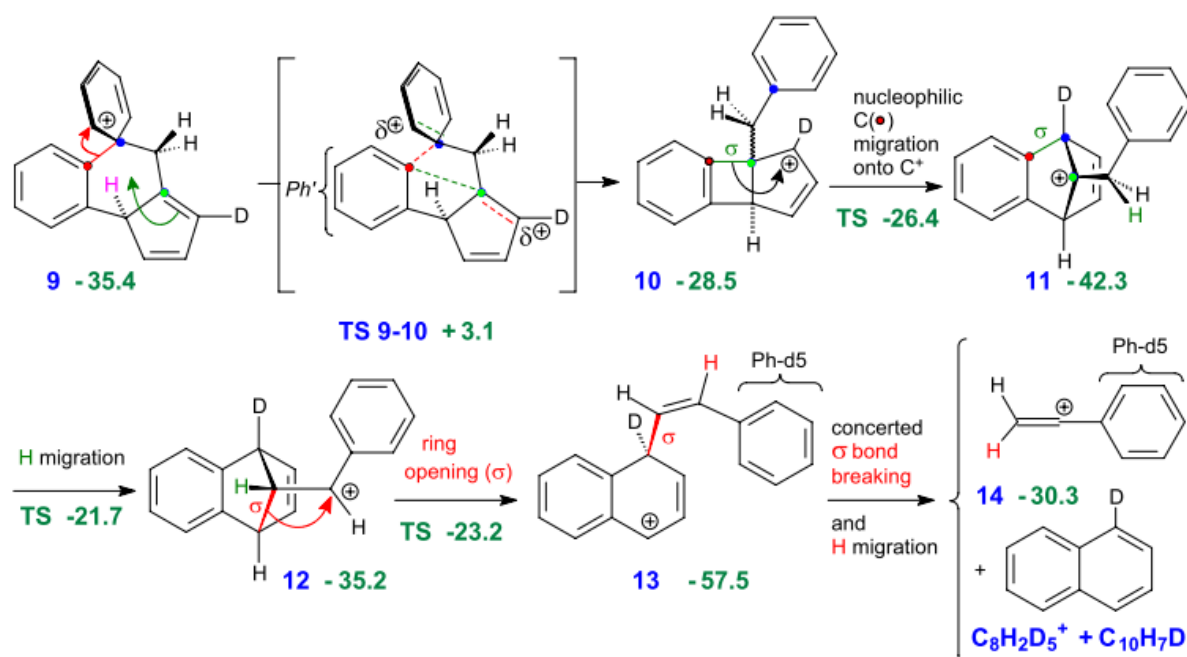
carbon is bound into the ipso position. A H [1,5] sigmatropic shift gives then **9** with a barrier of 22 kcal mol⁻¹, which keeps the evolving system below the energy of reagents by 14 kcal mol⁻¹.



Scheme 4.21: Central steps, with temporary linking of the two external phenyl rings. Energies are in kcal mol⁻¹.

From **9** further rearrangements follow. The scenario for the final fragmentation is shown in Scheme 4.22. The step **9–10** corresponds to a barrier just above the zero, which is defined by the reagents (3 kcal mol⁻¹), the step **5–6** is found to be even lower. Then two bond breakings and two bond formations in a concerted step (TS **9–10**) correspond to the shift of the carbon marked by a red dot, which belongs to the leftmost phenyl from the ipso position (blue dot) to the central 5-ring (green dot), to form a 4-membered ring in **10**. The secondary to tertiary carbocationic rearrangement **10–11** follows, while releasing the strain involved by the 4-ring, produces the fused 6-rings of the to-be naphthalene σ skeleton and a potentially leaving C_8H_7 group. A further H migration gives **12** and precedes the two bond cleavages (steps **12–13** and **13–14**), which produce naphthalene and the $(Ph-C=CH_2)^+$ fragment. In the fragmentation step the 1,2 H migration and a cleavage of C–C bond are shown.

This reaction scheme is complicated, but it is more viable than others, explored within the same perspective (forming the naphthalene framework and a potentially leav-



Scheme 4.22: Final steps: phenyl migration, formation of the naphthalene framework (in **11**), and final fragmentation. Energies are in kcal mol⁻¹.

ing group). It can be used to explain the experimental results as concerns the peak at m/z 103. It is worth pointing out that in the end the proposed pathway is exoergic and keeps most of the steps of the system below the reagents level. But it also has two small barriers (steps **5–6** and **9–10**), which can explain the fact that to observe the peak at m/z 103, we need more energy (see Fig. 4.17(a)). When working with deuterated benzene, the scheme is consistent with the formation of the major $C_8H_7^+$ species, i.e. $C_8H_2D_5^+$.

4.2.5 Conclusion

The reaction of biphenylium ion $C_{12}H_9^+$ with benzene was investigated by using API-3000. The association product $C_{18}H_{15}^+$ was detected at m/z 230. The dependences of various products ion abundances on the nominal collision energy were performed to provide some insight in the reaction processes. The adduct formation route was found to be exothermic and barrierless, and therefore might be relevant for the atmosphere of Titan. Theoretical calculations were performed to shed light on the channel $C_{12}H_9^+ + C_6H_6 \rightarrow C_8H_7^+ + C_{10}H_8$ which was in the end found to be exoergic. Other products corresponding to the loss of H , $2H/H_2$, $H + H_2$, etc. have energetic barriers and consequently might be interesting for the modelling of the PAHs growth only in “hot” environments, such as combustion

systems.

To get a rough idea of the reactivity of biphenylium ion we made a comparison between reactivities of $C_6H_5^+$, $C_{10}H_7^+$ and $C_{12}H_9^+$ ion reacting with the same amount of benzene. It was found that the association reaction of $C_{12}H_9^+$ with benzene has a reaction probability about 100 times smaller than that of the aromatic phenylium and naphtylium ions.

4.3 Formation of $C_{12}H_{11}O^+$ ion

4.3.1 Introduction

Benzene is a good model to study more complex organic molecules. It is one of the important harmful volatile organic compound (VOC) of proved carcinogenic activity. In recent years, it was demonstrated that benzene can be removed from the gas phase using atmospheric non-thermal plasmas [57, 105, 106, 107]. By changing the O_2 concentration inside the plasma, it was found that in oxygen rich environments benzene undergoes complete combustion, while when the amount of oxygen is reduced plasma processing leads to polymerization and to formation of heavier oxidised derivatives, among which phenol represents the dominant product [57, 105].

The chemical processes occurring in non-equilibrium plasmas of benzene/air mixtures working at atmospheric pressure were recently investigated in our group [57, 56]. In order to study reactive processes in non-equilibrium plasmas of benzene/air mixtures, experiments were carried out by using a dielectric barrier discharge (DBD) reactor. Neutrals were produced in a DBD, and subsequently analysed by gas chromatography-MS (GC-MS). Phenol (C_6H_5OH) was observed as the most abundant product in the GC-MS spectrum. In addition to phenol several isomers with molecular formulas $C_{12}H_{10}O$ and $C_{12}H_{10}O_2$ were also detected (see Fig. 4.23).

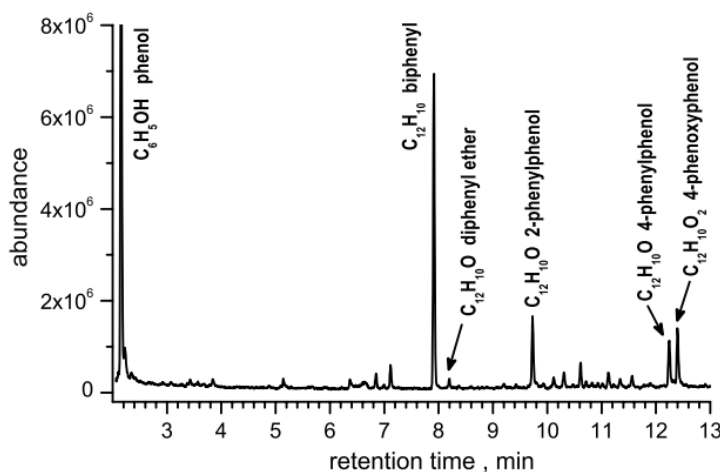


Figure 4.23: GC-MS analysis of the solid deposit obtained from the DBD treatment of a C_6H_6 mixture with 4 % of O_2 (phenol intensity off scale in the figure).

To study corona discharges of benzene/air mixture the Atmospheric Pressure Chemical

Ionization source was used. Ions were produced inside the APCI source and subsequently analysed by mass spectrometry. In Fig. 4.24(a) APCI measurements show that the most abundant peaks are observed at m/z 94 ($C_6H_6O^+$), m/z 171 ($C_{12}H_{11}O^+$) and m/z 187 ($C_{12}H_{11}O_2^+$).

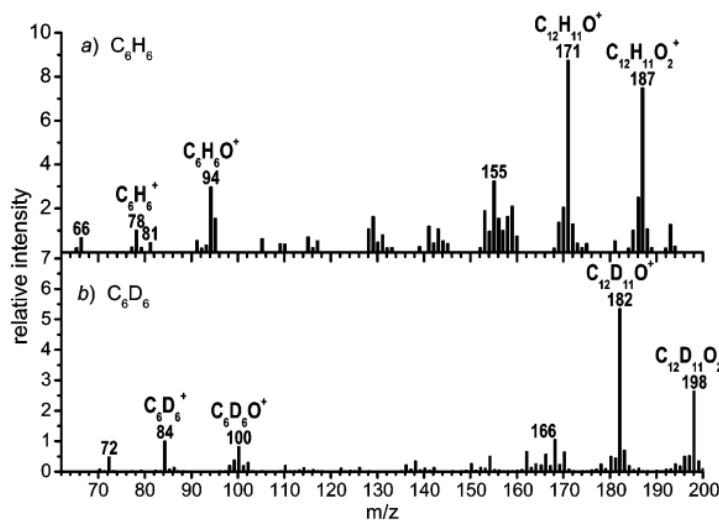


Figure 4.24: Positive ion mode mass spectra from the corona discharge source operating with: (a) benzene and (b) deuterated benzene. Air is used as nebulizer gas in both cases, and benzene injection flow is 0.1 mL/min.

Several experiments have been done to understand the chemical origin and nature of the oxygenated products. The peak at m/z 94 was attributed to phenol radical cation due to following results. When working with deuterated benzene in the APCI source, a mass shift to m/z 100 was observed (see Fig. 4.24(b)). The fragmentation spectra of ions at m/z 94 (for C_6H_6 /air mixture) and m/z 100 (C_6D_6 /air) show a loss of 28 Da, which corresponds to loss of CO molecule. It was shown that the loss of CO molecule is a typical fragmentation route of the phenol ion [108, 109]. Also, additions of D_2O to benzene (and H_2O to benzene- d_6) in the APCI source were studied. A shift is observed from m/z 94 to m/z 95 ($C_6H_5OD^+$) in the case of C_6H_6/D_2O mixture. A similar shift is observed from m/z 100 ($C_6D_6O^+$) to m/z 99 ($C_6D_5OH^+$) when working with mixture of C_6D_6 with H_2O . From all these data one can conclude that ions at m/z 94 and m/z 100 have the structure of phenol with the O-bound proton leading to H/D scrambling with water.

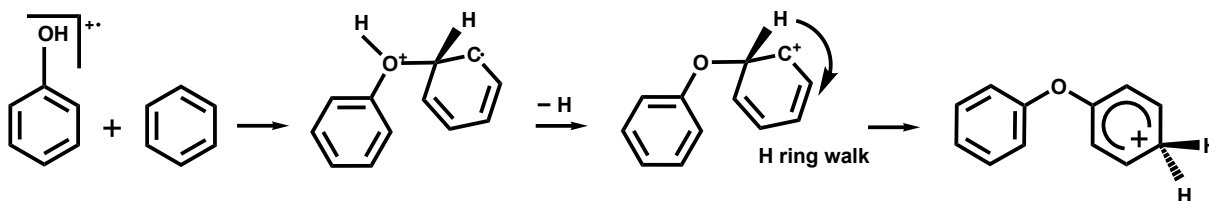
To gain information about reaction mechanisms leading to the formation of phenol cation in a benzene/air mixture several ion-molecule reactions were considered theoretically and experimentally studied in GIB-MS. It was shown that phenol was formed via

radical mechanism $C_6H_6 + O \cdot \rightarrow C_6H_5OH$ by oxygen addition on the benzene ring. The fact that phenol was detected as a neutral molecule in the DBD plasma of benzene/air mixture and as an ion in the corona discharge in the APCI source can be explained by post ionization of the neutral product [57].

For the heavier oxygenated products with molecular formulas $C_{12}H_{10}O$ and $C_{12}H_{10}O_2$, various isomeric structures have been detected in the solid deposit produced after DBD treatment using GC-MS. In particular, for the $C_{12}H_{10}O$ species the following isomers diphenyl ether, 2-phenylphenol and 4-phenylphenol have been identified on the basis of their different retention times, compared with commercially available products (see Fig. 4.23). This section is dedicated to the investigation of the possible chemical pathways leading to the formation of such isomers both in DBD and in plasma corona discharges. In the APCI mass spectrum of benzene (Fig. 4.24(a)) the ion at m/z 171 is the most abundant. A molecular formula $C_{12}H_{10}O^+$ has been established for this ion by observing a mass shift to m/z 182 when the spectrum is recorded with C_6D_6 . Hence the ion observed in the APCI source should be the protonated analogue of the neutrals observed in the solid deposit after DBD treatment.

In this section we explore the possibility that the ion $C_{12}H_{10}O^+$ observed in plasma corona discharges of C_6H_6 /air is formed not by post ionization of pre-formed neutral, but by ion-molecule reactions.

Several ionic routes for the formation of the ion at m/z 171 were proposed in the literature [110, 111]. One of the mechanism [110] is via aromatic electrophilic addition of $C_6H_5OH^+$ ions on neutral benzene (Scheme 4.25).



Scheme 4.25: Mechanism proposed for the formation of the ion observed at m/z 171.

$[C_6H_6O]^+$ ions were produced directly from commercial phenol in acetone in the APCI source and compared with the $[C_6H_6O]^+$ ions synthesized in the APCI source fed with a mixture of C_6H_6 and air. Figure 4.26 represents product ion MS spectra of selected $C_6H_6O^+$ ions reacting with benzene produced in the two above mentioned ways. As we can see, the reactivity of one type of ions is different from that of the other one. In particular, the formation of the adduct product at m/z 172 is ~ 20 times more likely

from $[C_6H_6O]^+$ ions coming from in-source synthesis than from $[C_6H_6O]^+$ deriving from commercial phenol.

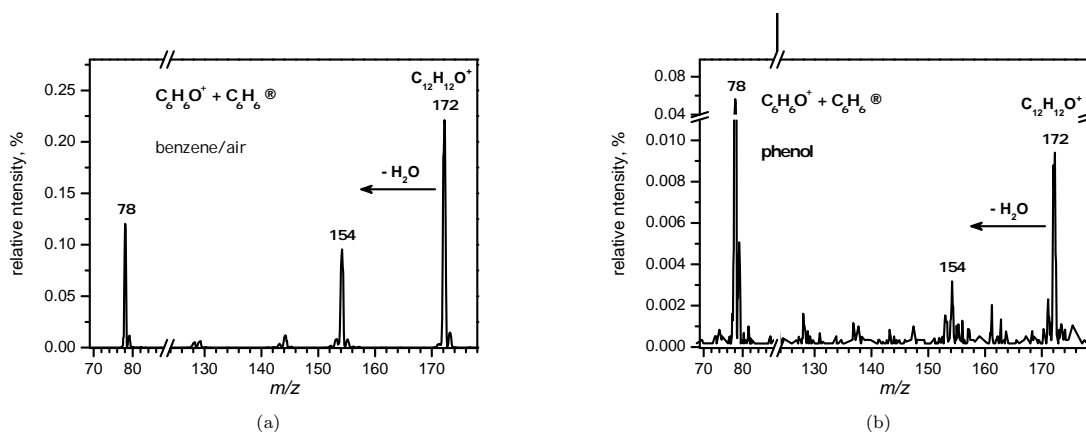
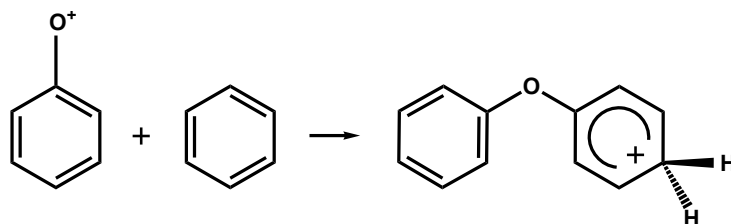


Figure 4.26: Reaction of mass selected $[C_6H_6O]^+$ (m/z 94) ions with C_6H_6 at a collision energy of 4 eV in the lab frame. The reacting $[C_6H_6O]^+$ ion was generated in two different ways: (a) by ion-molecule reaction in the APCI source fed with C_6H_6 and air; (b) by ionization of phenol in the APCI source. The pressure of benzene was about 10^{-3} mbar. The signal intensity of the parent ion (100%) is off-scale.

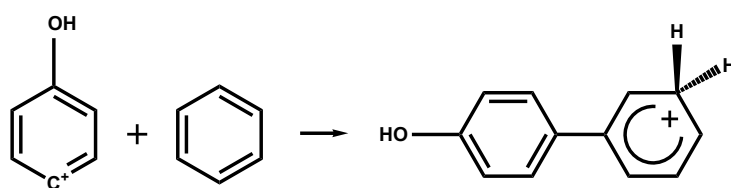
This might be explained by different degrees of internal excitation of produced $C_6H_6O^+$ ions. However this is a different problem that we have not explored any further. The important result is that for both precursors the reactivity of the $[C_6H_6O]^+$ ions is small and the main product from both reactions is an adduct at m/z 172 (and not at m/z 171), thus ruling out the attack of phenol molecular ion on the aromatic ring as a source of $C_{12}H_{11}O^+$ ion [110].

Then we moved to study the reaction of ions $[C_6H_5O]^+$ (m/z 93) with benzene as another possible source for the formation of $C_{12}H_{11}O^+$ [111]. Ions of molecular formula $[C_6H_5O]^+$ can exist in the form of two different isomers: phenoxy $C_6H_5O^+$ and hydroxyphenyl $OHC_6H_4^+$ cations [111]. Upon reaction with benzene, the two isomers should form ionic adducts with different structures (see Schemes 4.27 and 4.28). Specifically, the adduct structure from the reaction of $C_6H_5O^+$ ions with benzene could be protonated diphenyl ether (Scheme 4.27), while $OHC_6H_4^+$ ions after reacting with benzene will most likely give protonated phenylphenol (Scheme 4.28).

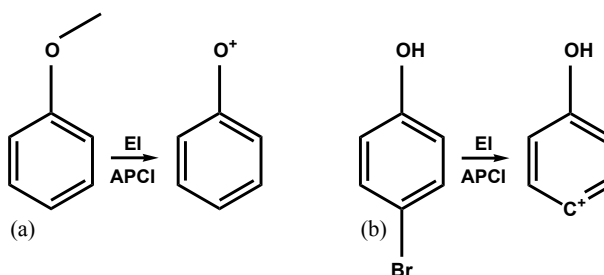
To produce phenoxy ions ($C_6H_5O^+$) we have used anisole (C_7H_8O) as a neutral precursor (see Fig. 4.29(a)), while the $OHC_6H_4^+$ ions were produced from p-bromophenol (Fig. 4.29(b)) by dissociative ionization in either EI or APCI sources.



Scheme 4.27: Mechanism proposed for the formation of the ion observed at m/z 171 through the reaction of phenoxy $C_6H_5O^+$ ions with benzene.



Scheme 4.28: Mechanism proposed for the formation of the ion observed at m/z 171 through the reaction of hydroxyphenyl $OHC_6H_4^+$ ions with benzene.



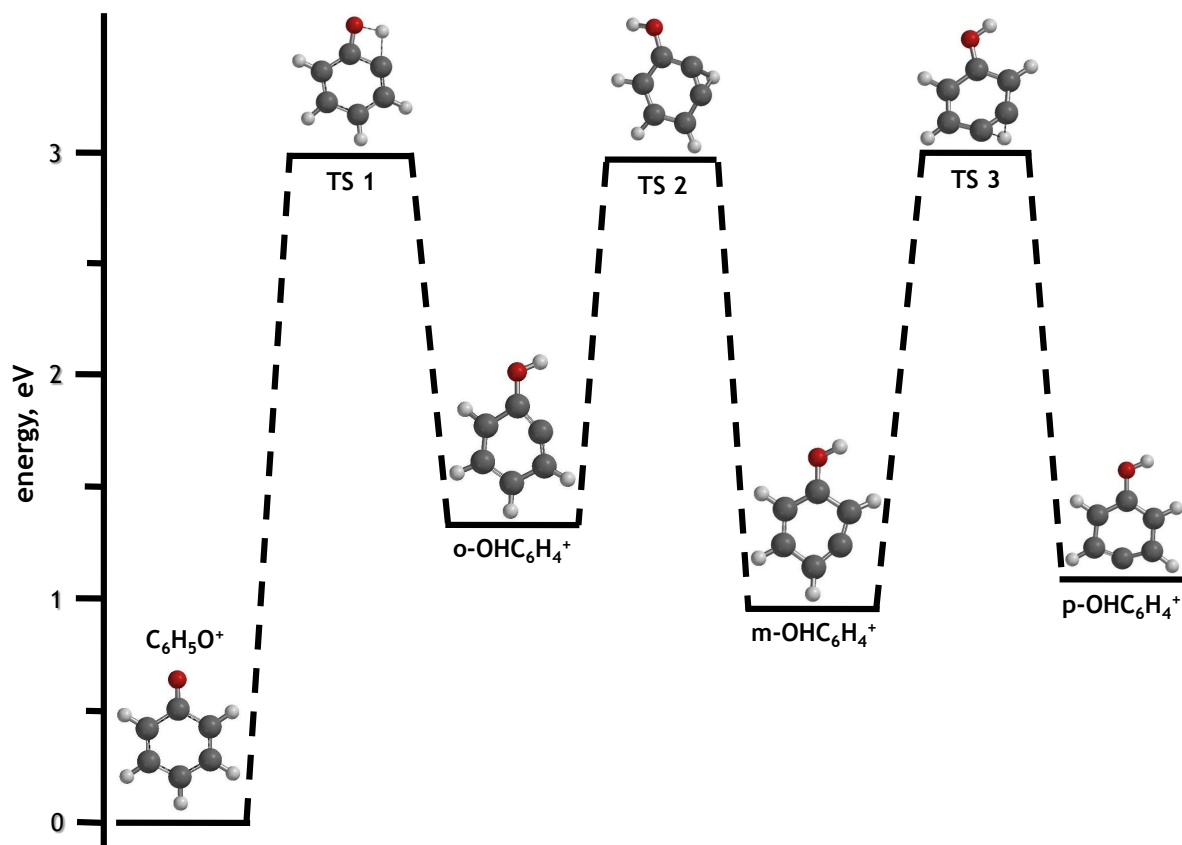
Scheme 4.29: Phenoxy ions ($C_6H_5O^+$) produced from anisole (a) and $OHC_6H_4^+$ ions produced from p-bromophenol (b) in EI or APCI source.

4.3.2 Theoretical results and reaction mechanisms

Before discussing the experimental results we present a summary of the theoretical calculations concerning the energetic and structures of the reactants and product ions. *Ab initio* quantum chemical calculations were performed at the B3LYP/6-31G* level of theory using the Spartan suite of program. Initially we focused on the possible interconversion of the two isomeric reagents $C_6H_5O^+$ and $OHC_6H_4^+$, in order to understand whether dissociative ionization of the different neutral precursors may lead to the formation of $[C_6H_5O]^+$ ions with a high degree of isomeric purity.

A schematic representation of the potential energy profile and the geometries of the most relevant structures interconnecting the ions $C_6H_5O^+$ and $OHC_6H_4^+$ is reported in

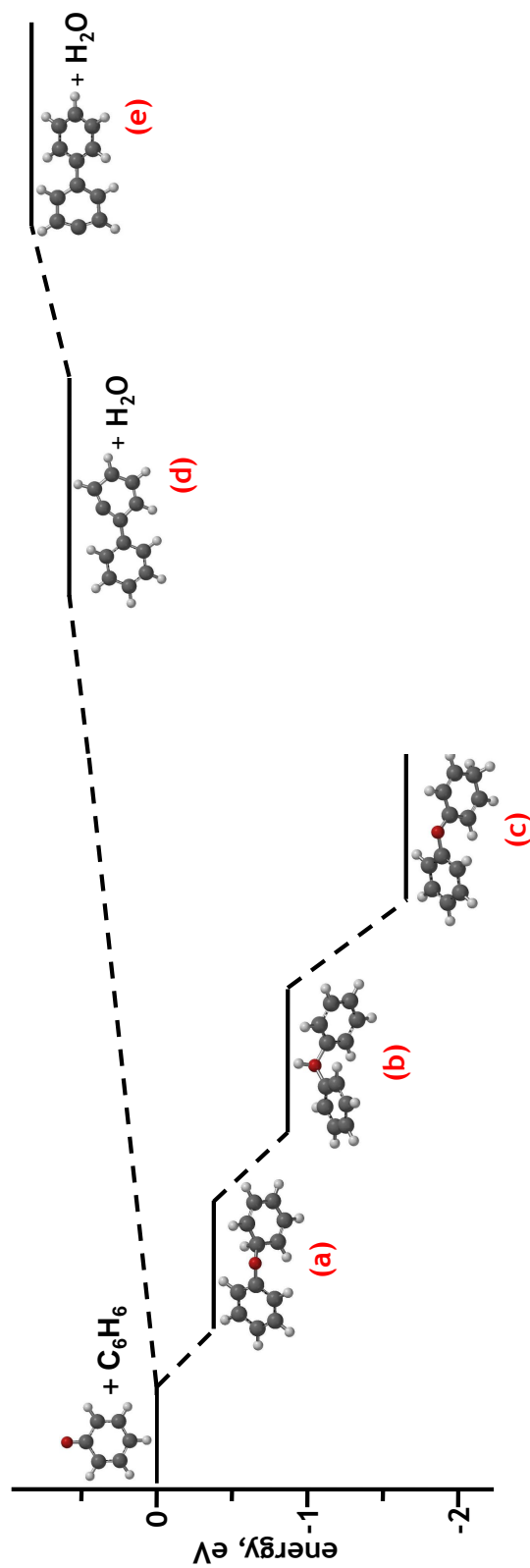
Scheme 4.30. The para- $OHC_6H_4^+$ isomer lies 1.09 eV above the $C_6H_5O^+$ ion. The isomerization $C_6H_5O^+ \rightarrow$ para- $OHC_6H_4^+$ requires the intermediate formation of the ortho- $OHC_6H_4^+$ cation that is hampered by a large energy barrier of about 3 eV (see the



Scheme 4.30: Structures and energies of isomeric $[C_6H_5O]^+$ ions.

energy and structure of the corresponding transition state, labelled as **TS 1** in Scheme 4.30). The ortho- $OHC_6H_4^+$ isomer can subsequently isomerize into the para- $OHC_6H_4^+$ via 1,2 H shifts. These rearrangements are also affected by high barriers: in particular, the transition state for the ortho-meta isomerization (**TS 2** in Scheme 4.30) lies at 2.98 eV while that for meta-para isomerization (**TS 3** in Scheme 4.30) is at 3.01 eV. Our calculations thus show that the interconversion between the two isomers is unlikely due to the presence of high energy barriers.

In Scheme 4.31 we present the results of the calculations on the reaction of the $C_6H_5O^+$ isomer with C_6H_6 . The addition of $C_6H_5O^+$ ions to benzene forms an adduct, labelled as structure (**a**), via a process that is exoergonic by 0.32 eV and barrierless. Structure (**a**) can subsequently rearrange into the more stable structures (**b**) and (**c**) corresponding to



Scheme 4.31: Schematic representation of the $C_6H_5O^+ + C_6H_6$ potential energy profile. Energies (ΔG^0) are given in eV at temperature of 298 K relative to the sum of energies of reactants.

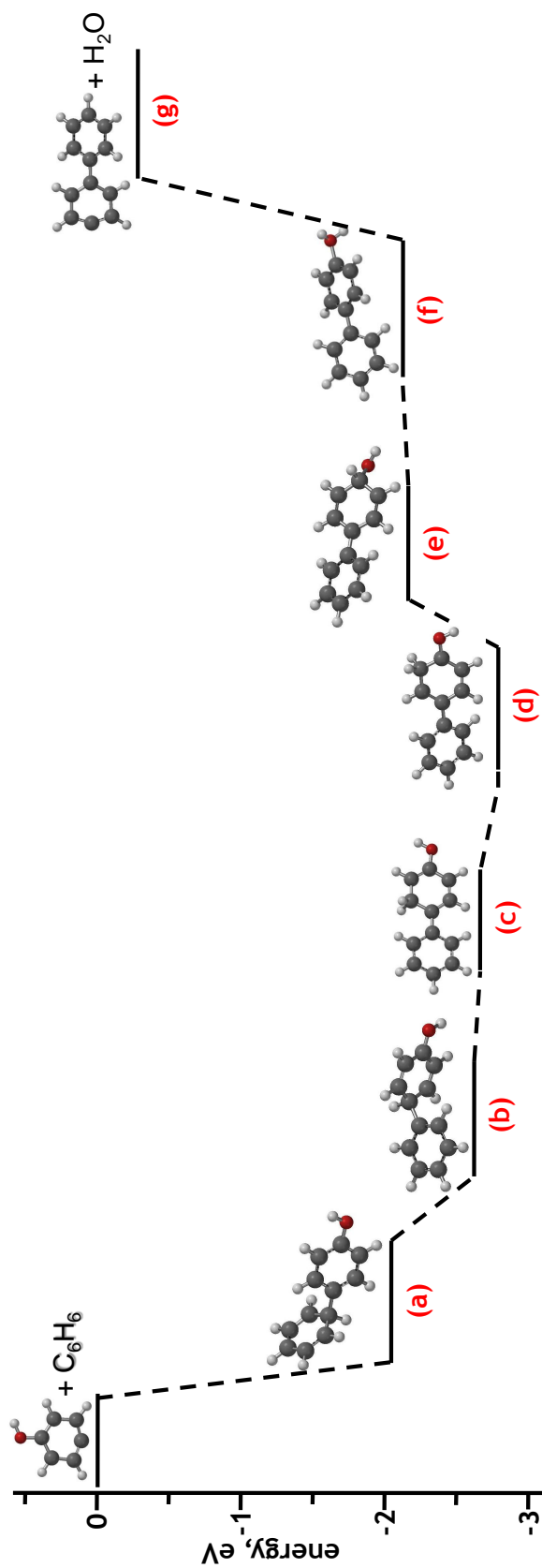
different isomers of protonated diphenyl ether by proton ring walk along the two benzene rings. In analogy with proton ring walk mechanisms previously addressed in our laboratory on protonated biphenyl, even in this case the 1,2 H shifts may present small barriers. Even though we have not explicitly calculated them, we do not expect them to be higher than 0.2–0.5 eV [85]. We also note that ring protonated diphenyl ether (structure **(c)**) is more stable, by about 1.64 eV, than the O-protonated isomer (structure **(b)**).

We have also investigated the reaction channel leading to $C_{12}H_9^+$ ion (m/z 153) plus water, that is endoergonic by 0.6 eV (13.84 kcal mol⁻¹) when $C_{12}H_9^+$ ionic product is assumed to have the structure labelled as **(d)** in Scheme 4.31. Several other structures, such as **(e)**, are also feasible, but they lie at higher energies. We have not attempted to explore any further the mechanism of $C_{12}H_9^+$ product formation, in particular to assess whether it can proceed via a complex-mediated mechanism that requires adduct formation and rearrangements.

Then we have moved to study the reaction of $OHC_6H_4^+$ cations with benzene. A schematic representation of the potential energy profile and geometries of the most relevant stationary points are reported in Scheme 4.32. The addition of C_6H_6 to $OHC_6H_4^+$ ions is a barrierless process giving rise to structure **(a)**; the process is exoergonic by 2.06 eV (47.51 kcal mol⁻¹). Adduct **(a)** can rearrange into structure **(b)**, which lies 2.16 eV below the energy of reactants, by migration of an H atom. It was shown in [102, 103] that phenylium and naphthylum ions are known to undergo statistical H/D scrambling as a consequence of the significant mobility of hydrogen atoms along the aromatic rings. Our calculations indicate that this is also the case for protonated phenylphenol cations. Due to the small energy difference between neighboring isomeric structures, an H atom prefers to “walk” along the ring (namely sequential 1,2-hydrogen shifts) and this leads to structures **(b)**–**(e)**. As shown in Scheme 4.32 the energy differences between two neighboring isomeric structures are not more than about 0.6 eV, which is in agreement with [85, 102, 103]. In addition, the reaction channel leading to the formation of $C_{12}H_9O^+$ ions plus water was also found to be exoergonic (see Scheme 4.32) by 0.27 eV (6.23 kcal mol⁻¹).

4.3.3 Experimental results

Typical mass spectra of the ionic products and the product branching ratios both obtained by API-3000 for the reaction of $C_6H_5O^+$ ions with benzene and $OHC_6H_4^+$ ions with benzene are shown in Fig. 4.33(a) and in Table 4.3. The product mass spectra from reactant ions generated via APCI source (Fig. 4.33(a)) were measured at a collision energy (in the



Scheme 4.32: Schematic representation of the $OHC_6H_4^+ + C_6H_6$ potential energy profile. Energies (ΔG^0) are given in eV at temperature of 298 K relative to the sum of energies of reactants.

centre of mass frame) $E_{CM} \sim 1$ eV and with a pressure of benzene $\sim 10^{-4}$ mbar.

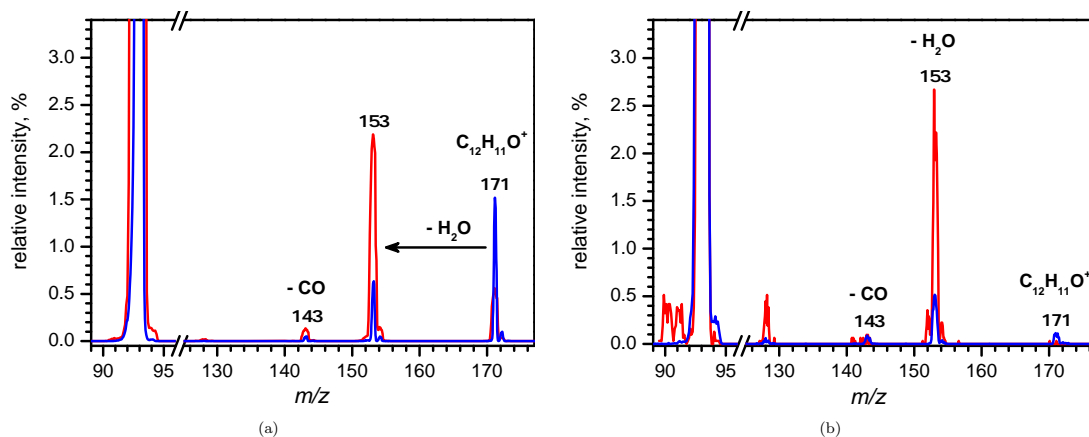


Figure 4.33: MS spectra of ionic products from selected $C_6H_5O^+$ ions (blue) and $OHC_6H_4^+$ ions (red), produced from anisole and p-bromophenol in the APCI source (a) and in the EI source (b), colliding with 10^{-4} mbar of C_6H_6 at a collision energy of 1 eV in the centre of mass frame. The signal intensity of the parent ion (100%) is off-scale.

The main ionic product for the reaction of $C_6H_5O^+$ ions with benzene is observed at m/z 171, corresponding to the ion-molecule adduct $C_{12}H_{11}O^+$ with a sufficiently long lifetime to reach the detector. The peak observed at m/z 153 is due to water loss, and the peak at m/z 143 corresponds to the loss of CO . For the reaction of $OHC_6H_4^+$ ions with benzene (see Fig. 4.33(a)) the most intense peak was observed at m/z 153, while the adduct was also present at m/z 171. According to our calculations the reactive channel giving $C_{12}H_9^+$ plus water from the reaction of the $C_6H_5O^+$ ion with benzene is endoergic at least by 0.6 eV (when the $C_{12}H_9^+$ isomeric structure (d) in Scheme 4.31 is formed), and therefore the corresponding to $C_{12}H_9^+$ ion peak at m/z 153 should not be present in the mass spectrum. However, when working at a collision energy $E_{CM} \sim 1$ eV, as done in the MS spectrum of Fig. 4.33(a), the translational energy imparted to the ionic reactant is of help to fragment the association product $C_{12}H_{11}O^+$ into $C_{12}H_9^+$ plus water.

Table 4.3: Branching ratios for formation of the various product channels observed upon reaction of both $OHC_6H_4^+$ and $C_6H_5O^+$ ions with 10^{-4} mbar pressure of C_6H_6 by API-3000.

$OHC_6H_4^+$ reagents	$C_6H_5O^+$ reagents	Position of peak
18.8%	67.1%	171
75.9%	30.3%	153
4.5%	2.4%	143
0.8%	0.2%	128

The reactions under investigation are studied also using GIB-MS, where a better control of the collision energy can be achieved. Mass spectra are measured at a collision energy of 1 eV (in the centre of mass frame) and with a pressure of benzene about 10^{-5} mbar (see Fig. 4.33(b)). It was shown that the biggest peak for both reactions was observed at m/z 153. The reacting ion $C_6H_5O^+$, produced in EI source of GIB-MS, is internally excited and expected to reduce the lifetime of the intermediate complex and therefore the probability for its stabilization into a long-lived species. On the contrary, $C_6H_5O^+$ ions produced into the APCI source can dissipate the excess of internal energy by collisions with N_2 at atmospheric pressure prior to reaction with benzene. These considerations can explain the small amount of ionic adduct $C_{12}H_{11}O^+$ at m/z 171 observed when the reactions are carried out in GIB-MS (Fig. 4.33(b)), while in the spectra recorded with API-3000 equipped with the APCI ion source (see Fig. 4.33(a)) the ionic adducts are formed with a higher yield.

The reaction of phenoxy ion $C_6H_5O^+$ with benzene are studied as a function of the collision energy with GIB-MS. Behaviour of cross sections (in arbitrary units) for the three channels are shown in Figure 4.34 over the center of mass collision energy range from 0.1 to 6 eV. Data have be-

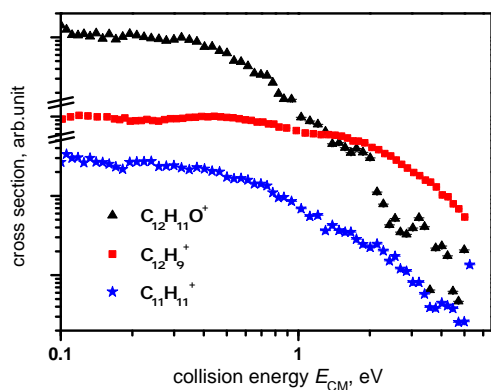


Figure 4.34: Cross sections as a function of the collision energy for the reaction of $C_6H_5O^+ + C_6H_6$ leading to the following products: $C_{12}H_{11}O^+$, $C_{12}H_9^+$ and $C_{11}H_{11}^+$.

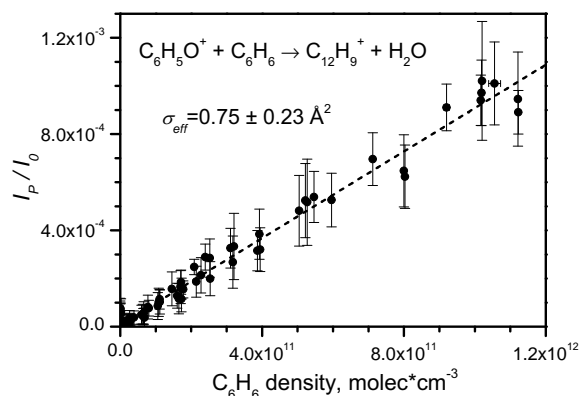


Figure 4.35: Density dependences of $C_{12}H_9^+$ product from the reaction of $C_6H_5O^+$ ion with C_6H_6 at a collision energy of ~ 0.64 eV in the center of mass frame. Dashed line is linear fit of the data.

en collected with a C_6H_6 pressure of about $\sim 2 \times 10^{-5}$ mbar to ensure adduct production via bimolecular association using GIB-MS. The adduct formation channel $C_{12}H_{11}O^+$ has a negative energy dependence and this speaks for a barrierless exothermic process, which is in agreement with theoretical calculations (see Scheme 4.31). The behaviour

of the cross section for the channel giving $C_{12}H_9^+$ at m/z 153 has also negative energy dependence, which is usually the sign of an exothermic reaction. According to our theoretical calculations the channel $C_6H_5O^+ + C_6H_6 \rightarrow C_{12}H_9^+ + H_2O$ is endoergic by at least 0.6 eV, while the same channel from the reaction $OHC_6H_4^+ + C_6H_6$ was found to be exoergic. It was also shown in Scheme 4.30 that any interconversion between the isomeric $[C_6H_5O]^+$ ions requires to overcome isomerization barriers of about 3 eV. The possible explanation for the negative energy dependence for the channel giving $C_{12}H_9^+$ ion is the following. Since $C_6H_5O^+$ ions were produced in EI source (see Fig. 4.33(b)) we have to take into account the possibility of having ions in electronically excited states. Thus such ions with an internal energy of at least ~ 0.6 eV can form the ion $C_{12}H_9^+$ via a barrierless process. This can clarify the negative energy dependence for $C_{12}H_9^+$ product channel, even if our calculations shows that this process is indeed endoergic.

The reactive channel giving $C_{12}H_9^+$ plus water has been studied by GIB-MS by measuring the ratio I_P/I_0 as a function of the density of benzene in the reaction cell, and results are shown in Figure 4.35 for the center-of-mass collision energy 0.64 eV. Data are linear with density up to a value 1.2×10^{12} molecules cm^{-3} . Ions were formed under low-pressure conditions. The corresponding range of benzene density was chosen to avoid a contribution of multiple collisions. The absolute value of the reactive cross section for the product $C_{12}H_9^+$ was estimated by fitting the data and a value of $\sigma \approx 0.75 \pm 0.23 \text{ \AA}^2$ was derived for the reaction $C_6H_5O^+ + C_6H_6 \rightarrow C_{12}H_9^+ + H_2O$.

4.3.4 H/D scrambling

Further measurements have been carried out in the API-3000 by using isotopically labelled C_6D_6 as neutral reagent, with the purpose of investigating any possible H/D atom scrambling in the channel leading to water loss to gain some insights about the mechanism. Black and red lines in Figure 4.36 show the mass region of $C_{12}(H, D)_9^+$ products from the reactions of $C_6H_5O^+$ and $OHC_6H_4^+$ ions with $\sim 10^{-4}$ mbar of C_6D_6 . The calculated intensities for position of H and D atoms from the ions corresponding to the loss of H_2O are shown as blue bars in Figure 4.36 given in terms of areas of the experimental peaks in the mass range 155–161 and then compared with the experimental results (black and red lines). It was found that for this range 155–161 the distribution seems to be statistical and this suggests that the mechanism for formation of the $C_{12}(H, D)_9^+$ ions involves the production of the adduct $C_{12}(H, D)_{11}O^+$, where the H and D atoms are randomized over both rings and therefore water loss occurs via a complex-mediated mechanisms for both

reactant isomers.

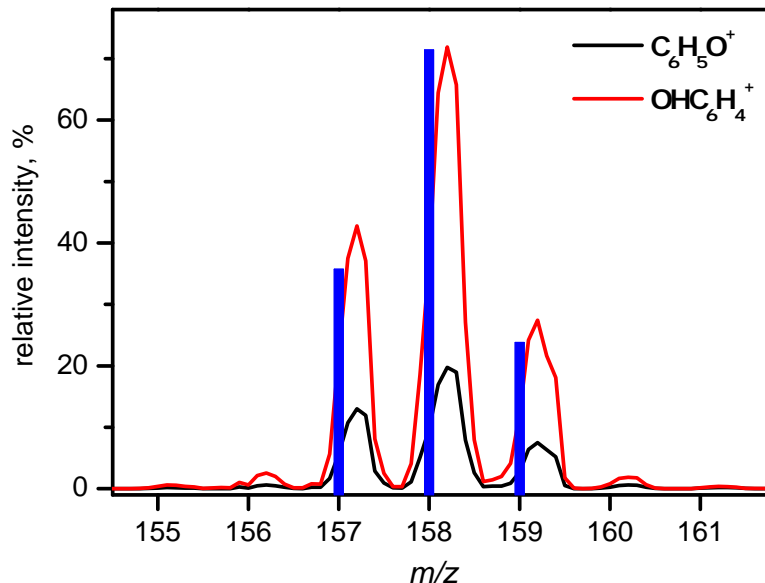


Figure 4.36: Comparison between the experimental (black and red lines) and calculated - red hatched bars intensities in the mass region of $C_{12}(H, D)_9^+$ products from the reaction of $C_6H_5O^+$ or $OHC_6H_4^+$ ions with C_6D_6 .

4.3.5 Supplementary data

To shed more light on the reaction mechanism and on the structure of the ion at m/z 171 ($C_{12}H_{11}O^+$) we have performed the following experiments. We have carried out collision induced dissociation spectra, using N_2 as fragmentation gas, of the cation $C_{12}H_{11}O^+$ (m/z 171), produced in the APCI source by infusion of a mixture of C_6H_6 /air. Then we have compared them with MS/MS spectra of isobaric ions deriving from commercial samples of diphenyl ether and 2-, 3- and 4-phenylphenol (molecular masses equal to 170 u ($C_{12}H_{10}O$), for structures see Fig. 4.37), using methanol as a solvent. In general, positive ion mode ionization of a given polar an-

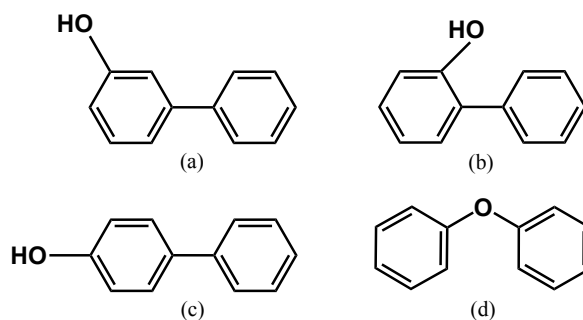


Figure 4.37: Schematic representation of commercial samples: (a) 3-phenylphenol, (b) 2-phenylphenol, (c) 4-phenylphenol, (d) diphenyl ether.

alyte molecule M in a soft ionization source such as APCI produces protonated molecular ions MH^+ . As a result, working with APCI source will give the corresponding peaks at m/z 171 for all commercial samples.

The MS/MS spectra of the ion at m/z 171 from 2-, 3- and 4-phenylphenol are very similar (Fig. 4.38) and show the following fragments: high loss of H_2O and small loss of CO .

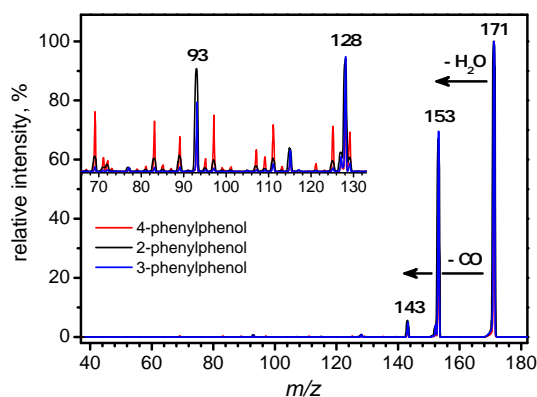


Figure 4.38: MS/MS spectra of selected $C_{12}H_{11}O^+$ ion produced from 2-, 3- and 4-phenylphenol colliding with $\sim 1.8 \times 10^{-4}$ mbar of nitrogen at a collision energy of 18 eV in the lab frame. The signal intensity of the parent ion (100%) is off-scale.

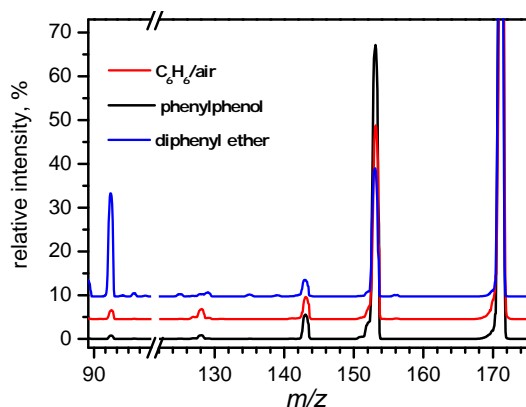


Figure 4.39: MS/MS spectra of selected $C_{12}H_{11}O^+$ ion produced from C_6H_6 /air, phenylphenol and diphenyl ether colliding with $\sim 1.8 \times 10^{-4}$ mbar of N_2 at a collision energy of 18 eV in the lab frame. The signal intensity of the parent ion is off-scale.

In Fig. 4.39 the MS/MS spectrum of $C_{12}H_{11}O^+$ ions produced from diphenyl ether are shown and the following fragments are observed: H_2O loss (major) and CO loss (minor). To compare the fragmentation spectra of MH^+ ions deriving from 2-, 3- and 4-phenylphenol and diphenyl ether with the MS/MS spectrum of the m/z 171, produced in the APCI source from a C_6H_6 /air mixture (Fig. 4.39) a linear combination of two spectra (one is MS/MS spectrum of the m/z 171 from diphenyl ether, another one is MS/MS spectrum of the m/z 171 from one of the isomeric phenylphenol) is performed in Fig. 4.40. It was found that the best fit is obtained for a relative abundance of about 94% of isomeric phenylphenol and about 6% of diphenyl ether. This means that when working with C_6H_6 /air mixture in the APCI source both types of isomers can be obtained, with a majority of isomeric phenylphenol.

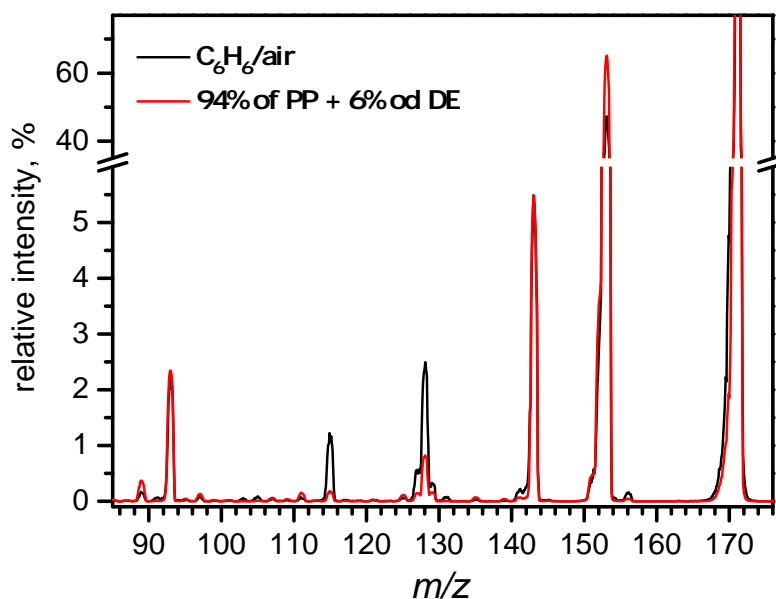


Figure 4.40: Linear combination of 94% of isomeric phenylphenol (indicated as PP) and about 6% of diphenyl ether (indicated as DE) and MS/MS spectrum of the m/z 171, produced in the APCI source from a C_6H_6 /air mixture. The signal intensity of the parent ion (100% is off-scale).

4.3.6 Conclusion

Ion-molecule reactions occurring in benzene/air corona discharges at atmospheric pressure with particular reference to the formation route of the $C_{12}H_{10}O^+$ ion were studied. It was shown that the mechanism proposed in Ref. [110] does not lead to the adduct at m/z 171, but to the $C_{12}H_{11}O^+$ ion at m/z 172. Theoretical calculations were performed to provide some mechanistic insights in the reaction processes, concerning the two precursor ions ($C_6H_5O^+$ and para- $OHC_6H_4^+$) reacting with neutral benzene. It was found that due to the presence of high isomerization barriers between the two precursors, any interconversion $C_6H_5O^+ \leftrightarrow OHC_6H_4^+$ prior to reaction is unlikely, when low collision or internal excitation energies are involved. According to our calculations the reaction of $C_6H_5O^+$ ion with benzene will lead to the adduct with a molecular structure of diphenyl ether, while the reaction of $OHC_6H_4^+$ ion will form the adduct with a molecular structure of phenylphenol. To shed more light on the structure of $C_{12}H_{11}O^+$ ion, MS/MS spectra of commercial diphenyl ether and phenylphenol were performed and compared with the ion at m/z 171 produced in the APCI source from a C_6H_6 /air mixture. The result is that the MS/MS spectrum of the m/z 171 from in-source C_6H_6 /air mixture consists of 94% of

phenylphenol and 6 % of diphenyl ether.

Bibliography

- [1] B. Berzard, P. Drossart, T. Encrenaz and H. Feuchtgruber. Benzene on the giant planet, *Icarus*, 154:492, 2001.
- [2] A. Coustenis, A. Salama, B. Schulz, S. Ott, E. Lellouch, T. Encrenaz, D. Gautier and H. Feuchtgruber. Titan's atmosphere from ISO mid-infrared spectroscopy, *Icarus* 161:383, 2003.
- [3] S.W. Leach, *Z. Phys. Chem.*, Munchen Ger., 195:15, 1996.
- [4] A.G.G.M. Tielens and S.B. Charnley. *Origins Life Evol. Biosphere.* 27:23, 1997.
- [5] M. Steglich, J. Bouwman, F. Huisken and T. Henning. Can neutral and ionized PAHs be carriers of the UV extinction bump and the diffuse interstellar bands? *The Astrophysical Journal*, 742:2, 2011.
- [6] L.J. Allamandola, J.R. Tielens, J.R. Barker. *Astrophys. J. Suppl. series*, 71:733, 1989.
- [7] E. Herbst. *J. Astrophys.*, 366:133, 1991.
- [8] T. Allain, S. Leach, E. Sedlmayr. Photodestruction of PAHs in the interstellar medium. I. Photodissociation rates for the loss of an acetylenic group. *Astron. Astrophys.*, 305:602. 1996.
- [9] N.L.J. Cox. The PAH-DIB hypothesis. *EAS Publications Series*, 46:349, 2011.
- [10] B.D. Nourse, T.B. McMahon. *Org. Mass Spectrometry*, 100:701, 1990.
- [11] D.K. Bohme. *Chem. Rev.*, 92:1487, 1992.
- [12] I. Feng, C. Lifschitz. *Int. J. Mass Spectrometry and Ion Processes*, 152:157, 1996.
- [13] <http://saturn.jpl.nasa.gov/>

- [14] F.M. Flasar et al.. Titan's atmospheric temperatures, winds, and composition. *Science*, 308:975, 2005.
- [15] R.V. Yelle, N. Borggren, V. De La Haye, W.T. Kasprzak, H.B. Niemann, I.C.F. Muller-Wodarg, J.H. Waite, Jr.. The vertical structure of Titan's upper atmosphere from Cassini Ion Neutral Mass Spectrometer measurements. *Icarus* 182:567, 2006.
- [16] S. Vinatier, B. Berzard, T. Fouchet, N.A. Teanby, R. de Kok, P.G.J. Irwin, B.J. Conrath, C.A. Nixon, P.N. Romani, F.M. Flasar, A. Coustenis. Vertical abundance profiles of hydrocarbons in Titan's atmosphere at 15° S and 80° N retrieved from Cassini/CIRS spectra. *Icarus*, 188:120, 2007.
- [17] J. Cui, R.V. Yelle, V. Vuitton, J.H. Waite, Jr., W.T. Kasprzak, D.A. Gell, H.B. Niemann, I.C.F. Muller-Wodarg, N. Borggren, G.G. Fletcher, E.L. Patrick, E. Raaen, B. Magee. Analysis of Titan's neutral upper atmosphere from Cassini Ion Neutral Mass Spectrometer measurements. *Icarus*, 200:581, 2009.
- [18] N.A. Teanby, P.G.J. Irwin, R. De Kok, C.A. Nixon, A. Coustenis, B. Berzard, S.B. Calcutt, N.E. Bowles, F.M. Flasar, L. Fletcher, C. Howett, F.W. Taylor. Latitudinal variations of HCN , HC_3N , and C_2N_2 in Titan's stratosphere derived from Cassini CIRS data. *Icarus*, 181:243, 2006.
- [19] R. De Kok, P.G.J. Irwin, N.A. Teanby, E. Lellouch, B. Berzard, S. Vinatier, C.A. Nixon, L. Fletcher, C. Howett, S.B. Calcutt, N.E. Bowles, F.M. Flasar, F.W. Taylor. Oxygen compounds in Titan's stratosphere as observed by Cassini CIRS. *Icarus*, 186:354, 2007.
- [20] J.-E. Wahlund, M. Galand, I. Muller-Wodarg, J. Cui, R.V. Yelle, F.J. Crary, K. Mandt, B. Magee, J.H. Waite, Jr., D.T. Young, A.J. Coates, P. Garnier, K. Agren, M. Andre, A.I. Eriksson, T.E. Cravens, V. Vuitton, D.A. Gurnett and W.S. Kurth. On the amount of heavy molecular ions in Titan's ionosphere. *Plan. Space Sci.*, 57:1857, 2009.
- [21] F.J. Crary, B.A. Magee, K. Mandt, J.H. Waite, Jr., J. Westlake and D.T. Young. Heavy ions, temperatures and winds in Titan's ionosphere: Combined Cassini CAPS and INMS observations. *Plan. Space Sci.*, 57:1847, 2009.
- [22] E.C. Sittler Jr., A. Ali, J.F. Cooper, R.E. Hartle, R.E. Johnson, A.J. Coates and D.T. Young. Heavy ion formation in Titan's ionosphere: magnetospheric introduction of free oxygen and a source of Titan's aerosols? *Plan. Space Sci.*, 57:1547, 2009.

- [23] M.L. Delitsky and C.P. McKay. The photochemical products of benzene in Titan's upper atmosphere. *Icarus*, 207:477, 2010.
- [24] L.H. Lim, R.M. Harrison, and S. Harrad. The contribution of traffic to atmospheric concentrations of polycyclic aromatic hydrocarbons. *Environ. Sci. Technol.*, 33:3538, 1999.
- [25] E.M. Lamoureux, and B.J. Brownawell. Chemical and biological availability of sediment-sorbed hydrophobic organic contaminants. *Environ. Toxicol. Chem.*, 18:1733, 1999.
- [26] N. Ohkouchi, K. Kawamura, and H. Kawahata. Distributions of three- to seven-ring polynuclear aromatic hydrocarbons on the deep sea floor in the central Pacific. *Environ. Sci. Technol.*, 33:3086, 1999.
- [27] H.-Y.N. Holman, Y.W. Tsang, and W.R. Holman. Mineralization of sparsely water-soluble polycyclic aromatic hydrocarbons in a water table fluctuation zone. *Environ. Sci. Technol.*, 33:1819, 1999.
- [28] L.C. Marr, T.W. Kirchstetter, R.A. Harley, A.H. Miguel, S.V. Hering, and S.K. Hammond. Characterization of polycyclic aromatic hydrocarbons in motor vehicle fuels and exhaust emissions. *Environ. Sci. Technol.* 33:3091, 1999.
- [29] J. Gundel, C. Mannschreck, K. Buttner, U. Ewers, and J. Angerer. Urinary levels of 1-hydroxypyrene, 1-, 2-, 3-, and 4-hydroxyphenanthrene in females living in an industrial area of Germany. *Arch. Environ. Contam. Toxicol.*, 31:585, 1996.
- [30] Z. Wang, M. Fingas, Y.Y. Shu, L. Sigouin, M. Landriault, and P. Lambert. Quantitative characterization of PAHs in burn residue and soot samples and differentiation of pyrogenic PAHs from petrogenic PAHs the 1994 mobile burn study. *Environ. Sci. Technol.*, 33:3100, 1999.
- [31] C.S. McEnally, L.D. Pfefferle, B. Atakan, and K. Kohse-Hoinghaus. Studies of aromatic hydrocarbon formation mechanisms in flames: Progress towards closing the fuel gap. *Prog. Energy Combust. Sci.*, 32:247–294, 2006.
- [32] M. Lyubovsky, L.L. Smith, M. Castaldi, H. Karim, B. Nentwick, S. Etemad, R. LaPierre, and W.C. Pfefferle. Catalytic Combustion over Platinum Group Catalysts: Fuel-Lean versus Fuel-Rich Operation. *Catalysis Today*, 83:71, 2003.

- [33] R.A. Kanaly and S. Harayama. Biodegradation of High-Molecular-Weight Polycyclic Aromatic Hydrocarbons by Bacteria. *Journal of bacteriology*, 182(8):2059, 2000.
- [34] S. Muller and R.J. Zahn. Air pollution control by non-thermal plasma. *Contrib. Plasma Phys.*, 47:520, 2007.
- [35] E. Marotta, A. Callea, X. Ren, M. Rea and C. Paradisi. Ionic intermediates and mechanisms of hydrocarbon processing. *Plasma Process. Polym.*, 5:146, 2008.
- [36] L. Martin, S. Ognier, E. Gasthauer, S. Cavadias, S. Dresvin and J. Amouroux. Destruction of Highly Diluted Volatile Organic Compounds (VOCs) in Air by Dielectric Barrier Discharge and Mineral Bed Adsorption. *Energy Fuels*, 22:576, 2008.
- [37] M.J. Gallagher, R. Geiger, A. Plevich, A. Rabinovich, A. Gutsol, A. Fridman. On-board plasma-assisted conversion of heavy hydrocarbons into synthesis gas. *Fuel*, 89(6):1187, 2010.
- [38] G. Petitpas, J.-D. Rollier, A. Darmon, J. Gonzalez-Aguilar, R. Metkemeijer and L. Fulcheri. A comparative study of non-thermal plasma assisted reforming technologies. *Int. J. Hydrog. Energy*, 32(14):2848, 2007.
- [39] M. Mori, H. Izumi, K. Nakagawa, T. Nakamoto, T. Mori, Y. Kawashimo and Y. Ueda. Fine characterization of plasma-polymerized films from a methane/air mixture. *J. Appl. Polym. Sci.*, 101(5):3408, 2006.
- [40] M. Frenklach, H. Wang. H. Bockhorn (Ed.), Soot Formation in Combustion, Springer-Verlag, Heidelberg, 165, 1994
- [41] H. Wang, M. Frenklach. A Detailed Kinetic Modeling Study of Aromatics Formation in Laminar Premixed Acetylene and Ethylene Flames. *Combust. Flame*, 110:173, 1997.
- [42] E. Herbst. Chemistry of star-forming regions. *J. Phys. Chem. A*, 109:4017, 2005.
- [43] D. Smith. The Ion Chemistry of Interstellar Clouds. *Chem. Rev.*, 92:1473, 1992.
- [44] M.J. McEwan, V. Anicich. Titan's ion chemistry: a laboratory perspective *Mass Spectr. Review*, 26:281–319, 2007.
- [45] E. Herbst. The chemistry of interstellar space. *Chem. Soc. Rev.*, 30:168, 2001.
- [46] J. Roithova and D. Schroder. Bond-Forming Reactions of Molecular Dications as a New Route to Polyaromatic Hydrocarbons. *J. Am. Chem. Soc.*, 128:4208, 2006.

- [47] J. Roithova and D. Schroder. Bond-formation versus electron transfer: C-C-coupling reaction of hydrocarbon dications with benzene. *Phys. Chem. Chem. Phys.*, 9:731, 2007.
- [48] J. Roithova, C.L. Ricketts, D. Schroder. Reactions of the dications $C_7H_6^{2+}$, $C_7H_7^{2+}$ and $C_7H_8^{2+}$ with methane: predominance of double charged intermediates. *Int. J. Mass Spectrom.*, 280:32, 2009.
- [49] P. Tosi, D. Ascenzi, P. Franceschi, G. Guella. Ion chemistry in gaseous discharges at atmospheric pressure. *Plasma Sources Sci. Technol.* 18:034005, 2009.
- [50] J. Friedrich. Mechanisms of plasma polymerization-Reviewed from a chemical point of view. *Plasma Processes and Polymers*, 8(9):783, 2011.
- [51] P. Tosi, D. Cappelletti, O. Dmitriev, S. Giordani, D. Bassi, D.R. Latimer and M.A. Smith. Dissociative Charge Transfer of Argon Ions with Methane Molecules from Ultralow to Superthermal Collision Energies. *J. Phys. Chem.*, 99:15538, 1995.
- [52] P. Tosi, D. Bassi, B. Brunetti and F. Vecchiocattivi. Molecular processes in $CH_4 - H_2$ plasmas diluted with rare gases: reactions of X^* atoms and X^+ ions ($X=Ne$ and Ar) with methane molecules*. *Int. J. Mass Spectrom. Ion Process.*, 149-150:345, 1995.
- [53] G.Ya. Gerasimov. Mechanism of Gas-Phase Degradation of Polycyclic Aromatic Hydrocarbons by the Action of Ionizing Radiation. *High Energy Chemistry*, 44(1):1, 2010.
- [54] G.Ya. Gerasimov. IonMolecule Formation of Polycyclic Aromatic Hydrocarbons by the Action of Ionizing Radiation. *High Energy Chemistry*, 45(2):162, 2011.
- [55] D. Ascenzi, J. Aysina, P. Tosi, A. Maranzana, G. Tonachini. Growth of polyaromatic molecules via ion-molecule reactions: an experimental and theoretical mechanistic study. *The Journal of Chemical Physics*, 133(18):184308, 2010.
- [56] G. Guella, P. Franceschi, P. Tosi. *Chem. Phys. Lett.*, 415:265, 2005.
- [57] D. Ascenzi, P. Franceschi, G. Guella and P. Tosi. Phenol Production in Benzene/Air Plasmas at Atmospheric Pressure. Role of Radical and Ionic Routes. *J. Phys. Chem. A*, 110:7841, 2006.
- [58] D.J. Griffiths. Introduction to Quantum Mechanics, Prentice-Hall, Engelwood Cliffs, NJ, 1995.
- [59] N.H. March. Self-Consistent Fields in Atoms, Pergamon, New York, 1975.

- [60] W. Thiel. *Advances in Chemical Physics*, Volume XCIII, I. Prigogine and S. A. Rice, Eds., Wiley, New York, 1996.
- [61] M. Born and R. Oppenheimer. Zuer quantentheorie der molekeln, *Annalen der Physik*, 84:457, 1927.
- [62] P. Hohenberg and W. Kohn. *Phys. Rev. B*, 136, 86, 1964.
- [63] I.N. Levine. *Quantum Chemistry*, 5th edn, Prentice Hall, Upper Saddle River, New Jersey, 2000.
- [64] S.S. Iyengar, M. Ernzerhof, S.N. Maximoff and G.E. Scuseria. Challenge of creating accurate and effective kinetic-energy functionals. *Physical Review A*, 63(5):052508, 2001.
- [65] W. Kohn and L.J. Sham. Self-consistent equations including exchange and correlation effects. *Physical Review*, 140(4A):1133, 1965.
- [66] A.D. Becke. Density-functional Thermochemistry.3. the Role of Exact Exchange. *Journal of Chemical Physics*, 98(7):5648, 1993.
- [67] P.J. Stephens, F.J. Devlin, C.F. Chabrowski and M.J. Frisch. *J. Phys. Chem.*, 98:11623, 1994 and references therein.
- [68] C.T. Lee, W.T. Yang and R.G. Parr. Development of the Colle-salvetti Correlation-energy Formula Into A Functional of the Electron-density. *Physical Review B*, 37(2):785, 1988.
- [69] S.H. Vosko, L. Wilk and M. Nusair. Accurate Spin-dependent Electron Liquid Correlation Energies For Local Spin-density Calculations - A Critical Analysis. *Canadian Journal of Physics*, 58(8):1200, 1980.
- [70] E. Lewars. *Computational chemistry*. *Kluwer Academic Publishers*, ISBN 0-306-48391-2, 2004.
- [71] A. Szabo and N.S. Ostlund. *Modern Quantum Chemistry*. *Dover Publications, Inc.*, Mineola, ISBN 0-486-69186-1, 1996.
- [72] T.H. Dunning, Jr.. *J. Chem. Phys.*, 90:1007, 1989.
- [73] E. Woon and T.H. Dunning, Jr.. *J. Chem. Phys.*, 98:1358, 1993.

- [74] M.M. Francl, W.J. Pietro, W.J. Hehre, J.S. Binkley, M.S. Gordon, D.J. Defrees and J.A. Pople. Self-consistent Molecular-orbital Methods.23. A Polarization-type Basis Set For 2nd-row Elements. *Journal of Chemical Physics*, 77(7):3654, 1982.
- [75] M.J. Frisch, G.W. Trucks, H.B. Schlegel, et al., GAUSSIAN 09, Revision A.02, Gaussian, Inc., Wallingford CT, 2009.
- [76] D. Young. Computational Chemistry. *Wiley-Interscience*, Appendix A. A.1.6:330, 2001.
- [77] P.H. Dawson. Quadrupole Mass Spectrometry and its Applications. *New York: American Institute of Physics*, 1995.
- [78] D. Gerlich. Diplomarbeit, University of Freiburg, Federal Republic of Germany, p 1, 1971.
- [79] E. Teloy, D. Gerlich. Integral Cross Sections for Ion-molecule Reactions. I. The Guided Beam Technique. *Chem. Phys.*, 4:417, 1974.
- [80] D. Gerlich. Inhomogeneous rf Fields: A Versatile Tool for the Study of Processes with Slow Ions. In State-Selected and State-to-State Ion-Molecule Reaction Dynamics. *Ng, C.-Y.; Baer, M., Eds.*, I:1, 1992.
- [81] K.M. Ervin, P.B. Armentrout. Translational Energy Dependence of $\text{Ar}^+ + \text{XY} \rightarrow \text{ArX}^+ + \text{Y}$ ($\text{XY} = \text{H}_2, \text{D}_2, \text{HD}$) from Thermal to 30 eV cm. *J. Chem. Phys.*, 83:166, 1985.
- [82] P.B. Armentrout. Mass Spectrometry Not Just a Structural Tool: The Use of Guided Ion Beam Tandem Mass Spectrometry to Determine Thermochemistry. *J. Am. Soc. Mass Spectrom.*, 13:419, 2002.
- [83] J.K. Fremerey. The spinning rotor gauge. *J. Vac, Sci. Technol. A*, 3(3):1715, 1985.
- [84] P.B. Armentrout. Fundamentals of ionmolecule chemistry. *J. Anal. At. Spectrom.*, 19:571, 2004.
- [85] D. Ascenzi, N. Cont, G. Guella, P. Franceschi and P. Tosi. New Insights into the Reaction Mechanisms of Phenylum Ions with Benzene. *J. Phys. Chem. A*, 111(49):12513, 2007.
- [86] S. Iglesias-Groth, A. Manchado, D.A. Garcia-Hernandez, J.I. Gonzalez Hernandez, D.L. Lambert. *Astrophys. J.*, 685:L55, 2008.

- [87] A.N. Eraslan, R.C. Brown. *Combust. Flame*, 74:19, 1988.
- [88] A.M. Starik, A.M. Savel'ev, N.S. Titova. *Plasma Source Sci. Technol.*, 17:045012, 2008.
- [89] H. Haverkamp, S. Wilhelm, A. Sorokin, F. Arnold. *Atmosph. Environment*, 38:2879, 2004.
- [90] D.K. Bohme, S. Wlodek, J.A. Zimmerman, J.R. Eyler. *Int. J. Mass Spectrom. Ion Proc.*, 109:31, 1991.
- [91] P.O. Momoh, S.A. Abrash, R. Maboutki, M.S. El-Shall. *J. Am. Chem. Soc.*, 128:12408, 2006.
- [92] P.O. Momoh, A.-R. Soliman, M. Meot-Ner, A. Ricca, M.S. El-Shall. *J. Am. Chem. Soc.*, 130:12848, 2008.
- [93] J.H. Waite, D.T. Young, T.E. Cravens, A.J. Coates, F.J. Crary, B.A. Magee and J. Westlake. The process of tholin formation in Titan's upper atmosphere. *Science*, 316:870, 2007.
- [94] I.P. Robertson, T.E. Cravens, J.H. Waite, Jr., R.V. Yelle, V. Vuitton, A.J. Coates, J.E. Wahlund, K. Agren, K. Mandt, B.A. Magee, M.S. Richard and E. Fating. Structure of Titan's ionosphere: model comparisons with Cassini data. *Plan. Space Sci.*, 57:1834, 2009.
- [95] G. Angelini, Y. Keheyan, E. Lilla, G. Perez. *Radiochim. Acta*, 51:173, 1990.
- [96] Y. Keheyan, R. Bassanelli. *Radiat. Phys. Chem.*, 47:465, 1996.
- [97] M. Slegt, F. Minne, H. Zuilhof, H.S. Overkleeft and G. Lodder. *Eur. J. Org. Chem.*, 32:5353, 2007.
- [98] We can report that in ref. [97] the reverse ordering was found: calculations at the B3LYP/6-311G(d,p) in vacuo give the triplet as the most stable structure, with the singlet lying only 1.1 kcal mol⁻¹ higher in energy.
- [99] H.A. Galue, J. Oomens. Spectroscopic Evidence for a Triplet Ground State in the Naphthyl Cation *Angew. Chem. Int. Ed.*, 50:7004-7007, 2011.
- [100] We report here some cc-pvTZ energy differences. Starting from naphthylum in the triplet state, **1** is at -28.3 kcal mol⁻¹ and the barrier for H migration (**1-2**) is +6.3

kcal mol⁻¹ above the reactants. The C–C bond formation (**2–3**) from **2** (–32.9 kcal mol⁻¹) is located at +7.9 kcal mol⁻¹ and leads to the intermediate **3** (–2.5 kcal mol⁻¹ with respect to the reactants). Both H migrations form **3** (**3–4a** and **3–4**) have energy barriers above the reactants: +25.6 and +13.8 kcal mol⁻¹ respectively.

- [101] See supplementary material at <http://dx.doi.org/10.1063/1.3505553> for M062X/cc-pvTZ optimized structures (cartesian coordinates) of reactants, products, transition structures, and intermediates, and their M06-2X/CBS//M06-2X/cc-pvTZ energies.
- [102] D. Ascenzi, D. Bassi, P. Franceschi, P. Tosi, M. Di Stefano, M. Rosi, and A. Sgamellotti. Reactions of phenylium ions $C_6(H, D)_5^+$ with D_2 . *J. Phys. Chem. A*, 119(16):8366–8372, 2003.
- [103] D. Ascenzi, D. Bassi, P. Franceschi, O. Hadjar, P. Tosi, M. Di Stefano, M. Rosi, and A. Sgamellotti. Reactivity of $C_{10}H_7^+$ and $C_{10}D_7^+$ with H_2 and D_2 . *J. Phys. Chem. A*, 121(14):6728–6737, 2004.
- [104] ¹³C contributions of peaks at $m/z=m$ on peaks at $m/z=m+1$ in the clusters corresponding to $C_{15}(H, D)_n^+$ (n=9–11) amounts to 5.35 %.
- [105] H. Sekiguchi, M. Ando, H. Kojima. *J. Phys. D: Appl. Phys.*, 38:2, 2005.
- [106] Z. Ye, Y. Zhang, P. Li, L. Yang, R. Zhang, H. Hou. Feasibility of destruction of gaseous benzene with dielectric barrier discharge. 2008.
- [107] G.R. Dey, A. Sharma, K.K. Pushpa, T.N. Das. *Journal of Hazardous Materials*, 178:693, 2010.
- [108] H.T. Le, R. Flammang, P. Gerbaux, G. Bouchoux, M.T. Nguyen. *J. Phys. Chem. A*, 105:11582, 2001.
- [109] D. Kuck. In *The Chemistry of Phenols. Rappoport, Z., Ed.; John Wiley and Sons: New York*, 4:259, 2003.
- [110] M. Tubaro, E. Marotta, R. Seraglia and P. Traldi. *Rapid Comm. Mass Spectrom.*, 17:2423, 2003.
- [111] D. Zagorevskii and J.L. Holmes. *Eur. J. Mass Spectrom.*, 2:341, 1996.

